Characterizing the AC-MOT

by

Melissa Anholm

B.Sc., University of California–Santa Barbara, 2006
M.Sc., University of Wisconsin–Milwaukee, 2009

A THESIS SUBMITTED IN PARTIAL FULFILLMENT OF
THE REQUIREMENTS FOR THE DEGREE OF

MASTER OF SCIENCE

in

The Faculty of Graduate and Postdoctoral Studies

(Physics)

THE UNIVERSITY OF BRITISH COLUMBIA

(Vancouver)

August 2014

Abstract

Magneto-Optical Traps (MOTs) have long been used to produce samples of cold trapped neutral atoms, which can be used in the measurement of a variety of physical quantities and theories. Until recently, one limitation of this type of trap was the necessity for the presence of a relatively large magnetic field which would decay only slowly after the trapping mechanism was turned off. This residual magnetic field is expected to partially destroy any atomic polarization induced, for example, by optical pumping. As a result, the precision of any physical measurement which requires polarization is limited. We will discuss the construction of our version of a newer type of MOT, the AC-MOT [2], which is designed specifically so as to minimize residual magnetic fields. We have found that our AC-MOT has lifetimes and cloud sizes similar to those we measured in our DC-MOT. We intend to use a trap similar to this in upcoming nuclear beta decay parity-violation measurements. We also discuss the numerical evolution of the optical Bloch equations in the presence of transverse and longitudinal magnetic fields, so as to quantify the effect of a magnetic field on atomic polarization.

Table of Contents

Abstract ii

Table of Contents iii

List of Figures v

Acknowledgements vii

1 Introduction and Motivation 1
  1.1 Motivation 1
  1.2 Overview 2

2 The Magneto-Optical Trap 3
  2.1 The Zeeman Shift 3
  2.2 Atoms in an Optical Molasses 4
  2.3 The Magneto-Optical Trap 8

3 The AC-MOT–What Makes It Different? 13

4 The Offline AC-MOT 15
  4.1 Methodologies for Measuring Trap Characteristics 15
    4.1.1 Measuring the Number of Trapped Atoms 17
    4.1.2 Measuring the Lifetime 19
    4.1.3 Measuring the Trap Width and Position 19
  4.2 Laser Frequency Calibrations in the Offline AC-MOT 22
  4.3 The Phenomenology of Lifetime Measurements in the AC- and DC-MOT 25
  4.4 Measured Lifetimes and AC Frequency 25
  4.5 Systematic Effects in the Offline AC-MOT 28

5 Turning the Trap Off 30
  5.1 Methods for Turning Off the Trap 31
  5.2 Duty Cycle 35

5.3 Residual Magnetic Field in a Pyrex Cell 38

6 Calibrations of the Online Trap 41
6.1 Frequency Response in the Online Setup 45
6.2 Frequency Response in the Hall Probes 46
6.3 Acoustic Resonances 49
6.4 Control of Online Power Supplies 52
6.4.1 Determining the Number of Points for an Arbitrary Waveform 52
6.4.2 Adjusting Waveform Parameters 53
6.5 Residual Magnetic Field in the Online Chamber 56
6.6 Magnetic Field During Optical Pumping Time 59

7 The Optical Bloch Equations 62
7.1 Explicit Form of the Density Matrix 62
7.2 The General Form of Rotating Coordinates 63
7.3 Derivation of a Toy-Model Set of Optical Bloch Equations . 66

8 Conclusions 77
8.1 Results 77
8.2 Future Work 78

Bibliography 80

Appendices

A Waveform Generation Code 82

B Very Basic Things 86
B.1 The Center of Gravity 86
B.2 Diagonalizing the Hamiltonian 86
B.3 Rotating Coordinates 86
B.4 Lifetimes and Half-Lifes 87
B.5 Reduced Matrix Elements 88
B.6 Doppler Cooling Limit 88

List of Figures

2.1 Zeeman Shifts in a Magnetic Field 5
2.2 Diagram of a Magneto-Optical Trap 9
2.3 ^{41}K Transitions 10

3.1 AC-MOT Sample Magnetic Field 14
3.2 AC-MOT Sample Laser Polarization 14

4.1 Photo of the Offline MOT 16
4.2 Geometry of the Offline MOT 17
4.3 CCD Camera Output 18
4.4 Trap Lifetime Measurement 20
4.5 Trap Width Measurement 21
4.6 Offline Optical Setup 23
4.7 Trap Frequency and Laser Power 24
4.8 AC and DC Lifetimes 26
4.9 Lifetimes as a Function of AC Frequency 27

5.1 Methods for Killing the Trap 32
5.2 Trap-killing Methods, Trap Size, and Laser Power 33
5.3 Trap-killing Methods, Lifetime, and Laser Power 34
5.4 Lifetime and Duty Cycle 36
5.5 Fluorescence and Duty Cycle 37
5.6 Optimal Waveform to Minimize Residual Magnetic Field . . . 39
5.7 Offline Residual Magnetic Field 40

6.1 The Inside of the New Trapping Chamber 42
6.2 Quadrupole Coil Geometry in the Online Chamber 43
6.3 Inductance 46
6.4 Initial Hall Probes Layout 47
6.5 Magnetic Fields 48
6.6 Ceramic Feedthroughs 50
6.7 Acoustic Resonances in the New Chamber 51

6.8 Improperly-Tuned Sinusoidal Start 55
6.9 Current and Magnetic Field 56
6.10 Current and Magnetic Field: A Closer Look 57
6.11 Current and Magnetic Field: A Much Closer Look 58
6.12 Current in Top and Bottom Coils 59
6.13 Quadrupole and Dipole Components of the Magnetic Field . 60
6.14 A Fit to the Residual Quadrupole Field 61

7.1 D1 Transition Strengths for $I = 1/2$ 67

Acknowledgements

Special thanks to my research advisor John Behr, who was always willing to spend time helping students stuck at any level of cluelessness without making them feel stupid. For some reason, he also seemed to think it was worthwhile to pay me for doing things that were largely quite enjoyable.

I would also like to thank undergraduate researchers Heather Norton and Rhys Anderson, both of whom did a lot of the work that I wanted very much to avoid doing myself.

Chapter 1

Introduction and Motivation

1.1 Motivation

Since the magneto-optical trap (MOT) was first described in 1987 by Raab et. al. [1], it has become a standard technique for confining cold samples of neutral atoms. These cold trapped atoms may subsequently be used in the measurement of a variety of physical quantities.

The MOT necessitates the use of a magnetic field in order to produce a confining force on the trapped atoms. However, there exist a certain class of experiments which require a sample of cold atoms in zero (or minimal) magnetic field – notably any experiment in which high polarization of atomic angular momenta is needed. If a MOT is to be used in such a case, the trapping mechanism must be intermittently shut off for a period of time. Because the atoms have been cooled in the trap, they will disperse only slowly after discontinuation of the MOT's trapping forces, and it is possible to restart the MOT before most of the atoms have moved beyond the trapping region. It is during this "off" time that the atoms may be polarized by a properly-tuned laser if needed, and data may be collected with minimal interference from magnetic fields.

It is useful, therefore, to find a method to eliminate the magnetic field in the trapping region as rapidly as possible, so that a maximal amount of time can be spent collecting data. Recently Harvey and Murray [2] have built and described a new type of MOT designed to do just that–the AC-MOT, so named for the electrical current in the MOT's electromagnets. Previous generation of MOTs had used only DC currents for that purpose. Although the experimental setup for an AC-MOT is more complicated, the benefit is that the magnetic field can be eliminated much more quickly than is the case for a DC-MOT.

This thesis will describe and characterize many aspects of two AC-MOTs built for use in- or alongside nuclear beta decay experiments for the TRINAT research group.

1.2 Overview

The entirety of Chapter 2 is devoted to a description of the physical processes involved in a functional (AC- or DC-) MOT, and Chapter 3 describes the additional requirements for an AC-MOT.

We describe our own offline AC-MOT, including our commonly used measurement techniques, and characterize some of its properties in Chapter 4. Chapter 5 discusses and demonstrates optimal strategies for turning off trapping forces in the offline AC-MOT.

Chapter 6 deals only with the online AC-MOT. The setup is described, and some measurements relevant specifically to the online AC-MOT are presented.

In Chapter 7, attention is given to quantifying the polarization problems caused by residual magnetic fields. Beginning with a derivation of the well-known Optical Bloch Equations, we introduce terms into the Hamiltonian to model the effect of a non-zero magnetic field on the polarization of a sample of atoms. Qualitative results of this model are discussed.

Chapter 8 is a discussion which provides additional context for our results, and suggests possible future work on this topic.

Chapter 2

The Magneto-Optical Trap

Since its invention in 1987 [1], the Magneto-optical trap (MOT) has become a standard technique for creating samples of tightly-confined cold atoms. The key principle is to use a magnetic field gradient, in addition to lasers tuned near an atomic resonance, to cause atoms to absorb photons, pushing them toward the MOT centre and simultaneously cooling them.

In order to understand the mechanism by which a MOT is able to confine atoms, we must first introduce the Zeeman effect (Section 2.1) and a description of an optical molasses (Section 2.2). A functional MOT combines the forces resulting from these two mechanisms to trap and cool atoms.

2.1 The Zeeman Shift

The atomic Hamiltonian for an atom in the presence of a weak magnetic field (such as is present in a MOT) picks up an additional Zeeman shift term [3],

$$\hat{H}_{\text{Zeeman}} = -\vec{\mu} \cdot \vec{B}, \tag{2.1}$$

where the magnetic moment $\vec{\mu}$ is given by

$$\begin{aligned} \vec{\mu} &= -\mu_B \left(g_S \vec{S} + g_L \vec{L} + g_I \vec{I} \right) && (2.2) \\ &= -\mu_B \, g_F \, \vec{F} && (2.3) \end{aligned}$$

where μ_B is the Bohr magneton, and g_S, g_L, g_I, and g_F are the g-factors associated with electron spin, orbital angular momentum, nuclear spin, and total angular momentum, respectively. Typically, however, $g_I \ll g_S, g_L$ and so the nuclear spin term is neglected for the purpose of laser tuning for MOT operation. Then,

$$\begin{aligned} \vec{\mu} &\approx -\mu_B \left(g_S \vec{S} + g_L \vec{L} \right) && (2.4) \\ &= -\mu_B \, g_J \, \vec{J}, && (2.5) \end{aligned}$$

and Eq. 2.1 becomes

$$\hat{H}_{\text{Zeeman}} \quad = \quad g_J \, \mu_B \, \vec{J} \cdot \vec{B}. \tag{2.6}$$

If we take the direction of the magnetic field as our quantization axis and label it as $\hat{z}$, the result is a simple perturbation to atomic energy levels [3],

$$\Delta E_{\text{Zeeman}} \quad = \quad g_J \, \mu_B \, M_J B_z, \tag{2.7}$$

where we note that in the case where angular momentum $\vec{J}$ and magnetic field $\vec{B}$ are parallel, the Zeeman contribution to the total energy of that state is *positive.* This result is accurate for systems in which the magnetic field can be taken as "small", meaning that M_J and M_I are good quantum numbers.

It is convenient at this point to introduce new notation to describe the Zeeman contribution to a transition as a whole – including the Zeeman shifts in the ground and excited states within a single term. Thus, we define

$$\mu' := (g_e M_e - g_g M_g) \, \mu_B, \tag{2.8}$$

where $g_\times$ and $M_\times$ are the Lande g-factor and the $\hat{z}$ component of the angular momentum, and the subscripts 'g' and 'e' refer to the ground- and excited states, respectively. Then the change to the energy of a transition is

$$\Delta E_{\text{transition}} = \mu' B_z. \tag{2.9}$$

In a MOT, the magnetic field must be quadrupolar. In other words, although the magnetic field is zero at the centre, it increases linearly with distance in every direction. Thus, so too will the atomic energy levels vary linearly along the paths of the beams of light, as shown in Fig. 2.1.

2.2 Atoms in an Optical Molasses

We will now consider a system of two-level atoms located at the intersection of two counter-propagating laser beams, detuned slightly from the atomic resonance. Such a setup is sometimes referred to as a one-dimensional "optical molasses" due to the viscous drag force induced on atomic motion, which will be discussed in more detail shortly.

In such a system, an incident photon can excite an atom from the ground state into the excited state, while simultaneously giving the atom a "push" proportional to the laser's detuning from the atomic resonance. An excited

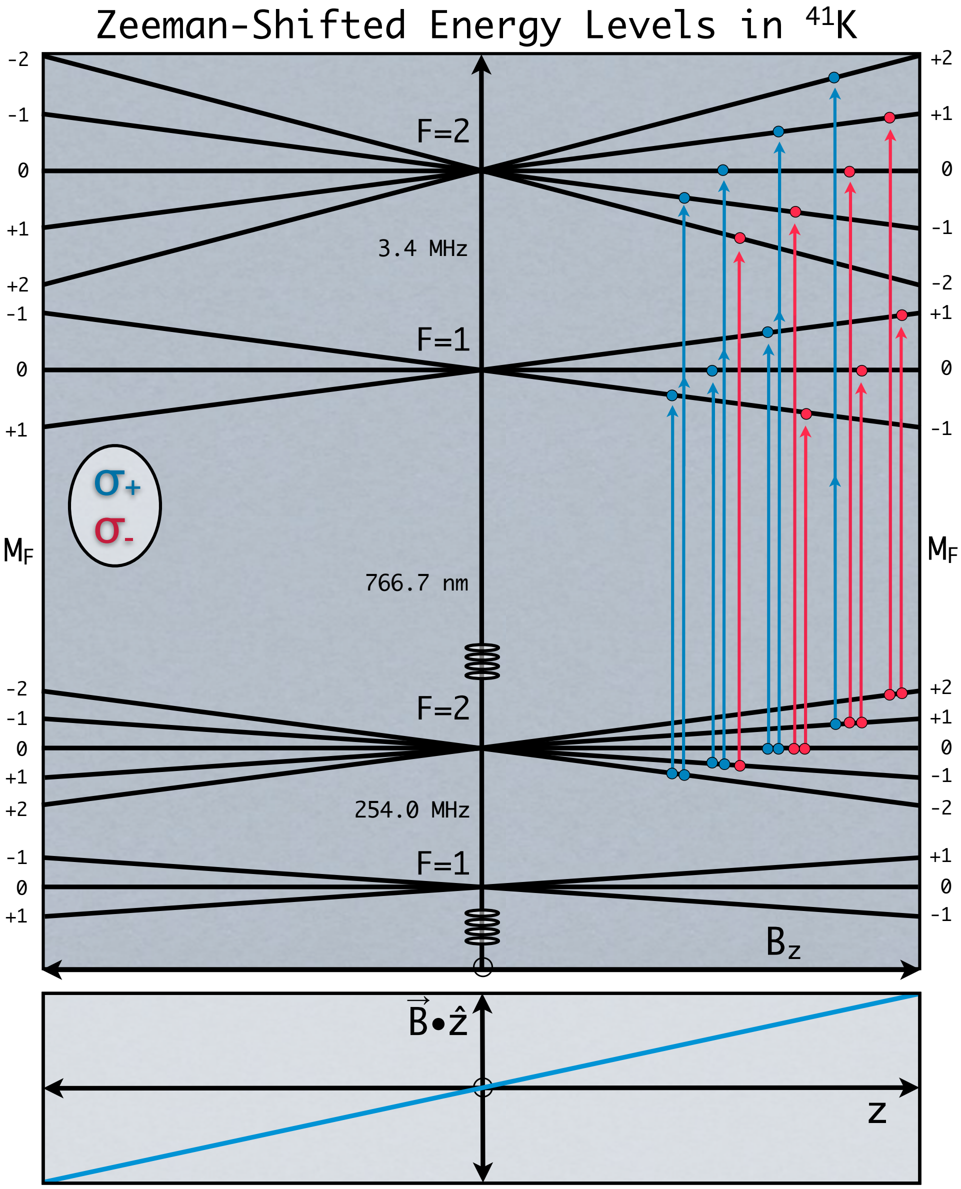

Figure 2.1: A level diagram to show the perturbation to hyperfine energy levels in ^{41}K resulting from a linear magnetic field gradient such as is used in a MOT.

atom will eventually spontaneously decay back into its ground state, emitting another photon in a random direction during the process. Thus, the atom's overall motion within an optical molasses is partly determined by the balance of laser intensities, and part random walk.

Additionally, laser light can also stimulate an excited atom to emit a photon and decay back to its ground state. This effect is negligible provided that the laser's intensity is sufficiently small, but as the laser intensity increases, so too does this effect. In the limit of infinite intensity, stimulated emission is just as likely to occur as stimulated excitation, and as a result, the atomic population is split evenly between the ground and excited states.

To describe the transition between these two regimes, we introduce the saturation intensity, I_{sat}, which is the intensity at which the decay rate by spontaneous emission is equal to the decay rate from stimulated emission for a laser tuned precisely to the atomic resonance. For an atomic transition of linewidth γ (equivalently, the linewidth γ describes the spontaneous decay rate, and is the inverse of the excited state's lifetime, so that $\gamma = 1/\tau$) and energy $\hbar\omega_0$, the saturation intensity is

$$I_{\text{sat}} = \frac{\hbar\,\omega_0^3\,\gamma}{12\pi\,c^2}. \tag{2.10}$$

Then, we can describe the intensity I of the on-resonance light within a particular system in terms of its relation to the saturation intensity by introducing s_0, the on-resonance saturation parameter, so that

$$s_0 := \frac{I}{I_{\text{sat}}}. \tag{2.11}$$

In practice, it is often useful to detune the lasers slightly from the resonant transition. We now introduce the detuning parameter,

$$\delta_0 := \omega_L - \omega_0 \tag{2.12}$$

which describes the difference between the laser frequency and the atomic resonance frequency. In such a situation, we still wish to be able to describe the extent to which the transition is saturated by the laser light. We therefore introduce the off-resonance saturation parameter, s, which is related to s_0 by

$$s := \frac{s_0}{1 + (2\delta_0/\gamma)^2}. \tag{2.13}$$

For atoms at rest in an optical molasses, the excited state population fraction is given by

$$\rho_{ee} = \frac{s}{2(s+1)} = \frac{s_0/2}{1 + s_0 + (2\delta_0/\gamma)^2}. \tag{2.14}$$

This result emerges as a steady-state solution to the two-level Optical Bloch Equations. (For a more in-depth treatment of the Optical Bloch Equations, see Chapter 7.) It should be clear that in the limit of large s values, ρ_{ee} approaches 1/2 as expected. Due to the very nature of a steady state solution, the rate at which atoms are excited to the higher energy level is equal to the rate at which atoms decay to the ground state. Therefore, the total scattering rate R for photons incident on atoms at rest in an optical molasses is given by [4]

$$R = \gamma\rho_{ee} = \frac{\gamma\, s_0/2}{1 + s_0 + (2\delta_0/\gamma)^2}. \tag{2.15}$$

Since every photon absorbed transfers to the atom a momentum of

$$\Delta\vec{p} = \frac{\hbar\,\omega_L}{c}\,\hat{e}_L, \tag{2.16}$$

where $\hat{e}_L$ is a unit vector in the direction of the laser's propagation, we are able to write out an expression for the average force on an atom at rest within a single laser beam. Trivially, the average force must be the momentum transferred multiplied by the rate at which this momentum transfer occurs, and so we find that in general,

$$\begin{aligned} \vec{F}_1 &= R\,\Delta\vec{p} & (2.17)\\ &= \frac{\gamma\, s_0/2}{1 + s_0 + (2\delta_0/\gamma)^2}\left(\frac{\hbar\,\omega_L}{c}\right)\hat{e}_L. & (2.18)\end{aligned}$$

Note that Eq. 2.18 need not include any contribution from spontaneous emission following absorption of a photon, because the (vector) average of any such contribution must be zero, since there is no preferred direction of spontaneous emission.

Of course, we cannot assume that atoms within the optical molasses will be at rest. For an atom moving with 3-velocity $\vec{v}$, an incident laser beam will be observed to have a Doppler shifted frequency ω'_L, so that

$$\omega_L \to \omega'_L(\vec{v}) \quad := \quad \omega_L\left(1 - \frac{\vec{v}\cdot\hat{e}_L}{c}\right) \tag{2.19}$$

within the atom's reference frame. (Note that as expected, the Doppler shifted frequency increases if the direction of atomic motion is anti-parallel to the direction of laser propagation.) This effective frequency shift propagates through to the equations of force, showing up everywhere the laser's frequency is referenced.

We now return to consideration of the average force within a single beam. With the Doppler shift taken into consideration, Eq. 2.18 becomes

$$\vec{F}_1'(\vec{v}) \quad = \quad \frac{\gamma\left(s_0\,\hbar\,\omega_L/(2c)\right)(1-\vec{v}\cdot\hat{e}_L/c)}{1+s_0+\left(\frac{2}{\gamma}(\delta_0-(\omega_L/c)\,\vec{v}\cdot\hat{e}_L)\right)^2}\,\hat{e}_L. \tag{2.20}$$

Therefore the net force on an atom moving with velocity $\vec{v}$ within two such counter-propagating laser beams (that is, one beam propagates in direction $+\hat{e}_L$, while the other propagates in direction $-\hat{e}_L$) is given by

$$\begin{aligned}\vec{F}_{\mathrm{OM}}(\vec{v}) \quad = \quad & \frac{\gamma\left(s_0\,\hbar\,\omega_L/(2c)\right)(1-\vec{v}\cdot\hat{e}_L/c)}{1+s_0+\left(\frac{2}{\gamma}(\delta_0-(\omega_L/c)\,\vec{v}\cdot\hat{e}_L)\right)^2}\,\hat{e}_L \\ & -\frac{\gamma\left(s_0\,\hbar\,\omega_L/(2c)\right)(1+\vec{v}\cdot\hat{e}_L/c)}{1+s_0+\left(\frac{2}{\gamma}(\delta_0+(\omega_L/c)\,\vec{v}\cdot\hat{e}_L)\right)^2}\,\hat{e}_L. \end{aligned} \tag{2.21}$$

2.3 The Magneto-Optical Trap

We now turn our focus to a description of a MOT. To create a MOT, a linear magnetic field gradient must be applied on top of an optical molasses. By taking advantage of the change in absorption from the Zeeman effect's perturbation to atomic resonances, atoms can be preferentially pushed towards a central region, where the Zeeman shift is zero.

To create the appropriate magnetic field, one employs a set of two electrical coils with antiparallel currents, so that the magnetic field is zero at the trap's centre, but its local gradient is non-zero; in the immediately surrounding region the magnitude of the magnetic field grows linearly with distance in any direction. The atomic energy levels are perturbed as a result, and the MOT uses a series of six laser beams (three sets of two anti-parallel 'twin' beams), all intersecting at the trap's centre, to take advantage of these energy perturbations to produce a confining force on the atoms. The geometry of a MOT in a laboratory is shown in Fig. 2.2.

The six beams of light must each consist of two frequency components, referred to here as the "trapping frequency" and the "repumper frequency" [4]. Examination of Fig. 2.3 shows why this must so – without the addition of a repumper component, it wouldn't be long before the trapped atoms all decayed into the "wrong" ground state, from which the original trapping laser could not excite them. For optimal MOT function, both the trapping

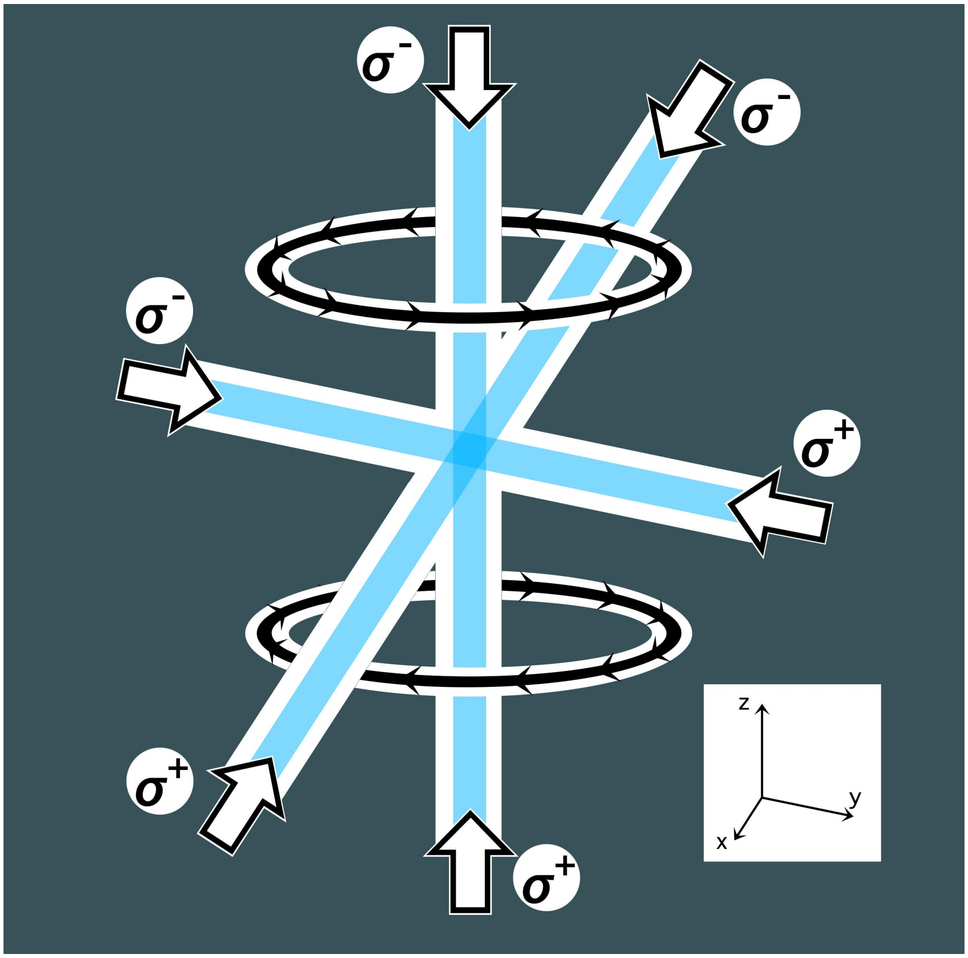

Figure 2.2: The necessary components of a magneto-optical trap include two electrical coils running anti-parallel currents, and six beams of light intersecting at the centre of the geometry. The electrical coils produce a quadrupolar magnetic field. Each beam of light consists of two frequency components – the "trapping" and "repumper" beams, and all are circularly polarized and counter-propagating, so as to couple to specific atomic energy transitions.

and repumper components should be red-detuned from their respective transitions. Typically, a MOT has much more power in the trapping component than the repumper component.

The reasons for red-detuning the lasers are twofold. The first reason

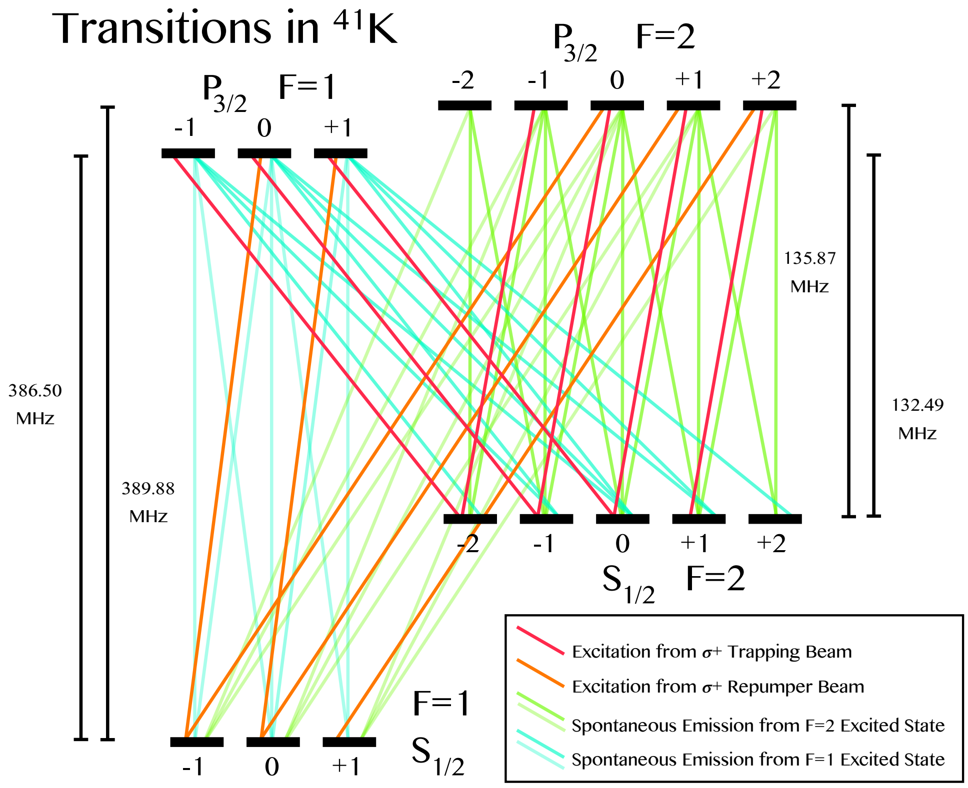

Figure 2.3: Hyperfine transitions in ^{41}K – Zeeman splitting of the hyperfine states is not shown. This diagram shows only the absorption transitions which couple to σ_+ light. An absorbed laser beam with σ_+ polarization must increase the atom's angular momentum projection along the axis of propagation. We see this as a change in the quantum number M_F by one unit, so as to conserve angular momentum. By a similar argument, absorption of σ_- light will decrease M_F by one unit. For spontaneous emission, there is no requirement on the direction or polarization of the spontaneously emitted photon, so the process can change M_F by 0, +1, or -1.

is that the atoms which are moving quickly antiparallel to the direction of the laser's propagation will see the light as being blueshifted closer to resonance; photons will then be preferentially absorbed by these atoms, and the imparted change in momentum will cause the atom to slow. By a similar argument, atoms moving parallel to the direction of light propagation are less likely to absorb a photon. This is the mechanism at work in an optical molasses, and the forces involved have been quantified in Section 2.2 The second reason for the detuning is simply a matter of selecting which side of the cloud of trapped atoms is more likely to absorb a photon propagating in a particular direction – the goal of course being that the absorbed linear momentum should push the atoms toward the central trapping region. Thus, when the beam interacts with the atoms near the centre of the trapping region, it has the dual effects of slowing the atoms and pushing them towards the centre [1].

We now turn to a mathematical description of the forces within a one-dimensional MOT. Although it can be rigorously shown that a MOT is able to confine atoms in three dimensions, as in [5], to aid clarity of description we will consider only a one-dimensional MOT for the remainder of this section. In effect, this means that we will apply the effects of a linearly changing Zeeman shift, described in Section 2.1, to the optical molasses described in Section 2.2. In these sections, no consideration was given to the polarization of the incident laser, but this matter can no longer be ignored. As can be seen in Figs. 2.1 and 2.3, an incoming laser with σ_+ polarization will interact with a different set of atomic transitions than it would when its polarization was σ_-, and in particular, swapping both the sign of the magnetic field and the polarization of the laser will lead to an indentical set of couplings between the atom and the laser, with an identical set of energy perturbations to transitions.

We will proceed by adding the Zeeman shift terms into Eq. 2.20. The presence of a Zeeman shift will change the effective value of the atomic resonance, ω_0 (rather than ω_L) in a manner which depends on the polarization of the incident laser. Therefore, for a σ_- or σ_+ laser respectively, the atomic resonance to which the laser couples becomes:

$$\omega_0 \to \omega_0'^{\pm}(\vec{r}) \quad := \quad \omega_0 \pm \mu' B_z(\vec{r})/\hbar \tag{2.22}$$

where μ' is as described in Eq. 2.8. This change makes its way through the calculations, showing up everywhere that ω_0 shows up. Eq. 2.20 becomes

$$\vec{F}_1^{\pm}(\vec{v}, B_z) \quad = \quad \frac{\gamma\left(s_0\,\hbar\omega_L/(2c)\right)(1 - \vec{v}\cdot\hat{e}_L/c)}{1 + s_0 + \left(\frac{2}{\gamma}(\delta_0 - (\omega_L/c)\,\vec{v}\cdot\hat{e}_L \mp \mu' B_z(\vec{r})/\hbar)\right)^2}\,\hat{e}_L. \tag{2.23}$$

In a MOT, we will wish to avoid the scenario in which the atoms are all optically pumped into one particular energy level, so we select one laser to have σ_- polarization, and its counterpropagating twin must have σ_+ polarization. It is important that the *correct* beam be given the correct polarization, and to do that we recall that in a MOT, we wish to preferentially push atoms toward the centre of the trap, therefore the absolute value of the effective detuning must be smaller in regions further from the centre. If we use the magnetic field gradient shown in Fig. 2.1 and consider only the trapping beam, then μ' takes the same sign as the $\sigma_\pm$ polarization (We will write this explicitly as $\mu'_\pm$ for clarity, remembering that $\mu'_- = -\mu'_+$.). We therefore choose the σ_- light to propagate in the $+\hat{z}$ direction, and the σ_+ light to propagate in the -$\hat{z}$ direction, and Eq. 2.23 becomes

$$\vec{F}_1^+(\vec{v}, B_z) = \frac{-\gamma\left(s_0\,\hbar\omega_L/(2c)\right)(1+\vec{v}\cdot\hat{z}/c)}{1+s_0+\left(\frac{2}{\gamma}(\delta_0+(\omega_L/c)\,\vec{v}\cdot\hat{z}-\mu'_+B_z(\vec{r})/\hbar)\right)^2}\hat{z} \tag{2.24}$$

$$\vec{F}_1^-(\vec{v}, B_z) = \frac{\gamma\left(s_0\,\hbar\omega_L/(2c)\right)(1-\vec{v}\cdot\hat{z}/c)}{1+s_0+\left(\frac{2}{\gamma}(\delta_0-(\omega_L/c)\,\vec{v}\cdot\hat{z}+\mu'_-B_z(\vec{r})/\hbar)\right)^2}\hat{z}, \tag{2.25}$$

and the total average force on an atom within a MOT is simply the sum of these two terms. Because we have chosen to work in a system where the magnetic field along the $\hat{z}$-axis is given by

$$B_z = \frac{\partial B}{\partial z}z, \tag{2.26}$$

we can now write the average force in terms of the atom's position. We find that

$$\begin{aligned}\vec{F}_{\mathrm{MOT}}(\vec{v}, z) &= \frac{\gamma\,s_0\,\hbar\omega_L}{2c}\hat{z} \\ &\times\left[\frac{-1-\vec{v}\cdot\hat{z}/c}{1+s_0+\frac{4}{\gamma^2}\left(\delta_0+(\omega_L/c)\,\vec{v}\cdot\hat{z}-\mu'_+\frac{\partial B}{\partial z}z/\hbar\right)^2}\right. \\ &\left.+\frac{1-\vec{v}\cdot\hat{z}/c}{1+s_0+\frac{4}{\gamma^2}\left(\delta_0-(\omega_L/c)\,\vec{v}\cdot\hat{z}+\mu'_-\frac{\partial B}{\partial z}z/\hbar\right)^2}\right]\end{aligned} \tag{2.27}$$

gives the average force on an atom within a MOT.

Chapter 3

The AC-MOT–What Makes It Different?

For our experiment, we need atoms which are not only cold and well confined, but spin polarized as well. Although the standard “DC” MOT has previously been demonstrated to trap and cool atoms in a confined region, it requires the use of a non-uniform magnetic field, which hinders our ability to polarize the atoms. Our challenge is to create an atom trap from which the magnetic non-uniformities can be eliminated rapidly. To that end, we have implemented an AC-MOT – a MOT in which the magnetic field generating coils are run with an AC electrical current, and laser polarizations are switched rapidly so as to match. This setup minimizes problems from residual eddy currents in nearby conductors, allowing us to eliminate the magnetic field much more rapidly [2]. With the quadrupole component of the magnetic field gone, the sample of cold atoms can be better polarized before they disperse.

To effect these goals, an “AC-MOT” was designed and constructed, initially by Harvey and Murray [2]. The principle was straightforward: instead of directing a DC current through the trap’s anti-Helmholz coils, an AC current would be used. Additionally, the polarization of the trapping lasers would need to be alternated synchronously with the current. In this way, although both the polarity of the magnetic quadrupole field and the laser polarization varied, a trapping force would remain.

By using a system in which the current is expected to vary, it becomes easier to shut the current off rapidly. In particular, it is possible to select a cut-off time for the current such that the residual magnetic field from eddy currents is minimized.

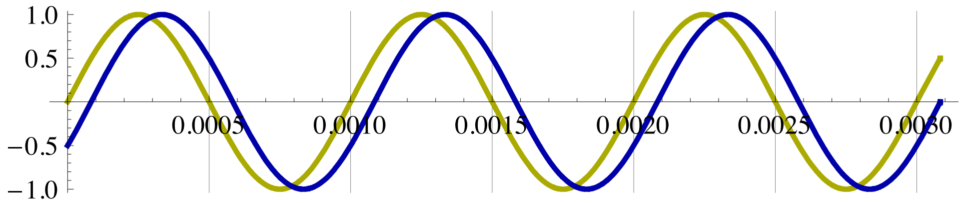

Figure 3.1: Sample waveform for use in an AC-MOT. Magnetic field (blue) lags current through quadrupole coils (yellow) slightly as a result of eddy currents in nearby conductors.

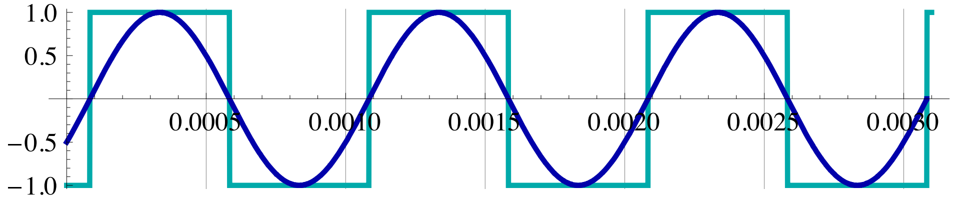

Figure 3.2: Laser polarization (cyan) is kept in phase with the magnetic field (blue), such that a trapping force is present at all times.

For systems in which the transient response time of the AC-MOT coils is much faster than that of the surrounding materials, we can describe the eddy currents after shutting off an AC-MOT driven by a voltage-controlled amplifier, which in turn is driven by a signal of $V = V_0 \sin(\omega t + \phi)$, by

$$I_{\text{eddy}}(\phi, t) = I_0 \frac{\omega\tau\cos(\omega t + \phi) - \sin(\omega t + \phi) + (\sin\phi - \omega\tau\cos\phi)e^{-t/\tau}}{1 + \omega^2\tau^2}, \quad (3.1)$$

where τ is a constant that depends on the properties of nearby materials. One can see from this expression that, given an equal number of half-cycles, a choice of $\phi = \tan^{-1}(\omega\tau)$ results in the eddy currents being zero after the AC-MOT is shut off [2].

Chapter 4

The Offline AC-MOT

In order to test the usefulness of the AC-MOT for our purposes, we initially implemented an AC-MOT in our “offline” geometry, which was never intended to be used for our final experiment. This allowed us to examine systematic effects in advance of the arrival of the “online” chamber. Additionally, because our intent for the online setup was to trap ^{37}K, which is radioactive with a half-life of 1.2s, it was not possible to work directly with this isotope during much of the setup and optimization processes. Instead, we chose to work primarily with (stable) ^{41}K, which was an ideal candidate because its hyperfine structure is similar to that of ^{37}K.

Our offline setup, shown in Fig. 4.1 included a vacuum-pumped pyrex cell with a connected potassium dispenser, and vertically oriented anti-Helmholz coils external to the cell. In the AC-MOT, these coils carry a sinusoidally varying current. The optical details (shown explicitly in Fig. 4.6) are very similar to those one might use in a typical DC-MOT, with the notable addition of an electro-optic modulator (EOM), used to rapidly flip the polarization of the laser light between two perpendicular linear polarization states. The geometry of the current-carrying magnetic field coils is shown in Fig. 4.2.

4.1 Methodologies for Measuring Trap Characteristics

In order to evaluate a variety of trap properties, we used a CCD camera to capture images of the trapping region. Typical results are shown in Fig. 4.3. Each such image requires a camera exposure that $\sim$ 10 - 100 of milliseconds, limiting our ability to record rapid changes to the atom cloud. Because a full AC cycle takes only $\sim$ 1 millisecond, this technique is not able to tell us anything about the cloud during different phases of the AC trapping cycle. Instead, we examine images taken over a period of *many* AC cycles to learn about overall, time-averaged characteristics of the AC-MOT.

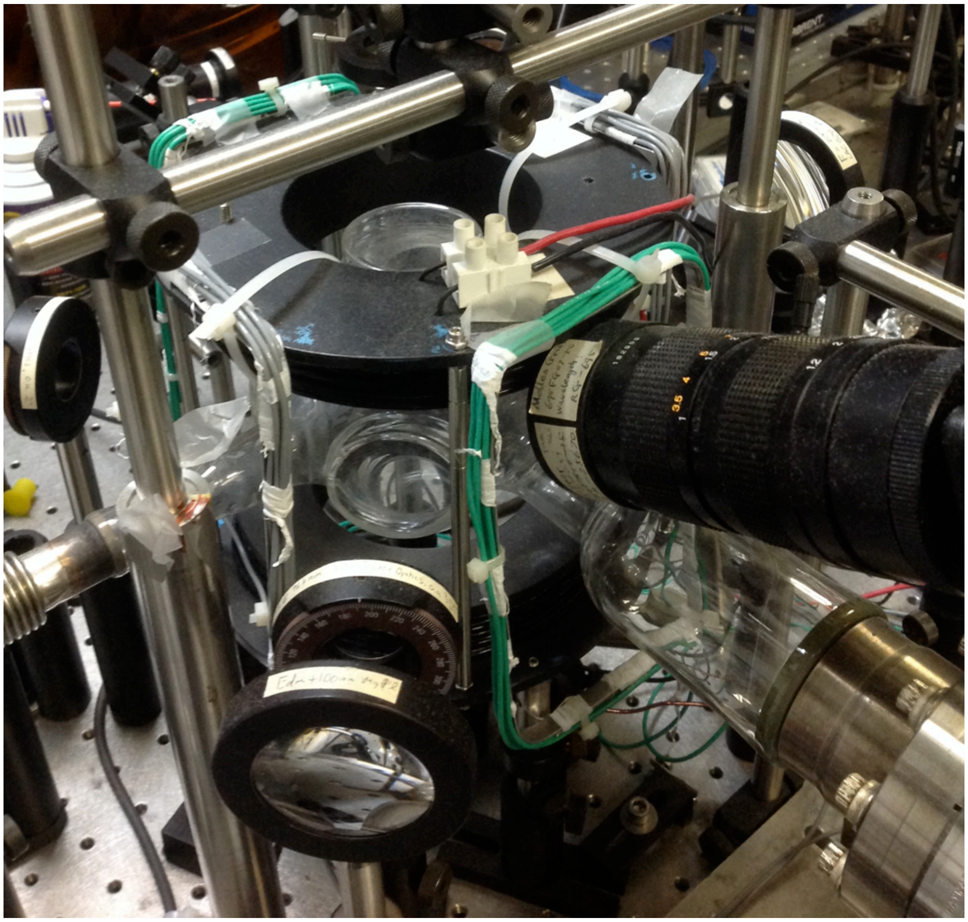

Figure 4.1: A photo of the offline MOT's vacuum-pumped pyrex cell and vertically-oriented current-carrying coils. The CCD camera used for fluorescence and lifetime measurements is visible on the right centre, and the potassium vaporizer is located beyond the port in the lower right corner. Trim coils are used to keep the magnetic field at the centre of the pyrex cell at zero, and the green and grey trim coils are clearly visible in this picture. The vertical trim coils cannot be seen, as they are wound about the same rings that contain the vertical quadrupole coils. To complement this photograph, a schematic of the coils' geometry is shown in Fig. 4.2, and the optics setup is shown in Fig. 4.6.

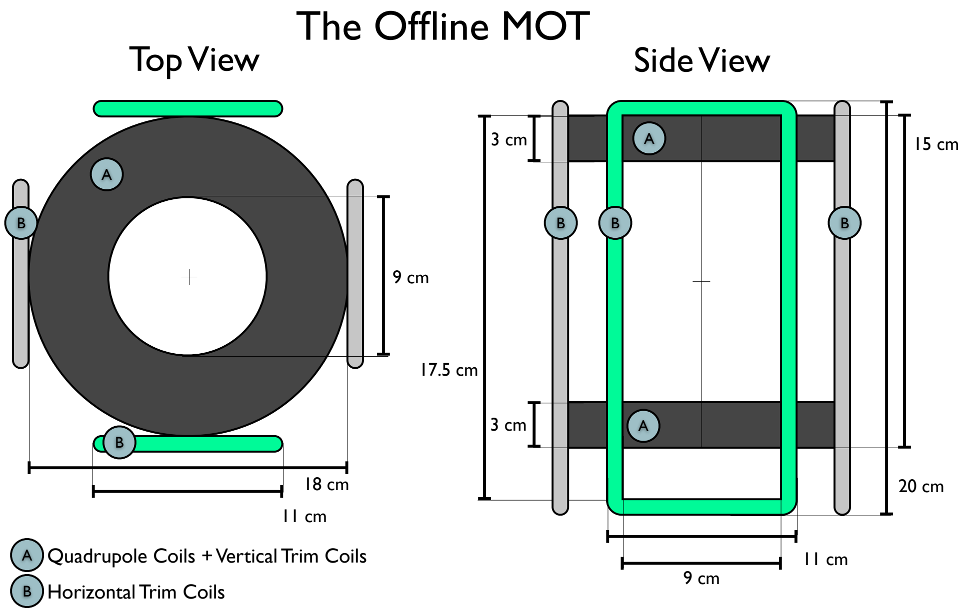

Figure 4.2: Geometry of the Offline MOT. Note that there are three separate sets of ‘trim coils’, used to adjust the DC components of the magnetic field, such that the Zeeman shift is zero at the centre of the trap (the vertical trim coils are separate from the quadrupole coils, despite being located within the same plastic frame). In practice, the current in these trim coils was set so as to optimize the appearance of the cloud of trapped atoms – a method which seemed to work reasonably well for us, given the fact that the local magnetic field in our lab could be measurably altered by the status of TRIUMF’s cyclotron (below our lab), or the operation of certain equipment for other experiments (above our lab).

4.1.1 Measuring the Number of Trapped Atoms

In order to determine the number of atoms in the trap at any given time, a smaller region of interest is selected (see Fig. 4.3), and the background brightness is subtracted off, pixel by pixel. Then, the overall trap fluorescence is given by the sum of the brightness for each pixel within the region of interest. Because trap fluorescence is expected to be proportional to the number of trapped atoms, this type of measurement tells us how many atoms we are able to trap at a particular time up to an overall scaling factor, provided that parameters such as laser power and frequency are kept constant. In the majority of cases examined within this document, we will be interested only in the way the number of trapped atoms scales – not in the total number of atoms.

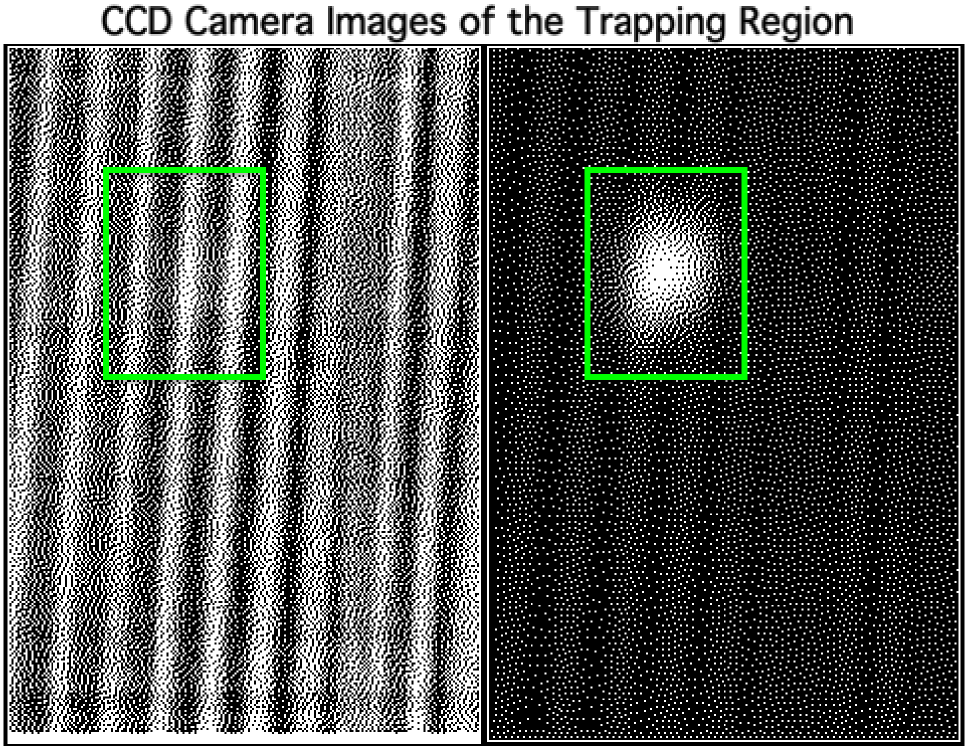

Figure 4.3: Images of the trapping region as collected by a CCD camera. The image on the right shows a cloud of atoms trapped in a MOT, while the image on the left shows the background for the same spatial region, collected while the laser light was present but the magnetic field had been turned off. Each pixel from the CCD camera's image has a 'brightness' value ranging from 0 to 255. In order to make sense of the results, it is usually necessary to consider only some smaller region of interest immediately surrounding the cloud of atoms, and subtract the background image from the trap image, pixel by pixel, before analyzing the results. The green rectangles show a typical region of interest.

4.1.2 Measuring the Lifetime

Because we are in a regime of low density, the number of trapped atoms $N(t)$ in a MOT with trap lifetime τ will obey the equation

$$\frac{\mathrm{d}N(t)}{\mathrm{d}t} = N_0\, e^{+t/\tau} \tag{4.1}$$

while it is loading. We therefore chose to measure the lifetime by determining the rate at which atoms are loaded into the trap, as shown in Fig. 4.4. Beginning from a state with no trapped atoms, the conditions necessary for trapping are created, and the total fluorescence in the region of interest is monitored intermittently over a period of several seconds.

In order to obtain a measurement of the trap lifetime, we record a background image followed by a series of images of the trap over a period of time. To increase the signal-to-noise ratio, the cloud of trapped atoms may be destroyed and fluorescence measurements repeated over again several times.

One notable pitfall that must be avoided when measuring the trap lifetime in this manner is setting an incorrect region of interest. As one might expect, the cloud has been observed to move slightly when trap settings are adjusted. While position stability is largely a non-issue in the online AC-MOT, the offline setup was prone to a variety of systematic effects that were not necessarily consistent from day to day (described further in Section 4.5). Unfortunately, if the region of interest is set to be too large, the signal is overwhelmed by the noise and cannot be used. Therefore it was necessary to double check, for each such lifetime measurement, that the cloud was positioned where it was expected to be–within our defined region of interest.

4.1.3 Measuring the Trap Width and Position

We are also sometimes interested in measurements of the size and position of the trap. In the offline AC-MOT, we were limited to using the CCD camera for such measurements, and even in principle one CCD camera would only allow us to measure the width and position along two of the three spatial dimensions. In practice, however, we used only one dimension, because the pronounced vertical streaks in the camera output (see Fig. 4.3) make it difficult to work with.

Once the CCD camera has collected an image, the brightnesses of its pixels are projected along its two axes, and gaussian curves are fit to the result, as shown in Fig. 4.5. Fig. 4.5 also demonstrates the problem inherent

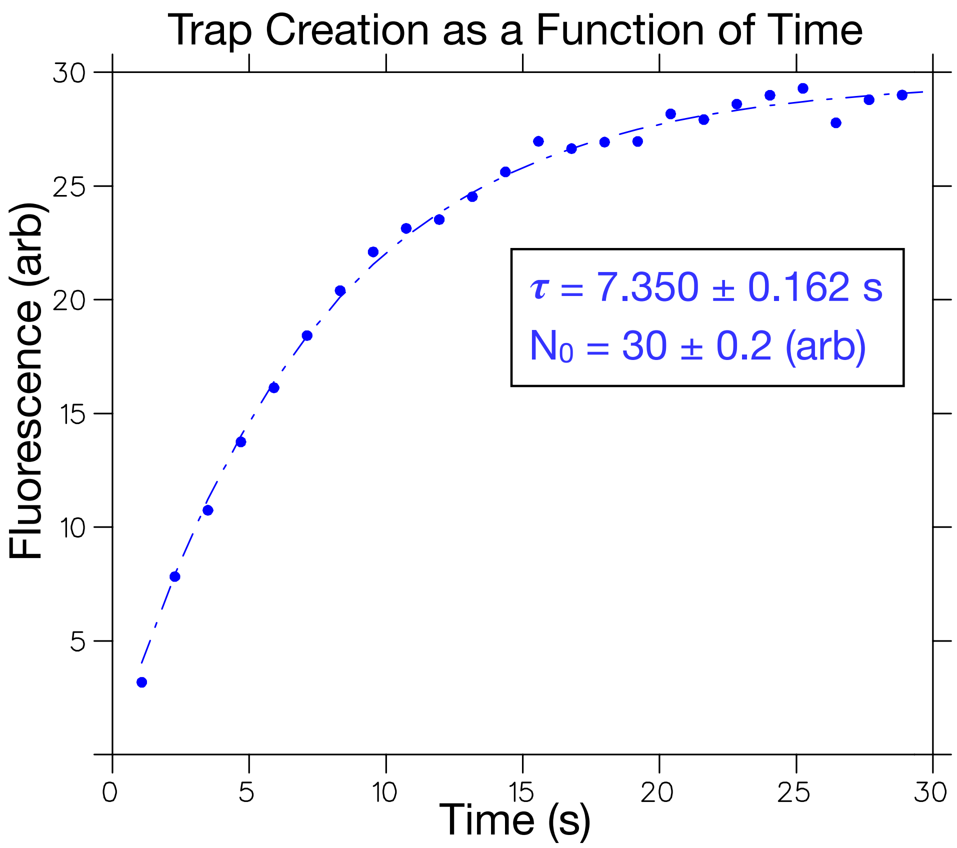

Figure 4.4: A typical set of reduced fluorescence data from the CCD camera, used to extract AC-MOT lifetimes. The quantity plotted on the vertical axis is the fluorescence measured only within a pre-defined region of interest, after the background brightness has been subtracted off. At t=0, when the conditions necessary for trapping begin, there is no cloud of trapped atoms present. The fluorescence is measured at time intervals spanning a period of several seconds, at which point the trapping mechanism is removed and the atoms are allowed to disperse. Once the cloud has been completely destroyed, the measurements may be repeated again as the number of trapped atoms grows again. To obtain a plot such as this, with sufficiently clean data, the cycle of measurements is repeated 3 to 5 times. A fit is then performed to extract the trap lifetime τ, which is described by Eq. 4.1.

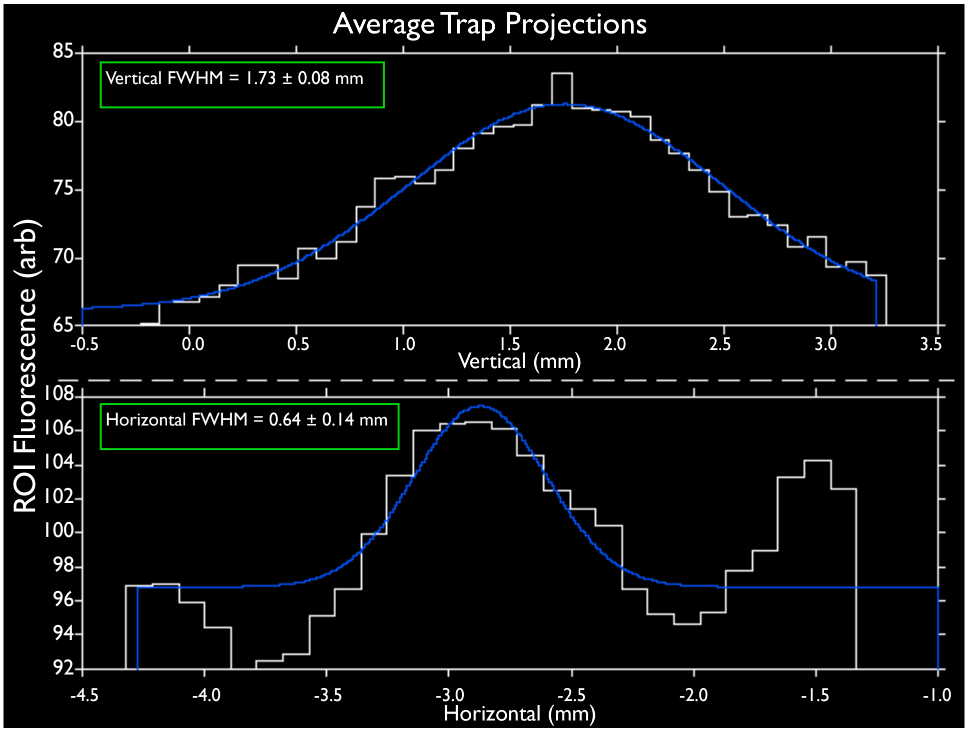

Figure 4.5: A typical set of trap fluorescence projections along the vertical and horizontal axes. The projections are fit to a gaussian, and the FWHM used to characterize cloud width. In these plots, the background fluorescence has been subtracted off–however the vertical lines (as seen in Fig. 4.3) are not steady from image to image, and so they are still prominently visible in the horizontal projection. The result of this is that our horizontal trap width measurements are not particularly reliable. In this thesis, when the trap width is mentioned without explicitly stating an axis of projection, it should be assumed that a vertical projection is being used.

in working with fluorescence projections along the horizontal axis within our system. The 'full width at half maximum' (FWHM) of the vertical projection's gaussian is used to characterize the cloud's width, and its centre is used to describe the cloud's position.

4.2 Laser Frequency Calibrations in the Offline AC-MOT

One aspect of optimal MOT operations is that of tuning the lasers to optimal frequencies. In many setups, the precise parameters of the MOT's repumper beam are of secondary importance to the MOT's operation. However, as can be seen in Fig. 2.3 for ^{41}K, the repumper component in our MOT is actually quite important, due to the proximity of the $F = 1$ and $F = 2$ excited states to one another. That is, a high fraction of the atoms excited by the trapping laser will end up in the 'wrong' excited state, increasing the likelihood that they will decay to the 'wrong' ground state – therefore the repumper component of the MOT's laser beams plays a relatively large role.

The optical setup in our offline AC-MOT is shown in Fig. 4.6, and the variable subscripts in Eqs. 4.2 and 4.3 make reference to that diagram. The trapping frequency, f_{trap} and the repumper frequency, f_{repump} in this system can be described by

$$\begin{aligned} f_{\text{trap}} &= f_{\text{lock}} - f_{\text{AOM A}} - f_{\text{AOM B}} && (4.2) \\ f_{\text{repump}} &= f_{\text{trap}} + f_{\text{VCO}}. && (4.3) \end{aligned}$$

We chose to lock the laser to the spectral peak at approximately 277.4 MHz from the centre of gravity in ^{39}K. This peak was the result of a combination of two different D2 transitions in ^{39}K: $F = 1 \rightarrow F = 1$ (272.7 MHz) and $F = 1 \rightarrow F = 2$ (282.0 MHz) [6, 7]. The relative strengths of these two transitions in our vapor cell is unclear, therefore there exists some systematic uncertainty in the absolute value of all measured frequencies which depend on the laser's lock point.

In order to produce the desired coupling to both the $F = 2 \rightarrow F = 1$ and $F = 2 \rightarrow F = 2$ D2 transitions (132.49 MHz and 135.87 MHz, respectively, from the centre of gravity [6, 7]), the laser frequency was adjusted from its lock point by passing it through two AOMs. To produce a laser beam tuned to +130 MHz (that is, slightly red-detuned from both resonances), AOMs A and B were adjusted to decrease the frequency of the laser light passed through them by a total of 147 MHz. We took this as our starting trap frequency.

Sidebands were added next – initially at $f_{\text{VCO}} = 241$ MHz, and the sideband with the positive detuning was used as the repumper. This produced a repumper frequency of +371 MHz – red-detuned from the D1 transitions at +386.5 MHz ($F = 1 \rightarrow F = 1$) and +389.88 MHz ($F = 1 \rightarrow F = 2$) [6, 7].

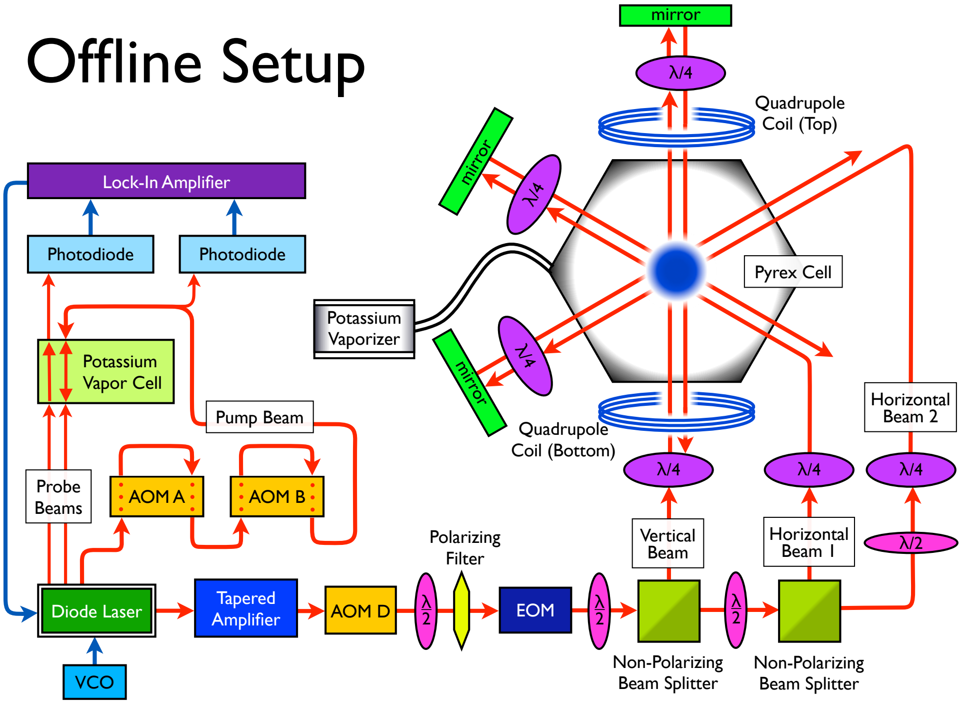

Figure 4.6: A diagram of the components of the offline AC-MOT. The geometric layout of the current-carrying magnetic field coils is shown in Fig. 4.2. The basic design is similar to that of a typical DC-MOT. The laser is locked to a chosen carrier frequency by using standard saturation spectroscopy techniques, and a voltage-controlled oscillator (VCO) is used to add sidebands above and below the carrier frequency. AOM D is used only to turn the light on and off. The EOM is used as a rapidly-changing variable wave plate. Tuned properly, it is able to adjust a polarized laser beam passing through it to either of two perpendicular linear polarization states, which is essential for the operation of an AC-MOT. Subsequent half-wave plates are used to adjust the polarization directions (in both states) so as to minimize ellipticity after the laser passes through beam splitters, and quarter wave plates are used immediately before the beams enter the trapping chamber so as to produce circular polarization. Thus, when the direction of linear polarization is switched by ninety degrees at the exit from the EOM, the direction of circular polarization of the light in the chamber is also switched.

In Fig. 4.7, the trap frequency f_{trap} was swept while keeping the repumper frequency fixed by a method in which f_{VCO} and $f_{\text{AOM B}}$ were swept together, such that their combined contribution to f_{repump} was constant. However since f_{VCO} does not contribute to f_{trap}, the change in $f_{\text{AOM B}}$ also produced a change to f_{trap}.

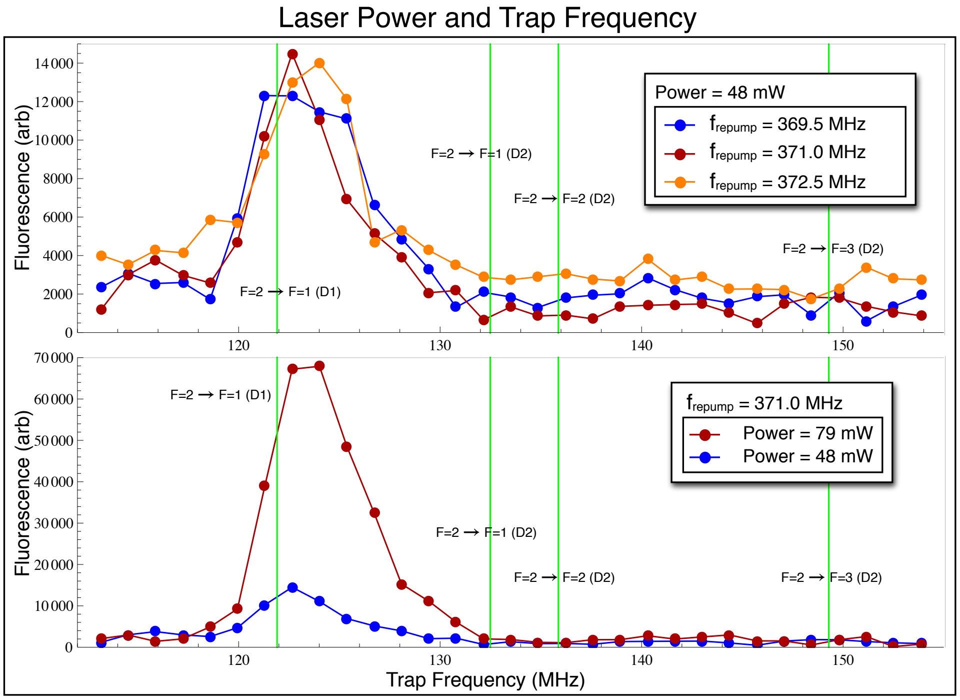

Figure 4.7: The relationships between trapping frequency, repumper frequency, laser power, and trap fluorescence are shown here. Power measurements were taken after the EOM (as shown in Fig. 4.6), and would include the trapping frequency component of the laser beam as well as the two sidebands, each of which has about 10% the power of the carrier frequency component. One of these sidebands functions as the repumper, and the other is simply ignored as it is not close to any atomic resonances. Fluorescence is measured according to the procedure described in Section 4.1.1, though we do not interpret the overall fluorescence as proportional to the number of trapped atoms here, since a varying laser frequency will also have a large effect on the fluorescence for any particular trapped atom.

4.3 The Phenomenology of Lifetime Measurements in the AC- and DC-MOT

It is interesting to consider the relationship between lifetimes in AC- and DC-MOTs. Fig. 4.8 shows that lifetimes for an AC-MOT are significantly shorter than those measured in a DC-MOT under similar operating conditions.

One possible reason for the experimentally measured decreased lifetime is that in an AC-MOT, the restorative 'spring' force resulting from the Zeeman shift is eliminated or decreased during some fraction of each AC cycle. The author speculates that if this were the case, it might be possible to bring the results into closer agreement if the laser frequencies were tuned closer to resonance, so as to make the trapped atoms colder. Unfortunately, this has never been attempted.

Another possible interpretation for this result is that our loss mechanisms in the offline AC-MOT are dominated by systematic effects. In particular, the gain on the two power supplies controlling each quadrupole coil individually under AC operation were seen to drift over time. If their current outputs became too unequal, the AC-MOT was lost entirely – that is, the cloud positions for each "side" of the AC cycle ceased to overlap with one another. This was a significant problem in the offline setup, but the extent to which this may have contributed to our measurement of lower AC lifetimes is unclear.

4.4 Measured Lifetimes and AC Frequency

We were interested to find out whether the trap lifetime in an AC-MOT changes as a function of its (AC) frequency, and to see how lifetimes in the AC-MOT relate to the lifetimes of a comparable DC-MOT.

The results are shown in Fig. 4.9. It appears that the trap lifetimes are roughly constant as a function of frequency, provided that the AC-MOT is going faster than some minimum frequency (around 100 Hz). The precise location of the cutoff drifted over the course of data collection, as we see from the measured 1s lifetime at 100 Hz and the 4s lifetime at 50 Hz. This cutoff effect has also been observed previously, in [2], where the cutoff was observed to be around 2 kHz.

The astute reader may notice that the 500 Hz lifetimes in Fig. 4.9 appear to be inconsistent with those in Fig. 4.8 – but this does come as a surprise, as the data for the two plots was collected months apart, and any number of trapping variables may have been changed. Parameters such as overall

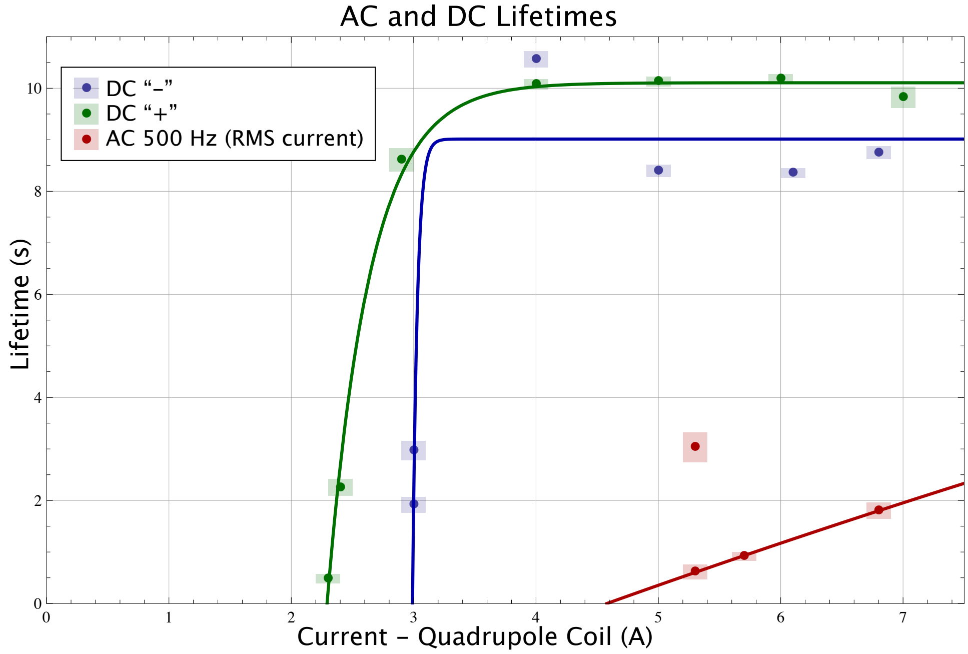

Figure 4.8: A comparison of the measured lifetimes in an AC trap and the two equivalent DC trapping states. That is, the DC "+" trap is identical to the DC "−" trap, except for the direction of current flow in the anti-Helmholtz coils, and the sign of the laser polarization. In the AC-MOT, the laser polarization flips back and forth between these two states, and the current in the anti-Helmholtz coils varies sinusoidally at 500 Hz. It can be seen from this plot that the AC-MOT lifetimes are shorter than those of a comparable DC-MOT.

laser power, fraction of power in the repumper beam, frequency tuning of either or both of these components, laser alignment, and laser polarization in either or both of the DC 'states' (both of which are needed for an AC-MOT), are all things which have been known to drift or change over longer time periods, and these can all affect the robustness of a MOT. One must also consider the systematic effects discussed in Section 4.5, which can alter trap characteristics on much shorter timescales.

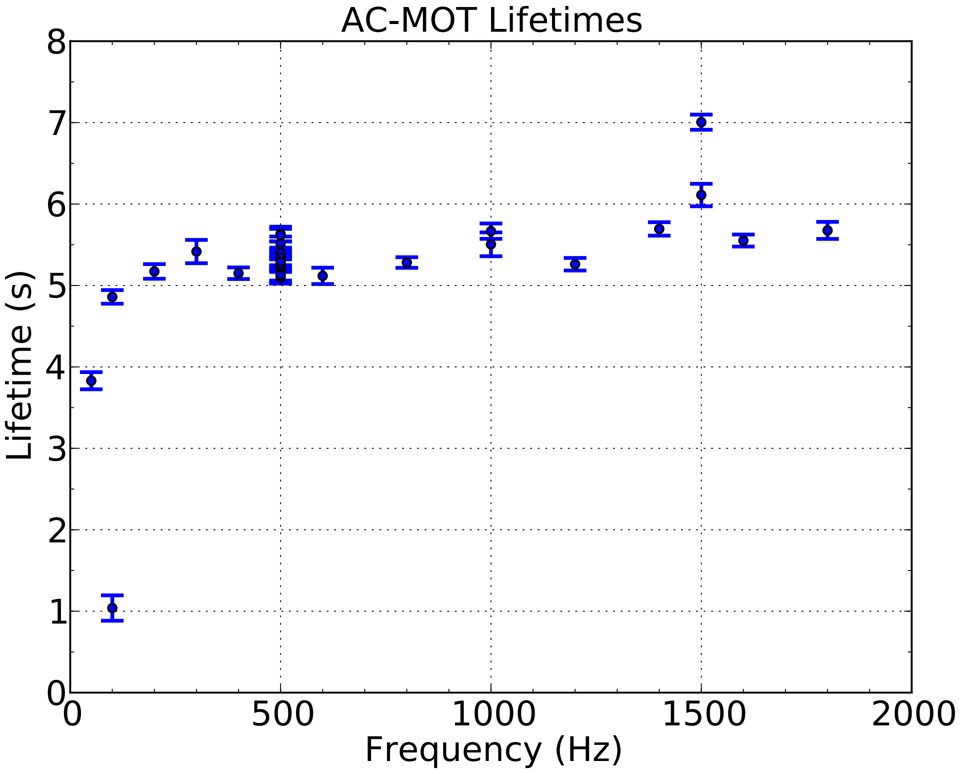

Figure 4.9: Lifetimes as a function of AC frequency. Lifetimes are measured as described in Section 4.1.2. For each datapoint, the amount of current in each coil was normalized with respect to the other coil's current through a method in which the trap position as seen by a CCD camera was required to remain constant. The peak-to-peak amplitude of the magnetic field (as measured by a Hall probe located near one side of the trap) was also held fixed at every data point. A new measurement at the 500 Hz baseline was taken between datapoints at other frequencies in order to be certain that there was no time-dependence in the results. Although the trap lifetime is nearly constant at "high enough" frequencies, there is a sharp cutoff around 50-100 Hz – though the cutoff itself appears to have changed during the measurement process. This change could be due to any of a number of systematic effects described in Section 4.5. The reason for the existence of such a cutoff is unclear, but the effect has previously been observed in [2] to occur around 2kHz.

4.5 Systematic Effects in the Offline AC-MOT

The offline AC-MOT setup was plagued by a variety of systematic problems. One noteworthy problem that had been observed in the offline MOT setup even before it was converted into an AC-MOT was the non-uniformity of the windows on the pyrex cell. This had the dual effects of damaging laser polarization, and distorting the beam profile. Thus, whenever the optical setup was ajusted or bumped and recalibrated, the laser interference patterns within the central trapping region would change as well. This could be observed qualitatively in images of the trapped cloud of atoms collected with the CCD camera–a slight recalibration of the lasers would often result in a DC trap that had moved a few millimeters or had changed its shape. Such problems are to be expected.

In the AC-MOT, however, this problem was compounded. In order to produce a functional AC-MOT, it is necessary for the cloud's location in one DC-MOT state must be the same as (or at least overlapping with) the cloud's location in the other DC state. If this cannot be achieved, the AC-MOT will fail – and to the extent that is achieved only poorly, the characteristics of the AC-MOT will be non-optimal. The atomic cloud may be spread out, and atoms may be ejected from the trapping region, damaging the AC-MOT's ability to retain atoms. This problem of was largely corrected in the online AC-MOT setup, where lasers entered the chamber only through viewports specifically designed to be flat, and mounted on a much more solid stainless steel chamber.

An additional source of instability specific to the offline AC-MOT was the power supplies controlling the current through the anti-Helmholtz coils. In the offline MOT, it was necessary to use a different set of power supplies to control the AC-MOT than we had used for DC control. Although the power supplies used for DC operation of the MOT were quite stable, they were not able to produce an alternating current. For running the anti-Helmholtz coils in AC mode we used a pair of Peavey CS 4080Hz audio amplifiers, which were unable to produce a DC current. It is worth noting here that it was necessary to use two amplifiers – one for each current-carrying coil – because a single amplifier would have been unable to drive the necessary current through both coils. Though I am unable to comment on the quality of this hardware when used for its intended purpose, it turned out to be quite problematic for use in an AC-MOT.

As is typical for audio amplifiers, these devices were not able to output a tunable DC offset to their current. In principle, they were expected to produce symmetric positive and negative voltage outputs, automatically adjusting their average DC offsets to zero. In practice, oscilloscope readouts suggested that the DC offsets output from these devices drifted over time. The gain on these amplifiers drifted over time as well – perhaps as a result of them heating with use, though the drift on these two audio amplifiers was asynchronous. Since it was necessary to run these amplifiers at close to their full power, it was common for the gain on one or both amplifiers to drift upward just enough for the output waveform to be clipped on one side.

Therefore, it was necessary to closely monitor current output from the audio amplifiers while trapping. Though nothing could be done about DC offsets, their respective gains could be adjusted manually, and this sometimes had an effect on the DC offset.

Problems with the audio amplifiers dominated systematic effects in the offline AC-MOT. Instability in the anti-Helmholtz coil currents produced instability in the atoms' effective (Zeeman shift) potential well. Since an AC-MOT requires that the potential minima for both 'states' must be in the same spatial location, the offline AC-MOT proved to be very finicky. Lifetime measurements and trap size measurements were very different from day to day, and somewhat different from hour to hour.

Fortunately, this latter problem was mostly eliminated in the online AC-MOT. The solution was simply to buy a more expensive set of power supplies designed to do what we wanted. The online setup used two Matsusada DOP 25-80 power supplies, which are capable of outputting both DC and AC currents and voltages, and which also had extremely minimal drift. As a result, the online AC-MOT proved to be significantly more stable than the offline AC-MOT.

Chapter 5

Turning the Trap Off

The reader will recall that the goal of this work is to obtain samples of cold, tightly confined, spin-polarized atoms for further study. To polarize a sample of atoms well, the magnetic field gradient must be zero (or as close as is achievable), and an incident optical pumping laser must be as completely polarized as possible, and tuned precisely to the proper atomic resonance. Unfortunately, these requirements (as well as the fact that the lasers used for confining atoms within a MOT would destroy any atomic polarization) mean that atomic polarization cannot be obtained during the normal operation of a MOT. The trapping lasers must be shut off and the magnetic field gradient must be eliminated before successful optical pumping can occur.

To this end, we employ a strategy of running the AC-MOT over several AC 'cycles', then halting the trapping mechanism for a period of time to allow for optical pumping. The MOT forces resume again – ideally before too many atoms have been lost from the trapping region – and the atom cloud is compressed once more during operation of the AC-MOT, until the trapping forces are halted again. We will henceforth refer to this on/off cycling – and more specifically to the fraction of the total time spent with the AC-MOT off – as the 'duty cycle'.

We wish to allow as much time as possible for optical pumping, while simultaneously retaining as many atoms as possible. The residual magnetic field during the optical pumping window is an additional consideration, and its optimization was the reason behind our choice to develop an AC-MOT. It is, of course, necessary to use an integer number of AC cycles between optical pumping times so as to allow us to shut off the current in the quadrupole coils at a moment when the residual eddy currents in the suriounding materials are zero [2]. In this way, the magnetic field gradient is minimized so as to allow for optical pumping.

The problem of optimizing laser polarization for optical pumping is addressed by former co-op student Scott Smale in his end of term report [8]. Here, it suffices to say that in the online trap, the optical pumping laser setup was entirely separate from the one that was used for trapping in the MOT, and optical pumping was never implemented at all in the offline trap.

5.1 Methods for Turning Off the Trap

The trapping mechanism in a MOT can be stopped by shutting off either the magnetic field or the trapping laser. It is helpful to determine which mechanism for removing trapping forces produces the best trap lifetimes and smallest cloud sizes, as averaged over many on/off cycles during which the cloud of atoms is retained.

The data used to generate Figs. 5.1, 5.2, and 5.3 was taken in the offline MOT. We ran a continuous loop of 3 AC cycles at 1000 Hz, followed by 1 "off" cycle – 3 ms on followed by 1 ms off. We also took a series of data in which the trapping mechanism was not stopped, in order to make a useful comparison.

We are interested in understanding what happens to the cloud of trapped atoms when we turn the trap off. It is possible to halt the trapping mechanism by turning off the magnetic field gradient, the laser, or both. We examine the differing effects of each of these techniques, and the results are shown in Figs. 5.1, 5.2, and 5.3.

As one might expect, increasing the laser power increases trap fluorescence, but it also heats the atoms, thereby decreasing trap lifetime. We find that it is possible to preserve the trap lifetime, despite removing trapping forces during some fraction of the time, as long as the trapping light is removed. While the magnetic field is being turned off, it is non-zero and poorly quantified for some length of time. Furthermore, since we attempt to eliminate the magnetic field as rapidly as possible, it is entirely reasonable to suppose that we may overcorrect the current, and thus the sign of the magnetic field gradient would be briefly opposite of our expectation. If at any point the sign of the magnetic field is reversed, the atoms that had previously been trapped could be ejected upon interacting with the laser. We did not examine the presence of this mechanism beyond what is shown in this section.

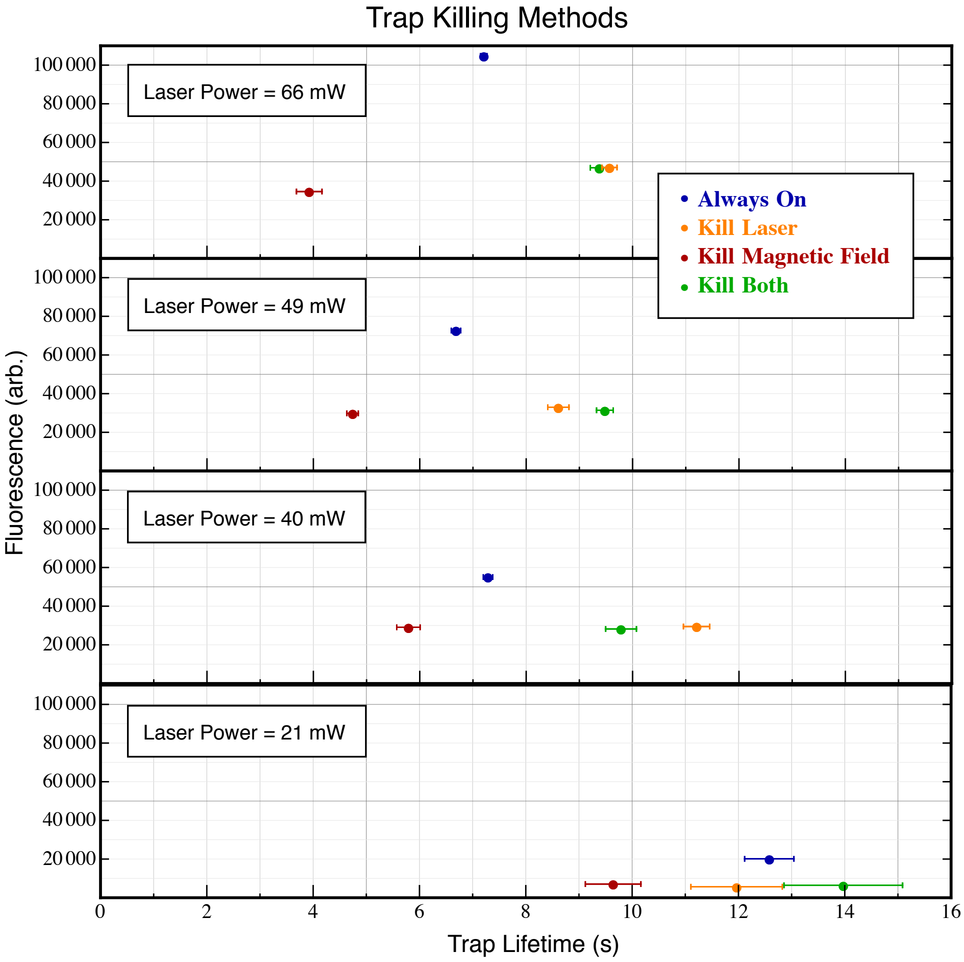

Figure 5.1: Different methods for eliminating the trapping mechanism and destroying the cloud of atoms were tested at several different levels of laser power in the offline AC-MOT at $f_{\mathrm{AC}} = 1000$ Hz. The goal was to remove the trapping mechanism for some part of the duty cycle while still maintaining a long average lifetime and a high number of trapped atoms. Trap fluorescence is treated as a stand-in for the number of atoms in the trap, and is measured as in Section 4.1.1. Except for the points labelled as ‘always on’, the MOT is run with a duty cycle in which the trapping forces are on for 3 ms, then off for 1 ms.

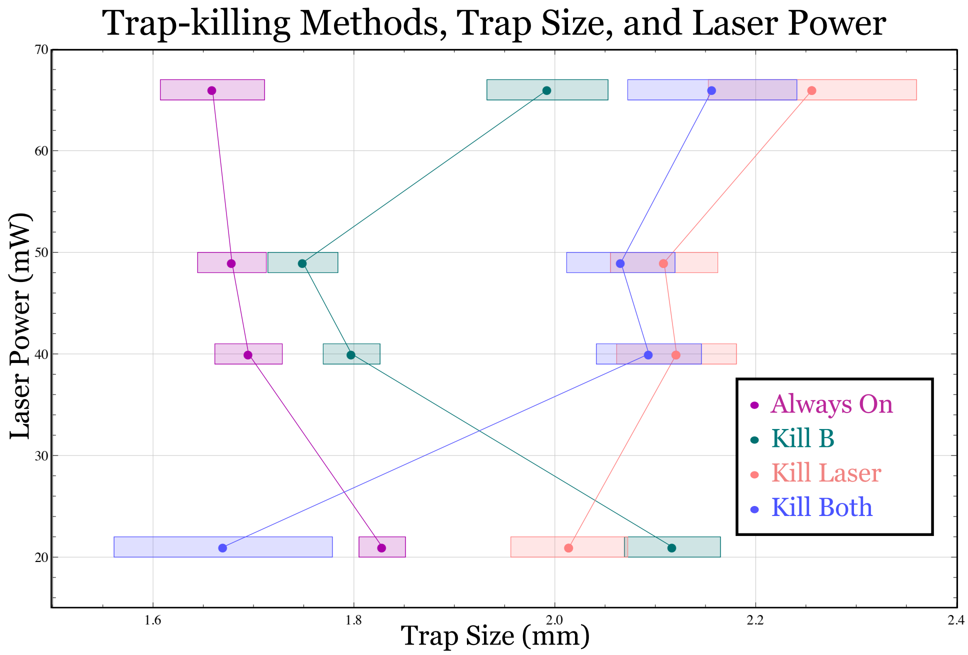

Figure 5.2: Different methods to eliminate the trapping mechanism, and their effects on trap size, are shown for several different laser power measurements. The AC-MOT is run at a frequency of $f_{\mathrm{AC}} = 1000$ Hz, and except for the points labelled as 'always on', the MOT is run with a duty cycle in which the trapping forces are on for 3 ms, then off for 1 ms. Laser power is measured immediately after the EOM shown in Fig. 4.6. Trap size is averaged over many on/off cycles, and is measured as described in Section 4.1.3. This data seems to suggest that whether or not the magnetic field is shut off, the trap diameter is larger if the laser is shut off. This is consistent with what we might have guessed based on the premise that the optical molasses from trapping lasers would create a drag force to slow expansion of the atom cloud once the MOT's confining force is shut off.

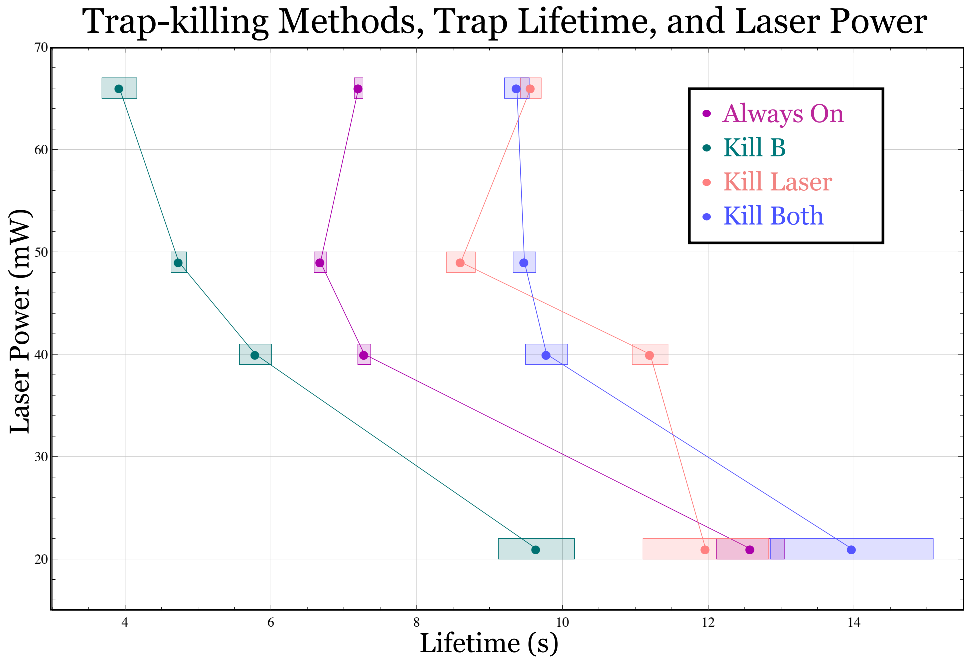

Figure 5.3: The AC-MOT is run at a frequency of $f_{\mathrm{AC}} = 1000$ Hz, and except for the points labelled as 'always on', the MOT is run with a duty cycle in which the trapping forces are on for 3 ms, then off for 1 ms. Laser power is measured immediately after the EOM shown in Fig. 4.6, and trap lifetime is measured as in Section 4.1.2, and is averaged over many on/off cycles. For this plot, trapping forces are removed from an AC-MOT operating with several different values of laser power (plotted on the vertical axis). The effect on (average) trap lifetime is shown. Whether the magnetic field is turned off or not, the lifetimes are longer when the laser is shut off. It is interesting to note that that the trap lifetimes measured in the case where the trapping mechanism is always on are shorter than the trap lifetimes measured when the laser (and therefore the trapping mechanism) is shut off for part of the duty cycle. The mechanism behind this effect is unclear.

5.2 Duty Cycle

It is important to maximize the percentage of time during which the magnetic field (which is itself needed in order to maintain the trap) is off, while simultaneously keeping the observed trap lifetime as long as possible (as averaged over many trapping/non-trapping cycles), because we are only able to collect useful data during the time when the magnetic field is off and the atoms are polarized. The eventual goal is optimize count-limited beta-decay statistics using (radioactive) ^{37}K as our trapped isotope. To this end, we examine different methods for destroying the trapping forces, and achievable duty cycles in an AC-MOT trapping ^{41}K, which has a hyperfine structure similar to that of ^{37}K.

Initial results describing the effect of different duty cycles on average trap lifetime and fluorescence are shown in Figs. 5.4 and 5.5. Both show data collected in the offline pyrex chamber using ^{41}K. It is worth noting that the most obvious way to improve on these results would be to use a set of laser beams which is more optimally balanced and more gaussian in profile. However, in the offline vapor cell we were limited by the quality of the chamber windows through which the laser passed. In particular, an anti-reflective coating on the windows would have likely produced a large improvement in beam profile and balance. This was later achieved in the online chamber, however no comparable data has been collected in that geometry.

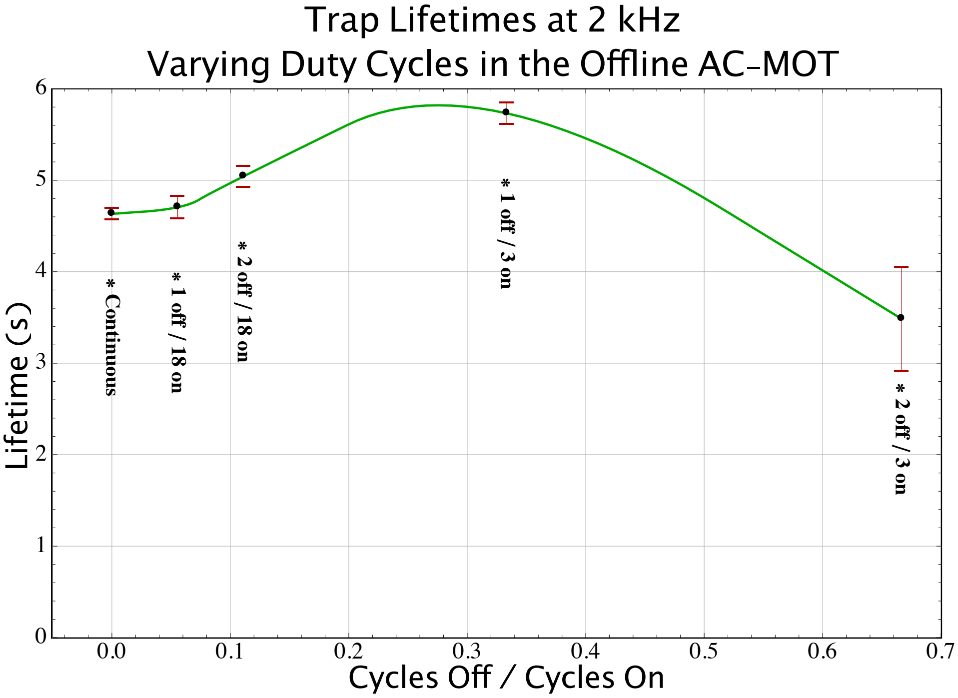

Figure 5.4: Initial results describing the effect of varying the duty cycle on the (time-averaged) trap lifetime, at $f_{\mathrm{AC}} = 2$ kHz. Trapping forces are removed by eliminating both the magnetic field and the trapping laser. Lifetime measurements are taken as per the procedure described in Section 4.1.2, with the additional caveat that lifetime measurements are averaged over multiple on/off cycles. The green curve is intended only to guide the eye. One can see that turning the trapping forces off for a sufficiently small fraction of the time does not harm trap lifetime measurements; counterintuitively, the trap lifetime may even increase slightly in some cases. This observation is consistent with the data presented in Fig. 5.3.

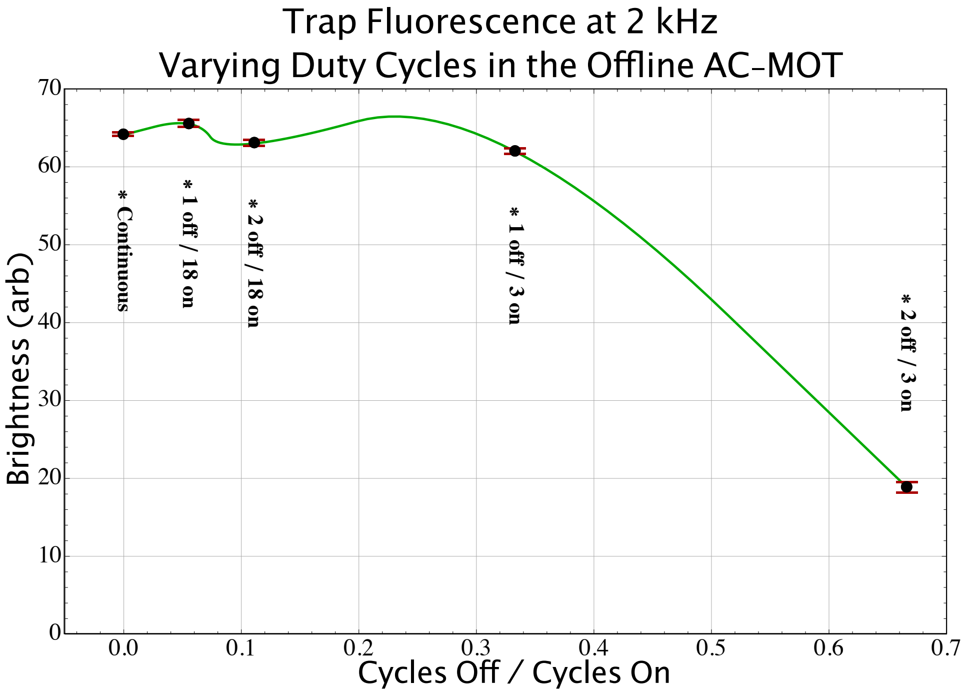

Figure 5.5: Trap fluorescence measured as a function of the trapping duty cycle at $f_{\mathrm{AC}} = 2$ kHz. Trapping forces are removed by eliminating both the magnetic field and the trapping laser. Brightness measurements are taken as per the procedure described in Section 4.1.1, with the additional caveat that fluorescence measurements are averaged over multiple on/off cycles. The green curve is intended only to guide the eye. Since the laser is shut off during the "off" cycles, one might expect that in the absence of atom loss, fluorescence should be proportional to the fraction of total time used for the AC-MOT, but this does not appear to be the case. Instead, we see that the brightness is roughly constant provided that the duty cycle includes a sufficient percentage of time with the AC-MOT on.

5.3 Residual Magnetic Field in a Pyrex Cell

One of the things we attempted to optimize is the residual magnetic field in the magneto-optical trap. In particular, our goal was to eliminate the magnetic field in the trapping region as completely and as quickly as possible after turning off the trapping mechanism. As a first test, we worked with our offline AC-MOT, where we measured the residual magnetic field using a Hall probe located outside the chamber. Typical results are shown in Figs. 5.6 and 5.7.

Our methodology suffered from a variety of systematic effects. With the Hall probe located outside the chamber, far from the region in which the field gradient could be expected to be linear, we treated the measured value of the magnetic field as being directly proportional to the size of the field gradient within the central trapping region. Given our knowledge of the system's geometry, we were able to estimate the proportionality constant, but this was made more difficult by the fact that the Hall probe's mount was not stable. Both the position and orientation of the probe would change between datasets, and the result was a noticeable change in measured magnetic field strength.

Because of the amplifiers available to us, we controlled the current through the anti-Helmholtz coils indirectly, through their voltages. In the offline traps, a variety of audio amplifiers were used to drive the rapidly oscillating AC voltages we needed. Two audio amplifiers were used at any given time – one to drive each coil – because an individual audio amplifier could not produce sufficient current to drive both coils at once. This technique produced several systematic effects. The amplifiers' gains drifted by approximately 10% over the course of a couple hours' worth of measurements. Additionally, the frequency dependence of the gain was different between any set of two amplifiers. Unfortunately, when the currents through the two coils became too unequal, the trap was destroyed.

The amplifiers were controlled in the voltage domain by means of an arbitrary waveform. These waveforms were generated by computer to a format which was compatible with the Stanford Research Systems DS435 function generators, to which the waveforms were uploaded. The function generators were then used to control the audio amplifiers directly.

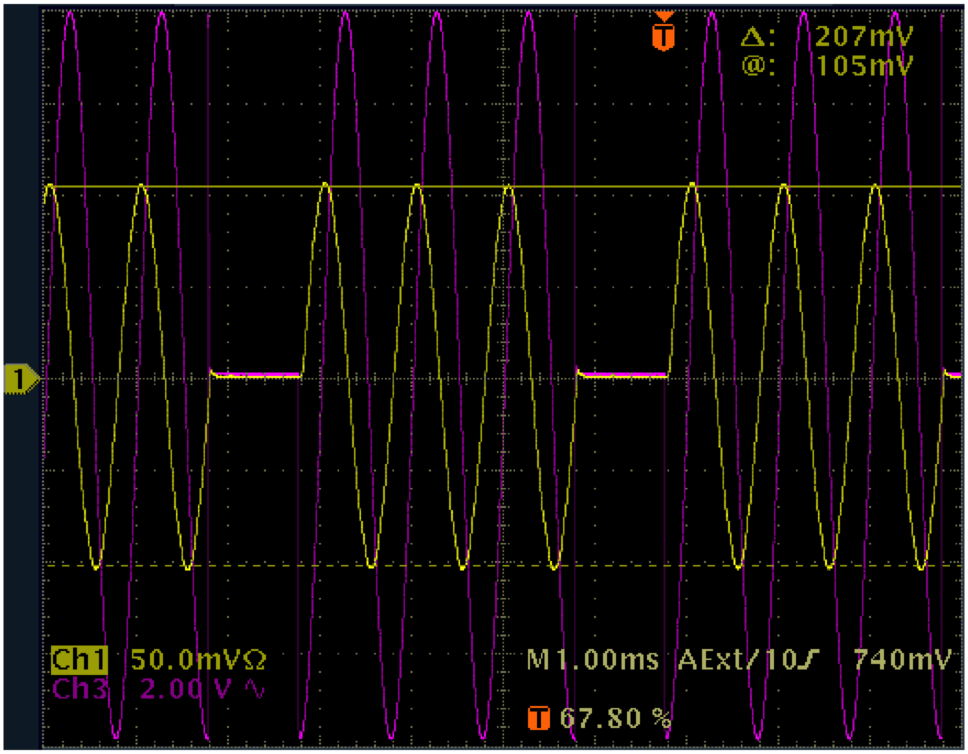

Figure 5.6: Optimal Waveform to Minimize Residual Magnetic Field in the Offline Trap. Channel-1 shows the readout of the Bell Labs Hall probe, while Channel-3 shows the output of an SRS-DS345 function generator as it is being used to control (one of) the anti-Helmholtz coils. On Channel-1, 1 mV is equivalent to 1μT at the probe's location. The peak-to-peak amplitude of the magnetic field is approximately 2.2 mT.

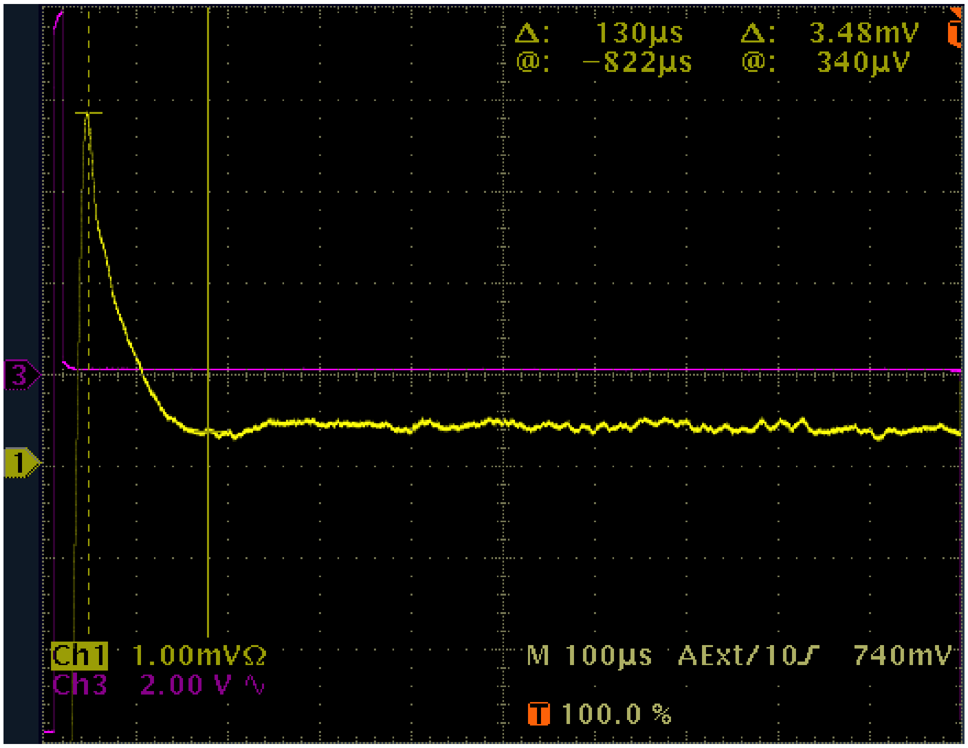

Figure 5.7: This is a zoomed in view of the same output as is shown in Fig. 5.6. At the time of the initial drop in magnetic field, the residual magnetic field (Channel-1) is 3.2% of its maximum value, and decays rapidly away. Note that this Hall probe's overall offset drifts by approximately 1mV.

Chapter 6

Calibrations of the Online Trap

In addition to our offline setup, measurements and calibrations were also done on a new "online" MOT chamber setup. The online trapping setup differs from the offline setup in that the online setup includes two distinct magneto-optical traps, separated by approximately two metres. The first is used for initial collection of a sample of atoms, either from the beamline itself in the case of radioactive atoms, or else from a dispenser to be used for offline tests. The trapped atoms in the first MOT are then periodically loaded into the second MOT according to the methodology described in [9]. This is done so as to minimize the background from decaying untrapped radioactives near the second trapping chamber where our detection apparatus is located. The first trap is only intended to be run as a DC-MOT.

The second trapping chamber was newly constructed from 316-L stainless steel, which has very low electrical and thermal conductivity as compared with other metals. This material was selected because while it was necessary for our chamber to be sturdy enough to mount a series of deterctors, it was also desirable to minimize electrical eddy currents resulting from the AC-MOT in this chamber.

Around this time, we also acquired a new model of Hall probe, and two new, more reliable amplifiers to drive the anti-Helmholtz coils in the second trap. Additionally, in the time before the chamber was closed up for trapping, it was possible to mount the Hall probes reliably at known positions relative to the centre of the trapping region. This allowed for a much more accurate estimate of the effects of eddy currents at the trap centre than had been possible in the offline setup.

The power supplies for the online trap are both Matsusada DOP 25-80, which are designed to run in the range of ±25V and ±80A. These were an upgrade from the offline MOT's audio amplifiers, not only because of their greatly decreased propensity for drifting, but also because these power supplies allowed for rapid switching between an AC signal and a DC voltage or current.

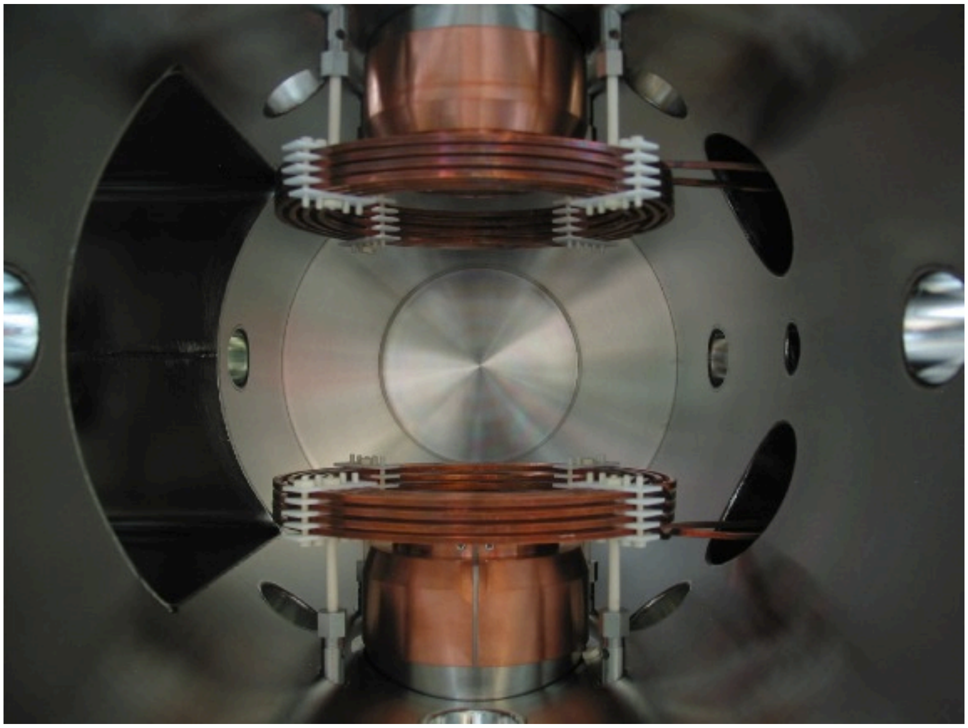

Figure 6.1: A photo of the inside of the new trapping chamber, before most of the hardware for observing β-decay daughter particles was installed. The two current-carrying copper quadrupole coils are clearly visible. The chamber walls are made of 316-L stainless steel, a material which was selected as a compromise between strength, cost, and minimizing eddy currents in the chamber walls.

This ability for the second MOT to switch between AC and DC modes of operation rapidly and without destroying the cloud of trapped atoms was essential for two reasons, the first being the method by which the second trap acquires its atoms. The atoms are loaded directly from the first MOT, which transfers its atoms over to the new chamber at intervals of approximately one second according to the method described in [9]. The atoms are transferred by using a resonantly tuned laser to "push" the atoms over from their initial position in the first MOT, through two optical funnels, and into the new chamber where they are re-collected in the second DC-MOT, which already holds any atoms remaining from previous transfers which have not yet been lost. The optical funnels are each comprised of two sets of current-carrying

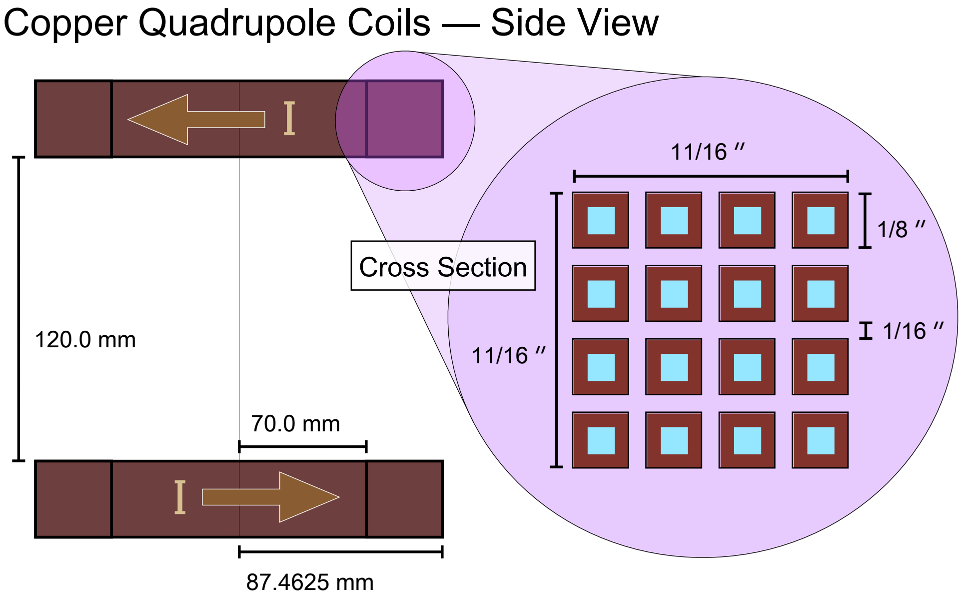

Figure 6.2: Geometry of the quadrupole coils in the online MOT is shown here. Water flows through the coils to cool them. These coils can be driven in AC mode with a DC offset, so they serve a second purpose as trim coils, cancelling out one component of the ambient magnetic field within the lab (generated by the nearby cyclotron when it is in operation, and by the earth itself). There are two additional sets of trim coils (not shown) which are external to the chamber, and tuned with a DC offset so as to cancel the magnetic field components in the other two dimensions.

coils–effectively a two-dimensional MOT–in order to keep the atoms confined in the transverse directions during the transfer. Once the atoms have been collected in the second MOT, they must not be lost as we switch its operation from a DC-MOT to an AC-MOT.

The author of this thesis speculates that it may be possible to adapt this technique to collect atoms in an AC-MOT directly. However, the atoms' times-of-flight are expected to be in the 10s of milliseconds, so a relatively small spread in transfer speed would cause arrival times to vary, spanning several AC cycles. It seems likely therefore that transferring atoms directly into an AC-MOT would result in a less robust and less efficient transfer mechanism. We did not attempt this.

The second reason for the importance of our ability to switch between AC and DC operation is that our goals for data collection require a small cloud of *polarized* atoms. We polarize the atoms by optically pumping them after the MOT has been turned off, but this is ineffective in the presence of non-uniform and non-static magnetic fields. In order for optical pumping to be effective, it is necessary that any present magnetic field must be uniform and aligned along a previously chosen axis of laser propagation. Any misalignment of the magnetic field axis with the optical pumping axis will prevent the atoms from being fully polarized. Similarly, a magnetic field which is non-uniform over the extent of the atomic cloud must produce non-uniform atomic polarization when an optical pumping laser is applied. Though we might be tempted to simply apply a large dipole field on top of any residual quadrupole field from the MOT so as to maximally align the two axes, this is inadvisable. The presence of a large magnetic field will cause energy splitting between nearby hyperfine levels, which will harm optical pumping efficiency as the laser becomes more detuned from only some of the transitions to which it was intended to couple. A large magnetic field would also cause mixing between the states we had hoped to optically pump, again damaging our ability to polarize the sample of atoms.

Thus, the best solution is to eliminate the quadrupole field used in the MOT as rapidly as possible, while simultaneously applying a small constant dipole field on top of any residual non-uniformities. To rapidly eliminate the quadrupole field from the MOT, we use an AC-MOT. However, the small dipole field is produced by generating a small DC current in the same coils that had been producing the quadrupole field, so the necessity of switching between AC and DC operation rapidly is clear.

6.1 Frequency Response in the Online Setup

The first task was to calibrate the power supplies' output in the relevant setup. With this information, we can monitor the current output either through the "current output monitor" port in the power supply, or if we are running the power supplies in current-control mode, indirectly through the amplitude of the input signal.

We first note that the power supplies' specifications are such that they can accept input voltages within the range [-10V, 10V], which is used to control an output signal in the range [-80A, 80A], and [-25V, 25V]. They are also equipped with 'voltage monitor' and 'current monitor' ports, both of which output a voltage signal in the range [-10V, 10V], to monitor the voltage and current outputs, respectively. Therefore we write,

$$\begin{aligned} I_{\text{out}}[\text{A}] &= \frac{80\text{A}}{10\text{V}}\, I_{\text{mon}}[\text{V}] && (6.1)\\ V_{\text{out}} &= \frac{25\text{V}}{10\text{V}}\, V_{\text{mon}} \\ &= \frac{25\text{V}}{10\text{V}}\, V_{\text{in}} && (6.2) \end{aligned}$$

It is useful to measure the effective inductance of the two coils when they are both running in their trapping (anti-Helmholtz) configuration. Because of the limit to the amount of voltage we are able to output to the coils, it is necessary to know their effective inductance in order to determine how high an AC frequency we can run our MOT at, if we require some minimum of current output. We determined both the resistive and capacitive components of the impedance of the system to be negligible, and drove the power supplies with a continuous sinusoid of amplitude $V_{\text{in}} = 9.8\text{V}$, at several different frequencies. Recall that under harmonic excitation, a system with a purely inductive load can be described by

$$\frac{I_{\max}}{V_{\max}} = \frac{1}{2\pi f L}. \qquad (6.3)$$

The data was therefore fit to

$$\frac{I_{\text{mon,max}}[\text{V}]}{V_{\text{in,max}}[\text{V}]} = \left(\frac{25\text{V}}{80\text{A}}\right)\frac{1}{2\pi f L}, \qquad (6.4)$$

and is shown in Fig. 6.3. The result was an effective inductance of (50.1 ± 0.2) μH.

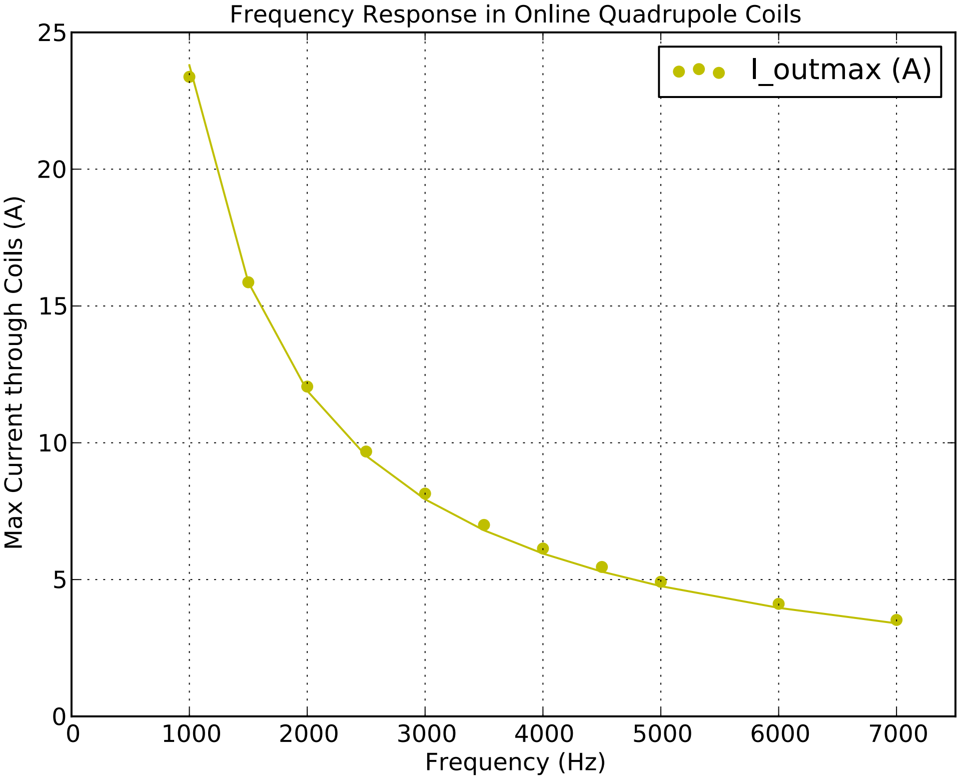

Figure 6.3: Inductance in the online MOT setup. The coils were both driven in voltage-control mode with a continuous sinusoidal input of amplitude 9.8V. Best fit gives $L = (50.1 \pm 0.2)\,\mu\mathrm{H}$, which is reasonably close to the value of $48\,\mu\mathrm{H}$ that was obtained by direct calculation in a simplified geometry. The coils were driven 180° out of phase with one another (as they would be during trapping) so as to account for mutual inductance effects.

This result is quite close to the value of $48\,\mu\mathrm{H}$ which can be calculated by use of the Biot-Savart law (ie, assuming that changes to the current are "slow") in a simplified geometry – 2 sets of circular coils of 16 turns each, with a radius of 78.7 mm, separated by a distance of 137.5 mm.

6.2 Frequency Response in the Hall Probes

We are interested in the size of the magnetic field gradient produced by an AC-MOT at varying frequencies. It is helpful to know the inductance of the system, but it is also possible that the Hall probes themselves may suffer from frequency-dependent systematic effects. We expect magnetic field to be directly proportional to the current in the coils, so any deviation from that would indicate either some frequency dependence in the Hall probes' response, or (less likely) some frequency dependence in the accuracy of the power supplies' current monitor output.

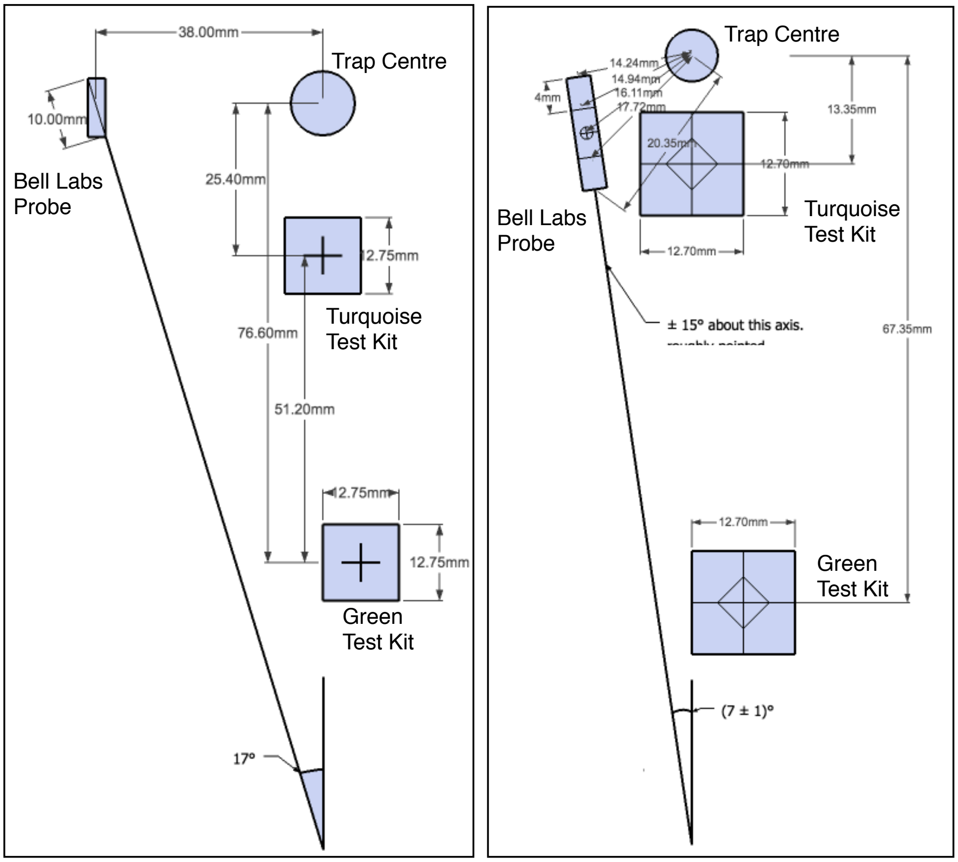

Hall Probes: First Layout

Hall Probes: Second Layout

Figure 6.4: Hall probe configurations used in the "online" trapping chamber. Angular tolerances on the axes of the Hall probes are all ±15°, except where otherwise specified. "out of page dimension" tolerances are ±6 mm. The Bell Labs probe is constrained to measure only the $\hat{z}$ component of the magnetic field (that is, out of the page), while the Ametes Test Kit probes measure the radial component of the field–to within given tolerances–unless otherwise specified.

In order to quantify this effect, we set up all three of the Hall probes as shown in the first configuration of Fig. 6.4, and drove the coils with a series of pure sinusoids at different frequencies, while holding the amplitude of the current output fixed. The result is shown in Fig. 6.5. Note that while some frequency dependence clearly does exist, it is reasonably small within the frequency range in which we are interested.

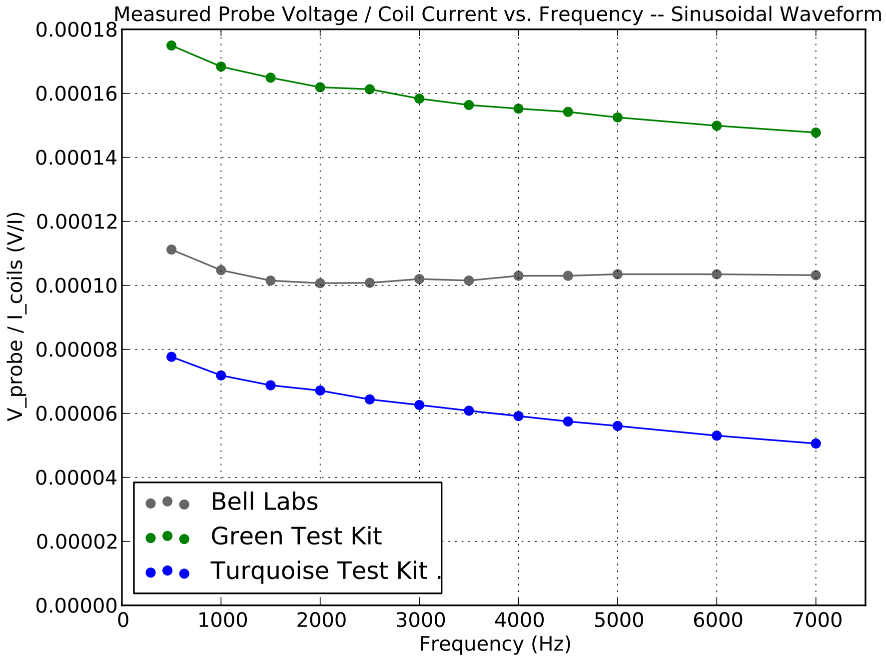

Figure 6.5: The ratio between the measured amplitude of the magnetic field and the measured amplitude of the coil current, as seen by three different Hall probes configured as on the left side of Fig. 6.4, as a function of frequency. Ideally, these lines would each be completely flat, indicating no frequency dependence in the Hall probes' outputs, however the dependence seen is not a major concern if we only consider our region of interest for the AC-MOT ($\sim$ 500 - 2000 Hz).

6.3 Acoustic Resonances

Because mechanical stability is important to any precision apparatus, we hoped to choose a trap frequency for the AC-MOT that would excite few mechanical resonances. In particular, mechanical vibrations in our current-carrying coils (located inside the vacuum chamber) have the potential to damage or shake loose the ceramic feedthroughs which maintain the vacuum seal between the inside of the trapping chamber and the outside world (see Fig. 6.6). The chamber must be maintained at ultra-high vacuum during any science run, so the prospect of loosening the ceramic feedthroughs with persistent acoustic vibrations was a very real concern.

We can see from Fig. 4.9 that below some cutoff, the trap frequency does not have a particularly large effect on trap lifetime, so we were largely free to select a trap frequency based on this secondary criterion – minimizing mechanical resonances.

In the new chamber, we chose to run the AC-MOT at a frequency of $f_{\mathrm{AC}} = 1/(9.824 \times 10^{-4} s) \approx 1017.9$ Hz. This is near a minimum of acoustic noise, as determined by Fig. 6.7. One possible systematic problem with this set of measurements is that they were all collected while the second half large flange on the chamber was absent. The simple presence of this flange would change the geometry whose resonance we are interested in, and eliminating the atmosphere within the chamber (as during operation of the MOT) would remove one source of the resonances observed.

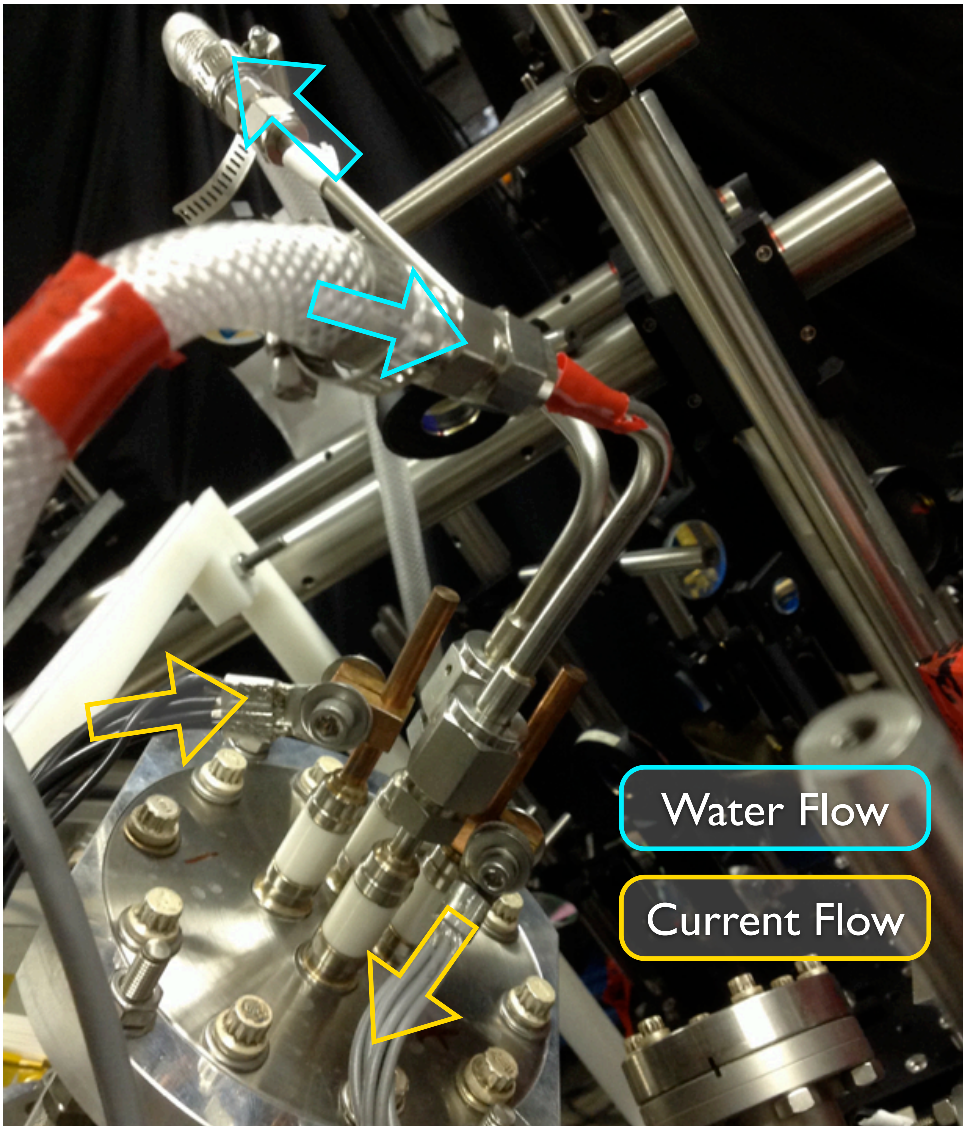

Figure 6.6: Ceramic feedthroughs to the top coil. The current-carrying quadrupole coils must be kept electrically isolated from the stainless steel chamber as they are fed voltages from the outside. These coils are kept cool inside the vacuum chamber by pumping water through them as they run. Each of these connections between the inside and outside of the vacuum chamber uses such a feedthrough. There are eight of these in total, and they are relatively brittle; they could be broken by repeated stresses between the quadrupole coils and the ceramic, such as may result from the varying forces of an AC-MOT.

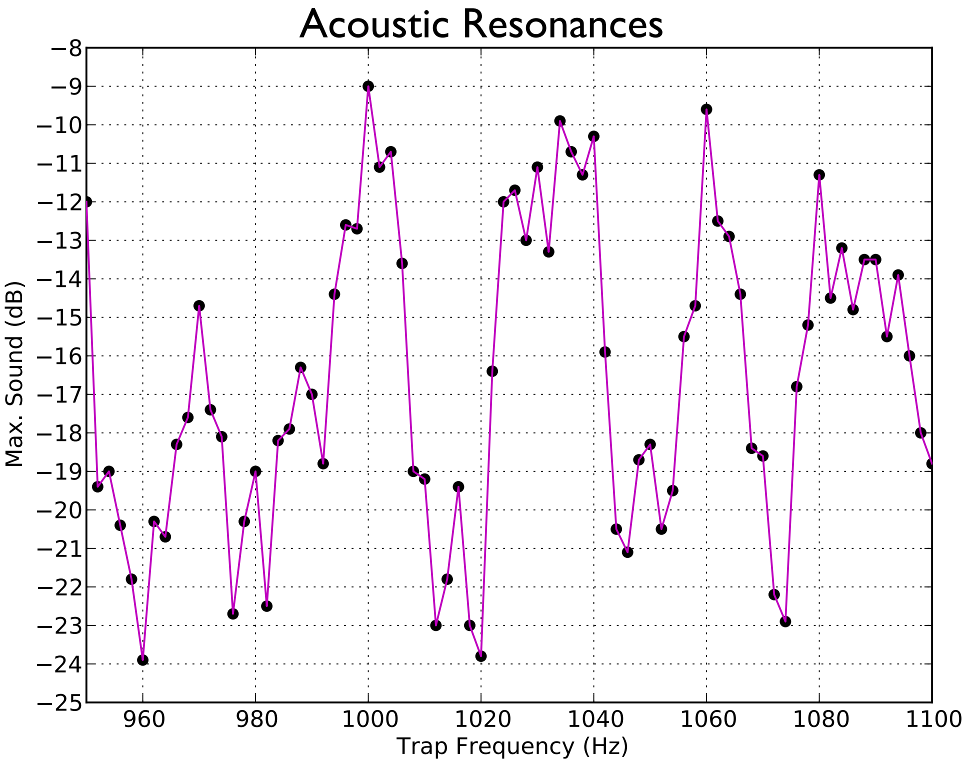

Figure 6.7: Acoustic resonances in the online chamber. This data was taken by driving the AC-MOT magnetic field coils with a continuous sinusoidal waveform at a series of frequencies, as shown on the horizontal axis, and using a nearby microphone connected to a computer with signal processing software to measure the overall amplitude of the resulting acoustic noise. Note that this data is likely sampled at a rate higher than the processing software's built-in Nyquist limit. Datapoints are taken at 2 Hz intervals, while the Nyquist limit was "probably" 5 Hz. (The software's documentation claimed a limit 5 Hz, however the program also included a bug in which the measured frequencies were reported as being twice their true value. Although the software's frequency spectrum analysis capabilities were not used explicitly, these limitations may still be relevant in determining the Nyquist limit to the resolution of any frequency-spectrum plots that resulted from any use of the software.) This oversampling gives the illusion of presenting more information than is actually available, and would have the effect of visually broadening the appearance of fine resonances on the plot. We eventually chose to run the trap at a frequency of $f_{\mathrm{AC}} = 1/(9.824 \times 10^{-4}s) \approx 1017.9$ Hz., near a local minimum of acoustic noise.

6.4 Control of Online Power Supplies

The newly purchased Matsusada DOP 25-80 power supplies' specifications allow for them to be controlled by an input signal in either "voltage-control" or "current-control" mode. That is, the power supplies accept an input voltage signal in the range ±10V, and translate this linearly, either directly into an output voltage (in the range ±25V), or into an output current (in the range ±80A).

Although we had initially intended to run the power supplies in current-control mode so as to have more direct control over the shape of the magnetic field, it became immediately obvious upon setup that this would not produce the desired results. We found that when controlled by a typical waveform in current-control mode, the output current contained large artifacts, the shape of which was strongly dependent not only on the frequency of the (AC) waveform and the lengths of time spent on (with a large AC signal) and off (with either zero current or a small DC current) within each waveform, but also on the overall amplitude of the current output as well. This would have been extremely challenging to work with had we continued with our original plan – however the power supplies functioned much as could have been expected when used in voltage-control mode, with no such artifacts present in the output. Therefore, the power supplies were always run in voltage-control mode, and the generated input waveforms were all created specifically to be used in this mode of operation.

The waveforms used for controlling the Matusada DOP 25-80 power supplies are themselves produced by two SRS DS345 function generators (one for each coil). The waveform shapes are created by running a Python script (see Appendix A) and output in a format to match the SRS DS345 specifications, then uploaded to the function generators.

6.4.1 Determining the Number of Points for an Arbitrary Waveform

The first thing to determine about any arbitrary waveform is the number of points comprising it (`N_points`) – a matter which turns out to be less trivial than one might have imagined. An arbitrary waveform may contain up to 16,300 points, and the function generator can sample those points at rates of

$$\texttt{samplerate = } 4.0 \times 10^7 \texttt{/ N\_sample} \text{ (points/second).} \tag{6.5}$$

where `N_sample` is an integer chosen by us. The function generator extrapolates its output voltage linearly between any set of two adjacent points in an arbitrary waveform.

It is clearly advantageous for the purpose of precise control to use a waveform with as many points as possible, so as to be able to sample points as rapidly as possible. We also would like for each individual sinusoidal period to utilize the same number of points (`points_per_cycle`), so that the exact results of shutting off the AC-MOT are reproducible independently of the number of AC cycles in the arbitrary waveform. We therefore require the waveform to obey the expression

$$\texttt{N\_points = N\_cycles * points\_per\_cycle} \tag{6.6}$$

$$\texttt{N\_points} \leq 16300 \tag{6.7}$$

This also constrains the values of AC frequency (`f_AC`) we may use. In particular,

$$\begin{aligned} \texttt{f\_AC} &= \frac{\texttt{samplerate}}{\texttt{points\_per\_cycle}} \qquad (6.8) \\ &= \left(4.0 \times 10^{7}\ \text{Hz}\right) \frac{\texttt{N\_cycles}}{\texttt{N\_sample * N\_points}} \qquad (6.9) \end{aligned}$$

where we hope to keep `f_AC` near some desired value while simultaneously maximizing `N_points` and minimizing `N_sample`. `N_cycles` is determined by the desired duty cycle of the AC-MOT, such that

$$\texttt{N\_cycles = cycles\_on + cycles\_off.} \tag{6.10}$$

Note that while `cycles_on` is required to have an integer value in order for the AC-MOT to function properly, there is no similar *a priori* requirement on `cycles_off`. In fact, for any given `f_AC`, we are able to adjust the value of `cycles_off` while simultaneously changing `N_points`, provided only that (`N_cycles / N_points`) remain fixed at a value that works. `N_sample` should not be adjusted without undergoing a major overhaul, as the sample rate is relevant to the shape of the "fast" features near the start and end of the waveform – features which use a small number of points, but which are critical to properly controlling the magnetic field.

6.4.2 Adjusting Waveform Parameters

In addition to the AC-frequency of a waveform, there were four parameters of the waveform which were varied in order to produce the most optimal magnetic field for use in the AC-MOT. `phi_start` and `phi_end` controlled the phase angle at which the sinusoidal waveform begins and ends, respectively.

The need for these parameters is consistent with the description of an AC-MOT given in [2]. Additionally, `t_startdelta` and `t_enddelta` control the length of time allocated to a maximum-amplitude voltage spike at the beginning and end of the sinusoidal component of the waveform, respectively. These were needed to overcome limitations specific to our power supplies.

Since `t_startdelta` produced a voltage spike in the same direction as the beginning of the sinusoid itself, its effect on the magnetic field was similar to starting the sinusoid up with a decreased starting phase `phi_start` The primary effects of both of these two parameters were on the shape of the sinusoidal part of the current output, rather than on the residual magnetic field after the driving sinusoidal voltage was removed (see Fig. 6.8).

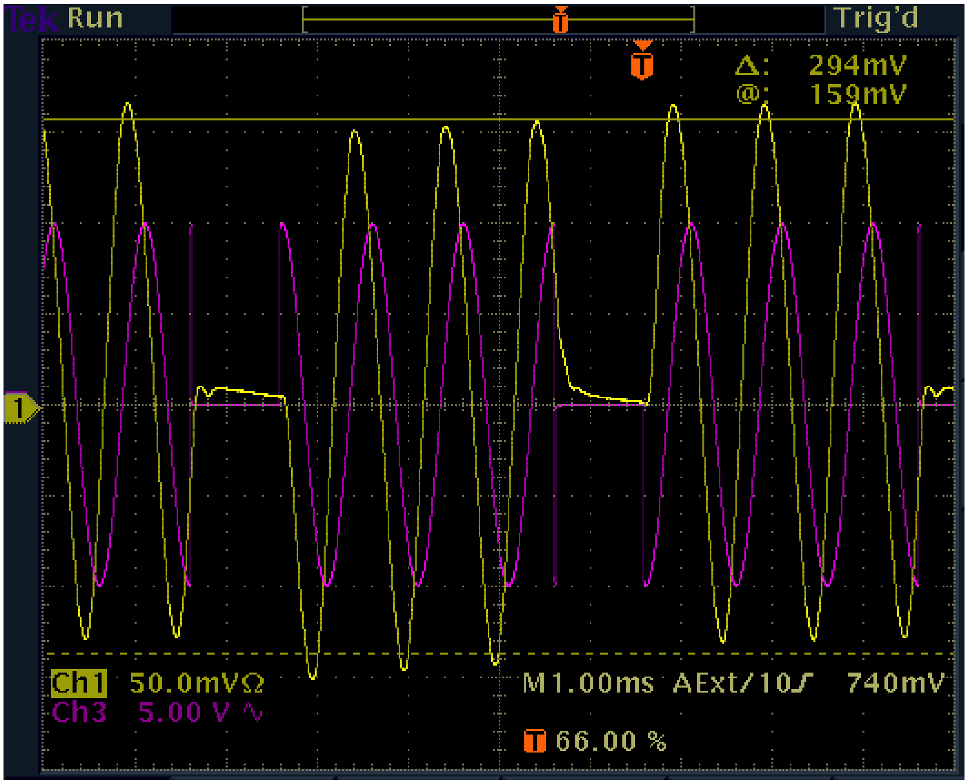

Figure 6.8: Ch1 shows the current through the quadrupole coils, while Ch3 shows the driving voltage. Although this data was collected in the offline trap, it shows clearly the results of using poorly-tuned starting parameters for the sinusoidal part of the waveform. In particular, note the non-uniform amplitude of the sinusoid, as well as its varying DC offset – both of which have been shown to harm the AC-MOT's ability to collect and retain atoms. One can also see the large residual current still present while the AC-MOT is "off".

6.5 Residual Magnetic Field in the Online Chamber

As is noted elsewhere, our goal is to produce a uniform magnetic field aligned with the axis of optical pumping as rapidly as possible after switching from the (non-uniform) quadrupole field that is needed to run the MOT.

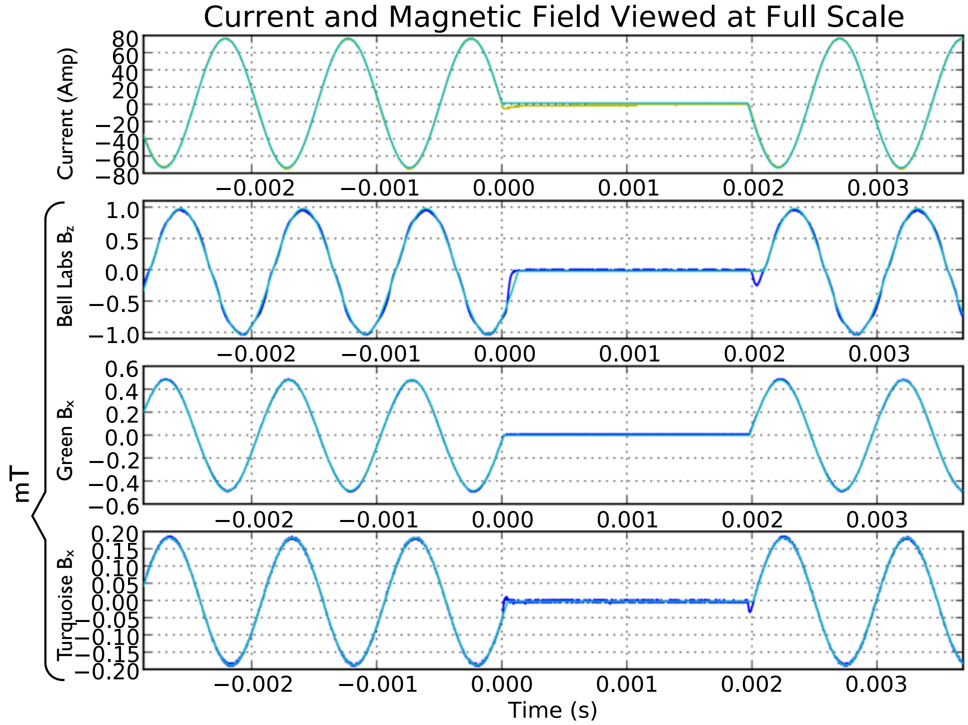

Figure 6.9: Current and magnetic field are shown as read out on an oscilloscope. The probes were positioned as in the second layout shown in Fig. 6.4. The waveform has been optimized to minimize the residual magnetic field in a '3 cycles on/2 cycles off' duty cycle at $f_{\mathrm{AC}} \approx 1017.9\,\mathrm{Hz}$, and entire scale of the readouts is shown. Yellow shows the current readout directly from the oscilloscope, while blue shows the magnetic field readout taken directly from the oscilloscope and converted into mT. The cyan curves which lie nearly on top of the readouts are fits. In all cases, the background has been subtracted off.

In Fig. 6.10, The magenta vertical lines show the time at which the AC-MOT part of the waveform goes on or off, as taken from the larger-

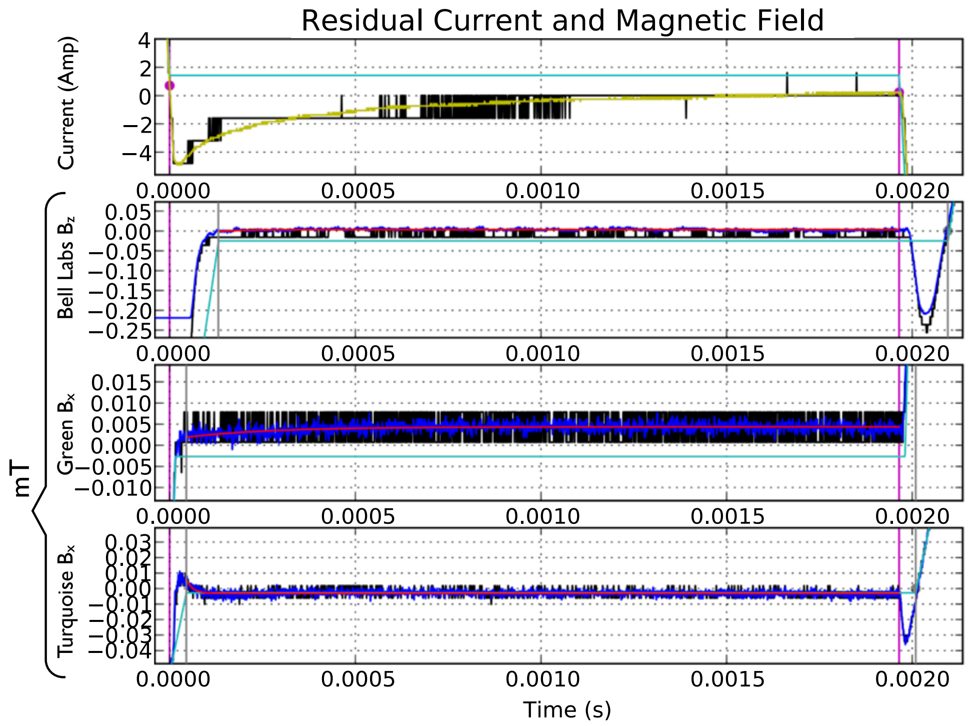

Figure 6.10: This plot shows data equivalent to that shown in Fig. 6.9 – however in this figure, the oscilloscope has been set to a more sensitive scale such that we are able to examine the magnetic field more closely during the time in which we intend it to be off. Note that this results in a systematic zero offset to the output. The backgrounds, as read out on this scale, have been subtracted off. The cyan curves show the fits as found from the data at a less precise scale in Fig. 6.9. On this intermediate scale, we see clearly that at least two of the three Hall probes pick up a spike when the sinusoidal part of the waveform begins or ends. These spikes are unlikely to accurately portray the magnetic field, as nothing to produce such readings is shown in the current readout from the coils. The coils are driven in voltage control mode, and a more plausible explanation is that the Hall probes or their leads are able to pick up on the voltage spikes sent to the coils when the AC-MOT part of the waveform begins or ends.

scale fit to the current. The grey vertical lines show the time at which the sinusoidal waveform resumes, as taken from the fits to the waveforms on the Hall probes. (The green and turquoise test kit Hall probes are very similar, however there is not an obvious voltage spike on the green test kit's readout. We use the measurements from the turqoise test kit to produce the vertical grey lines on both the green and turquoise test kits' plots.) The time delay between the magenta and grey lines gives us an estimate for how long the Hall probes are affected by a voltage spike. Therefore, we consider the waveform to be an inaccurate representation of the magnetic field during this same time delay at both the end and the beginning of the "magnetic field off" time. We fit the residual magnetic field only to parts of the readout which have not been excluded by this method.

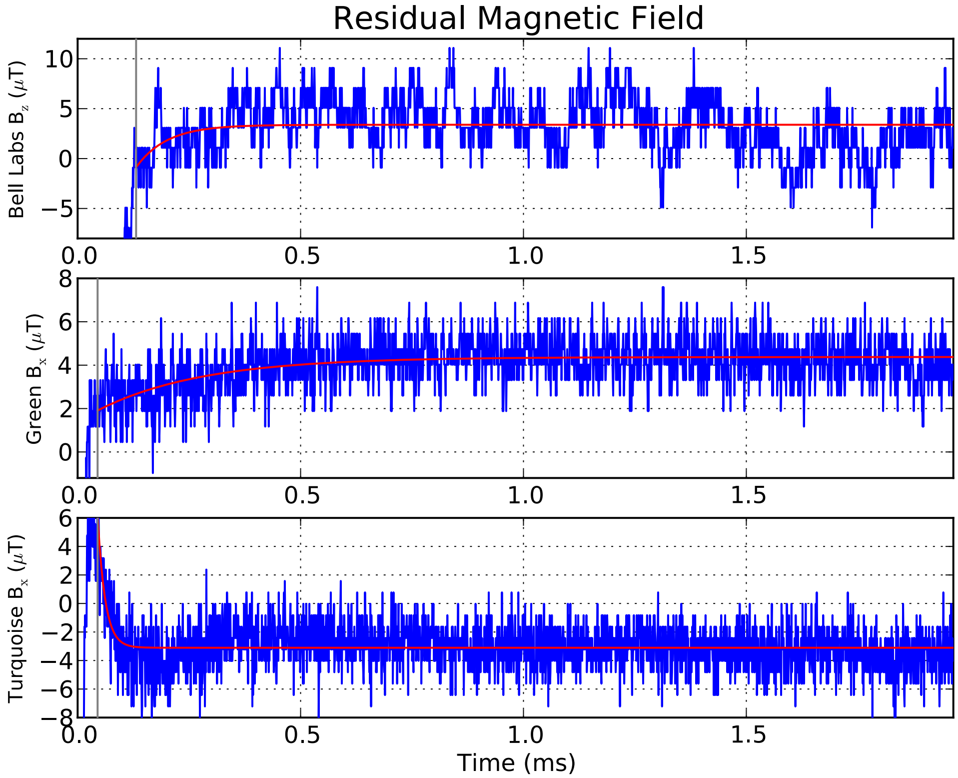

Figure 6.11: This plot shows the same data that can be seen in Fig. 6.10, however on this scale we are better able to see the features of the residual magnetic field. Fits to this data (for times after the grey lines) are shown in red.

6.6 Magnetic Field During Optical Pumping Time

The goal is to make a uniform dipole field while the AC-MOT is off, with as small a transverse field as possible, so as to allow optical pumping to better polarize the atoms. The results are shown below. All the figures in this section were created while using a waveform with three cycles on and two cycles off, at $f_{\mathrm{AC}} \approx 1017.9\,\mathrm{Hz}$.

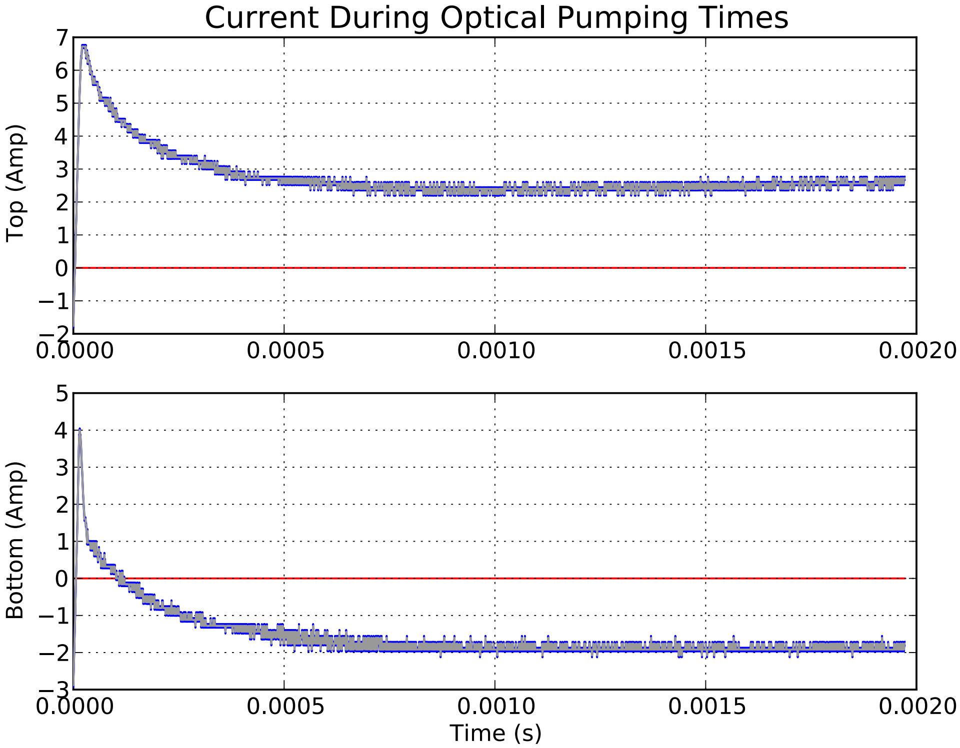

Figure 6.12: Current in the top and bottom power supplies during the optical pumping phase, as read out on the oscilloscope. The blue outline shows the systematic uncertainty due to limitations in the precision with which the power supplies were calibrated.

Unfortunately, it was not possible to measure the optical pumping field directly with a Hall probe, so estimates of the magnetic field must be made only from current data output from the power supplies. This fails to take into account any effects from eddy currents in the surrounding chamber,

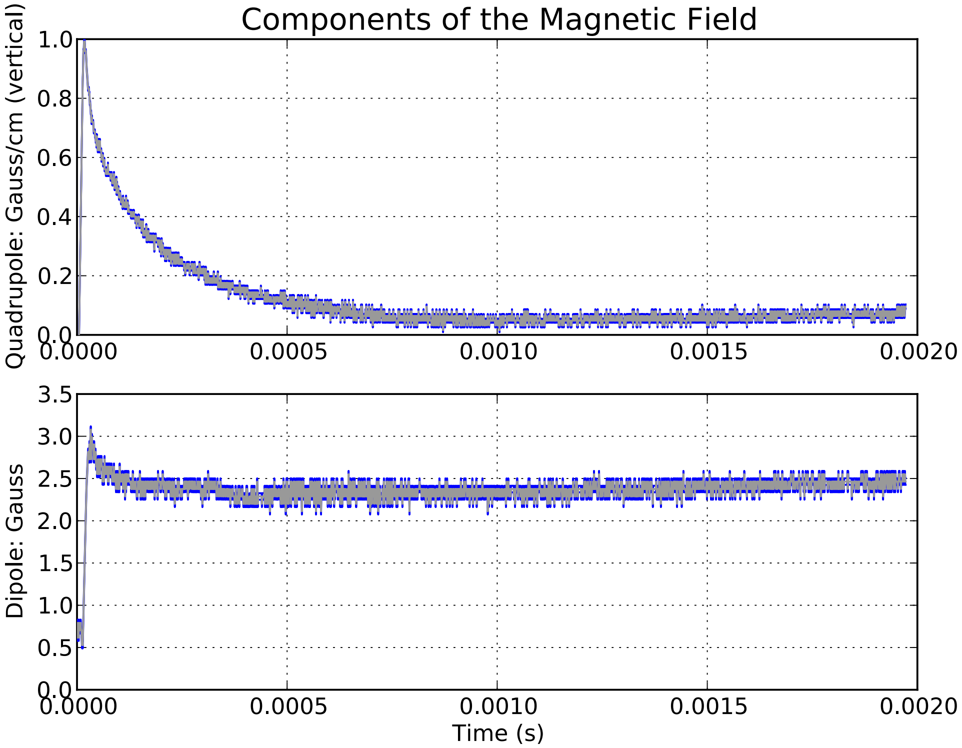

Figure 6.13: A model of the magnetic field resulting from the current in the coils. The blue outline shows the systematic uncertainty due to limitations in the precision with which the power supplies were calibrated. This was created by combining the current measurements in the coils (as shown in Fig. 6.12) with a COMSOL model of the coil geometry showing that each coil produces a magnetic field of magnitude 1.1 G/Amp at the centre, and a magnetic field gradient (along the vertical axis) of 0.2 G/cm/Amp at the centre. The current in the two coils may be run in parallel or antiparallel configurations to cancel out the quadrupole or dipole components of the field.

which is an important effect, so the quality of this method as an estimator for the magnetic field is not entirely clear.

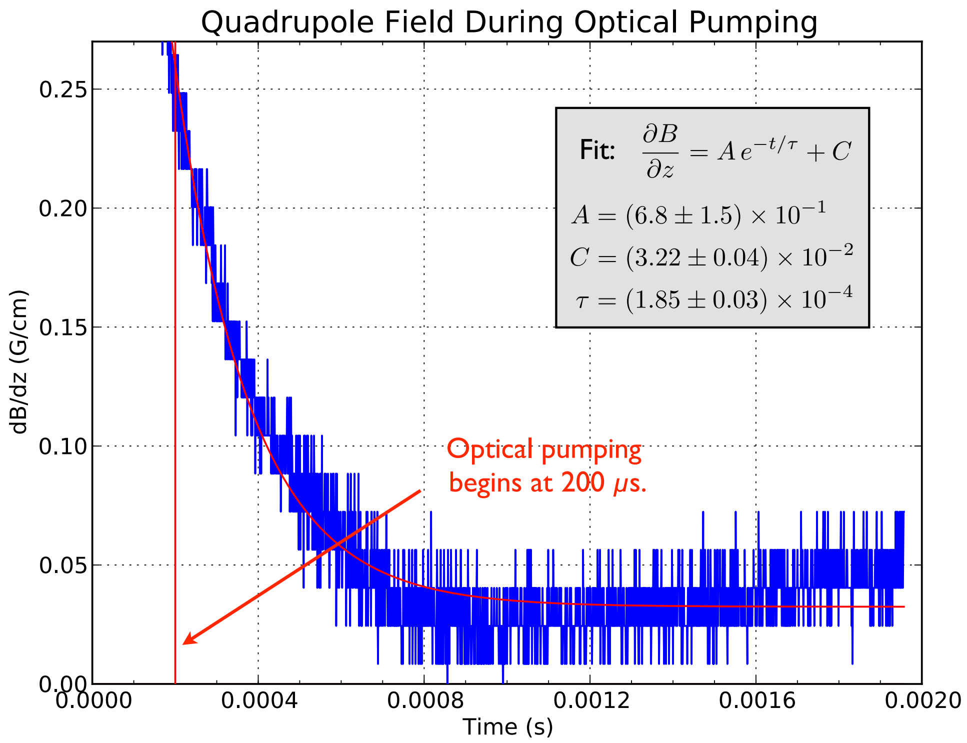

Figure 6.14: A closer look at the residual magnetic quadrupole field shown in Fig. 6.13. The field decays with a time constant of $\tau = 185\,\mu$s. The optical pumping laser is turned on $200\,mu$s after the AC-MOT is shut off, so as to avoid dealing with the worst of the residual quadrupole field during optical pumping.

Chapter 7

The Optical Bloch Equations

The optical Bloch equations are useful to describe the evolution of the quantum states in a sample of atoms in an optical molasses. In particular, we are interested in quantizing the extent to which the polarization of our sample of atoms is destroyed by stray magnetic fields.

The Optical Bloch Equations are specifically concerned with an atomic system including one valence electron in an electromagnetic field, usually produced by a laser. Though we speak of the density of states for a single atom, the description developed here may just as easily be applied to a statistical ensemble of many such atoms, provided that they do not interact with one another.

7.1 Explicit Form of the Density Matrix

Recall the standard definition of the density matrix,

$$\hat{\rho}(t) \;:=\; |\,\psi(t)\,\rangle\;\langle\,\psi(t)\,|\,. \tag{7.1}$$

We wish to describe $\hat{\rho}(t)$ and its time evolution explicitly in a basis chosen to simplify calculations. We select a basis such that the basis kets, $|\,i\,\rangle$, contain no time dependence. Thus, we write:

$$|\,\psi(t)\,\rangle \;=\; \sum_i c_i(t)\,|\,i\,\rangle \tag{7.2}$$

$$\langle\,\psi(t)\,| \;=\; \sum_i c_i^*(t)\,\langle\,i\,| \tag{7.3}$$

and

$$\hat{\rho}(t) \;=\; \sum_{i,j} c_i(t)\,c_j^*(t)\;|\,i\rangle\langle j\,|\,. \tag{7.4}$$

Equivalently, we show the matrix representation for a system of n basis states:

$$
\begin{aligned}
|\psi\rangle \quad &\longleftrightarrow \quad \begin{pmatrix} c_0 \\ c_1 \\ \vdots \\ c_n \end{pmatrix} && (7.5)\\
\langle\psi| \quad &\longleftrightarrow \quad \begin{pmatrix} c_0^* & c_1^* & \cdots & c_n^* \end{pmatrix} && (7.6)\\
\hat{\rho} \quad &\longleftrightarrow \quad \begin{pmatrix} c_0 c_0^* & c_0 c_1^* & \cdots & c_0 c_n^* \\ c_1 c_0^* & c_1 c_1^* & \cdots & c_1 c_n^* \\ \vdots & \vdots & \ddots & \vdots \\ c_n c_0^* & c_n c_1^* & \cdots & c_n c_n^* \end{pmatrix}. && (7.7)
\end{aligned}
$$

7.2 The General Form of Rotating Coordinates

We begin with a statement of the Schrödinger equation and its Hermitian conjugate.

$$
\begin{aligned}
\frac{d}{dt}|\psi\rangle \quad &= \quad \frac{1}{i\hbar}\hat{H}|\psi\rangle && (7.8)\\
\frac{d}{dt}\langle\psi| \quad &= \quad -\frac{1}{i\hbar}\langle\psi|\hat{H} && (7.9)
\end{aligned}
$$

We wish to describe the time-evolution of the density operator, $\hat{\rho}$, which we define as

$$
\hat{\rho} \quad := \quad |\psi\rangle\langle\psi|. \tag{7.10}
$$

It must then be the case that

$$
\begin{aligned}
\frac{d\hat{\rho}}{dt} \quad &= \quad \frac{d}{dt}\Big(|\psi\rangle\Big)\langle\psi| + |\psi\rangle\frac{d}{dt}\Big(\langle\psi|\Big) && (7.11)\\
&= \quad \frac{1}{i\hbar}\hat{H}|\psi\rangle\langle\psi| - \frac{1}{i\hbar}|\psi\rangle\langle\psi|\hat{H} && (7.12)\\
&= \quad \frac{1}{i\hbar}\Big(\hat{H}\hat{\rho} - \hat{\rho}\hat{H}\Big) && (7.13)\\
&= \quad \frac{1}{i\hbar}\Big[\hat{H},\, \hat{\rho}\Big]. && (7.14)
\end{aligned}
$$

We now consider the Hamiltonian, $\hat{H}$ for our system. Although in Section 7.1 we have constrained the basis kets of our system to have no time-dependence, we cannot guarantee that this will result in a time-independent Hamiltonian – in general, this will not be the case.

Although Eq. 7.14 is true for any Hamiltonian $\hat{H}$, we will henceforth take $\hat{H}_0 = \hat{H}$ to be the atomic Hamiltonian for a hydrogen-like atom with no external field and we consider a generalized change of coordinates described by a unitary transformation, $\hat{U}$. In general, $\hat{U} = \hat{U}(t)$ may be time-dependent, but it is useful to remember that any unitary transformation is only a generalized rotation matrix, and so the condition for unitarity is

$$\hat{U}\hat{U}^\dagger = \hat{U}^\dagger\hat{U} = \underset{\sim}{I}. \tag{7.15}$$

We define a new operator, $\widetilde{H}_0$, by

$$\widetilde{H}_0 := \hat{U}^\dagger\hat{H}_0\hat{U}. \tag{7.16}$$

It follows trivially that

$$\hat{H}_0 = \hat{U}\widetilde{H}_0\hat{U}^\dagger, \tag{7.17}$$

and so we return to considering the evolution of the density matrix $\hat{\rho}$. From Eq. 7.13, we find that:

$$\begin{align}
\frac{d\hat{\rho}}{dt} &= \frac{1}{i\hbar}\left(\hat{H}_0\hat{\rho} - \hat{\rho}\hat{H}_0\right) \tag{7.18} \\
&= \frac{1}{i\hbar}\left(\hat{U}\widetilde{H}_0\hat{U}^\dagger\hat{\rho} - \hat{\rho}\,\hat{U}\widetilde{H}_0\hat{U}^\dagger\right) \tag{7.19} \\
\hat{U}^\dagger\,\frac{d\hat{\rho}}{dt}\,\hat{U} &= \frac{1}{i\hbar}\left(\hat{U}^\dagger\hat{U}\widetilde{H}_0\hat{U}^\dagger\hat{\rho}\,\hat{U} - \hat{U}^\dagger\hat{\rho}\,\hat{U}\widetilde{H}_0\hat{U}^\dagger\hat{U}\right) \tag{7.20} \\
&= \frac{1}{i\hbar}\left(\widetilde{H}_0\,\hat{U}^\dagger\hat{\rho}\,\hat{U} - \hat{U}^\dagger\hat{\rho}\,\hat{U}\,\widetilde{H}_0\right). \tag{7.21}
\end{align}$$

At this point, we begin to suspect that it may be advantageous to define a "transformed" density matrix, $\widetilde{\rho}$, as

$$\widetilde{\rho} := \hat{U}^\dagger\hat{\rho}\,\hat{U}. \tag{7.22}$$

Then,

$$\hat{U}^\dagger\,\frac{d\hat{\rho}}{dt}\,\hat{U} = \frac{1}{i\hbar}\left(\widetilde{H}_0\widetilde{\rho} - \widetilde{\rho}\widetilde{H}_0\right), \tag{7.23}$$

but we will wish to eliminate all references to $\hat{\rho}$, instead writing this expression in terms of only $\widetilde{\rho}$. Thus, remembering that $\hat{U}$ may be time-dependent,

$$\begin{aligned}\frac{d\widetilde{\rho}}{dt} &= \frac{d}{dt}\left(\hat{U}^\dagger \hat{\rho}\, \hat{U}\right) &(7.24)\\ &= \frac{d\hat{U}^\dagger}{dt}\hat{\rho}\,\hat{U} + \hat{U}^\dagger \frac{d\hat{\rho}}{dt}\hat{U} + \hat{U}^\dagger \hat{\rho}\,\frac{d\hat{U}}{dt} &(7.25)\\ &= \frac{1}{i\hbar}\left(\widetilde{H}_0\widetilde{\rho} - \widetilde{\rho}\widetilde{H}_0\right) + \frac{d\hat{U}^\dagger}{dt}\hat{\rho}\,\hat{U} + \hat{U}^\dagger\hat{\rho}\,\frac{d\hat{U}}{dt} &(7.26)\\ &= \frac{1}{i\hbar}\left(\widetilde{H}_0\widetilde{\rho} - \widetilde{\rho}\widetilde{H}_0\right) + \frac{d\hat{U}^\dagger}{dt}\hat{U}\hat{U}^\dagger\hat{\rho}\,\hat{U} + \hat{U}^\dagger\hat{\rho}\,\hat{U}\hat{U}^\dagger\frac{d\hat{U}}{dt} &(7.27)\\ &= \frac{1}{i\hbar}\left(\widetilde{H}_0\widetilde{\rho} - \widetilde{\rho}\widetilde{H}_0\right) + \frac{d\hat{U}^\dagger}{dt}\hat{U}\,\widetilde{\rho} + \widetilde{\rho}\,\hat{U}^\dagger\frac{d\hat{U}}{dt}. &(7.28)\end{aligned}$$

We must now recall the unitarity condition, Eq. 7.15, which allows us to further simplify our expression for $\frac{d\widetilde{\rho}}{dt}$, using

$$\frac{d}{dt}\left(\hat{U}\hat{U}^\dagger\right) = \frac{d}{dt}\left(\hat{U}^\dagger\hat{U}\right) = \frac{d}{dt}\left(\underset{\sim}{I}\right) = 0 \qquad (7.29)$$

$$\begin{aligned}\frac{d\hat{U}^\dagger}{dt}\hat{U} &= -\hat{U}^\dagger\frac{d\hat{U}}{dt} &(7.30)\\ \hat{U}\frac{d\hat{U}^\dagger}{dt} &= -\frac{d\hat{U}}{dt}\hat{U}^\dagger. &(7.31)\end{aligned}$$

Then Eq. 7.28 becomes

$$\begin{aligned}\frac{d\widetilde{\rho}}{dt} &= \frac{1}{i\hbar}\left(\widetilde{H}_0\widetilde{\rho} - \widetilde{\rho}\widetilde{H}_0\right) + \frac{d\hat{U}^\dagger}{dt}\hat{U}\,\widetilde{\rho} - \widetilde{\rho}\,\frac{d\hat{U}^\dagger}{dt}\hat{U} &(7.32)\\ &= \frac{1}{i\hbar}\left[\widetilde{H}_0,\, \widetilde{\rho}\right] + \left[\frac{d\hat{U}^\dagger}{dt}\hat{U},\, \widetilde{\rho}\right]. &(7.33)\end{aligned}$$

Thus, we will find it useful to define an “effective Hamiltonian”, $\widetilde{H}_0'$, by

$$\begin{aligned}\widetilde{H}_0' &:= \widetilde{H}_0 + i\hbar\,\frac{d\hat{U}^\dagger}{dt}\hat{U} &(7.34)\\ &= \hat{U}^\dagger\hat{H}_0\hat{U} + i\hbar\,\frac{d\hat{U}^\dagger}{dt}\hat{U}. &(7.35)\end{aligned}$$

This notation considerably simplifies our expression for the evolution of $\widetilde{\rho}$. Indeed, we find that

$$\frac{d\widetilde{\rho}}{dt} = \frac{1}{i\hbar}\left[\widetilde{H}_0',\, \widetilde{\rho}\right], \qquad (7.36)$$

just as we might have guessed from Eq. 7.14.

It would be nice, at this stage, to select a transformation $\hat{U}$ will be useful. We'll assume from this point forward that $\hat{H}$ is a basis in which the Hamiltonian is already diagonalized. We hope to find a $\hat{U}$ such that $\frac{d\widetilde{\rho}}{dt} = 0$, which will simplify evaluating the time evolution of our system. Therefore, from Eq. 7.33,

$$\left[\widetilde{H}_0,\, \widetilde{\rho}\right] \;=\; -\, i\hbar \left[\frac{d\hat{U}^\dagger}{dt}\hat{U},\, \widetilde{\rho}\right], \tag{7.37}$$

which can be solved by setting

$$\frac{d\hat{U}^\dagger}{dt} \;=\; -\frac{1}{i\hbar}\,\widetilde{H}_0\,\hat{U}^\dagger \;=\; -\frac{1}{i\hbar}\,\hat{U}^\dagger\hat{H}_0. \tag{7.38}$$

Then $\hat{U}^\dagger$ has the form of an exponential. In particular,

$$\begin{aligned}\hat{U}^\dagger &= A\, e^{+i\hat{H}_0 t/\hbar}\\ \hat{U} &= A^* e^{-i\hat{H}_0 t/\hbar},\end{aligned}$$

and enforcing unitarity, we note that $A^*A = 1$, so without loss of generality we choose $A = 1$ and find that our equation is solved by

$$\hat{U}^\dagger = e^{+i\hat{H}_0 t/\hbar} \tag{7.39}$$

$$\hat{U} = e^{-i\hat{H}_0 t/\hbar}. \tag{7.40}$$

7.3 Derivation of a Toy-Model Set of Optical Bloch Equations

We'll derive the model used in Ref. [10], and also extend it. We'll use an $I = 1/2$ atom (eg, Hydrogen), and consider only the $F = 0$ excited state and $F = 1$ ground states. See Fig. 7.1, which was taken from Ref. [4].

We'll want to find a Hamiltonian, H, which describes all the relevant physical processes in our system. Therefore, we write,

$$H = H_0 + H_L + H_B, \tag{7.41}$$

where H_0 is the unperturbed atomic Hamiltonian, H_L represents the interaction between the laser and the atoms, and H_B is the part of the Hamiltonian resulting from magnetic effects.

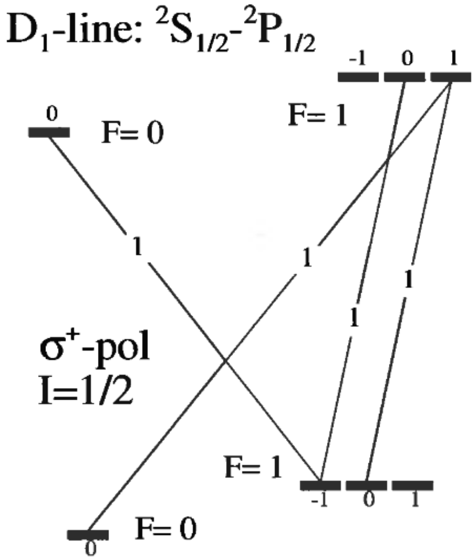

Figure 7.1: Transition strengths for a Hydrogen-like atom with nuclear spin $I = 1/2$, in a σ^+ radiation field [4]. To find the σ^- transition strengths, multiply all the m values by -1.

Initially, we will use the following as our basis states:

$$|F_g = 1, m_z = +1\rangle = \begin{bmatrix} 1 \\ 0 \\ 0 \\ 0 \end{bmatrix}; \; |F_g = 1, m_z = 0\rangle = \begin{bmatrix} 0 \\ 1 \\ 0 \\ 0 \end{bmatrix}$$

$$|F_g = 1, m_z = -1\rangle = \begin{bmatrix} 0 \\ 0 \\ 1 \\ 0 \end{bmatrix}; \; |F_e = 0, m_z = 0\rangle = \begin{bmatrix} 0 \\ 0 \\ 0 \\ 1 \end{bmatrix}. \tag{7.42}$$

Then, our unperturbed atomic Hamiltonian is given by

$$H_0 = \begin{bmatrix} 0 & 0 & 0 & 0 \\ 0 & 0 & 0 & 0 \\ 0 & 0 & 0 & 0 \\ 0 & 0 & 0 & \hbar\omega_0 \end{bmatrix}. \tag{7.43}$$

Note that we have selected a system in which the spin-orbit coupling is identically zero for the ground states, and may be considered already included in the excited state energy, $\hbar\omega_0$.

We now consider magnetic perturbations to our Hamiltonian. In general,

$$\begin{aligned} H_B &= -\vec{\mu}\cdot\vec{B} && (7.44) \\ &= g\mu_0\,\vec{F}\cdot\vec{B}. && (7.45) \end{aligned}$$

It is standard practice to take the magnetic field as being directed along the axis of quantization, and to label this direction as $\hat{z}$. Instead, we shall refer to the orientation of the magnetic field as $\hat{z}'$, as it is not, in general, exactly aligned with the axis of optical pumping, which will later be referred to as $\hat{z}$. Furthermore, primes will be used to designate terms which are described under the basis in which the $\hat{z}'$ axis is used as the axis of quantization. Under this convention, the perturbation to atomic energy levels is simply

$$\Delta E_{B'} = g\mu_0\,B\,F_{z'}. \tag{7.46}$$

Letting $\gamma = \mu_0 g$, we also define the Larmor frequency Ω_L according to

$$\Omega_L = \gamma B = \mu_0 g\,B, \tag{7.47}$$

so that our Hamiltonian in this basis becomes

$$H_{B'} = \begin{bmatrix} \hbar\Omega_L & 0 & 0 & 0 \\ 0 & 0 & 0 & 0 \\ 0 & 0 & -\hbar\Omega_L & 0 \\ 0 & 0 & 0 & 0 \end{bmatrix}. \tag{7.48}$$

This result must still be transformed into the laboratory frame coordinate basis so that it can be combined with the other terms in the complete Hamiltonian. We seek to apply a rotation operator of the form

$$\begin{aligned} H_B &= R^\dagger H_{B'} R && (7.49) \\ &= e^{i\phi J_{\hat{n}}}\,H_{B'}\,e^{-i\phi J_{\hat{n}}} && (7.50) \end{aligned}$$

for a rotation of angle ϕ about the $\hat{n}$-axis, where $J_{\hat{n}}$ is the generator of this rotation, and is normalized to obey the commutation relation,

$$\left[J_{\hat{\imath}}, J_{\hat{\jmath}}\right] = i\,\epsilon_{ijk}\,J_{\hat{k}}. \tag{7.51}$$

Our Hamiltonian combines an $F = 1$ and $F = 0$ representation, therefore we define the following generators of rotation:

$$J_{\hat{x}} = \frac{1}{\sqrt{2}}\begin{bmatrix} 0 & 1 & 0 & 0 \\ 1 & 0 & 1 & 0 \\ 0 & 1 & 0 & 0 \\ 0 & 0 & 0 & 0 \end{bmatrix}, \tag{7.52}$$

$$J_{\hat{y}} = \frac{1}{\sqrt{2}}\begin{bmatrix} 0 & -i & 0 & 0 \\ +i & 0 & -i & 0 \\ 0 & +i & 0 & 0 \\ 0 & 0 & 0 & 0 \end{bmatrix}, \tag{7.53}$$

$$J_{\hat{z}} = \begin{bmatrix} +1 & 0 & 0 & 0 \\ 0 & 0 & 0 & 0 \\ 0 & 0 & -1 & 0 \\ 0 & 0 & 0 & 0 \end{bmatrix}. \tag{7.54}$$

Without loss of generality, we take the transverse component of $\vec{B}$ to be directed along the $\hat{y}$ axis. That is,

$$\begin{aligned} \vec{B} &= B\,\hat{z}' && (7.55) \\ &= B\cos\phi\,\hat{z} + B\sin\phi\,\hat{y}, && (7.56) \end{aligned}$$

so that the $\hat{z}'$-axis is related to the $\hat{z}$-axis by a rotation of angle ϕ about the $\hat{x} = \hat{x}'$ axis. Explicitly,

$$\begin{aligned} H_B = & \begin{bmatrix} \frac{1}{2}(1+\cos\phi) & \frac{i}{\sqrt{2}}\sin\phi & \frac{1}{2}(\cos\phi - 1) & 0 \\ \frac{i}{\sqrt{2}}\sin\phi & \cos\phi & \frac{i}{\sqrt{2}}\sin\phi & 0 \\ \frac{1}{2}(\cos\phi - 1) & \frac{i}{\sqrt{2}}\sin\phi & \frac{1}{2}(1+\cos\phi) & 0 \\ 0 & 0 & 0 & 1 \end{bmatrix} \begin{bmatrix} \hbar\Omega_L & 0 & 0 & 0 \\ 0 & 0 & 0 & 0 \\ 0 & 0 & -\hbar\Omega_L & 0 \\ 0 & 0 & 0 & 0 \end{bmatrix} \\ & \times \begin{bmatrix} \frac{1}{2}(1+\cos\phi) & \frac{-i}{\sqrt{2}}\sin\phi & \frac{1}{2}(\cos\phi - 1) & 0 \\ \frac{-i}{\sqrt{2}}\sin\phi & \cos\phi & \frac{-i}{\sqrt{2}}\sin\phi & 0 \\ \frac{1}{2}(\cos\phi - 1) & \frac{-i}{\sqrt{2}}\sin\phi & \frac{1}{2}(1+\cos\phi) & 0 \\ 0 & 0 & 0 & 1 \end{bmatrix}, \end{aligned} \tag{7.57}$$

and we find that

$$H_B = \begin{bmatrix} \hbar\Omega_L\cos\phi & \frac{-i}{\sqrt{2}}\hbar\Omega_L\sin\phi & 0 & 0 \\ \frac{i}{\sqrt{2}}\hbar\Omega_L\sin\phi & 0 & \frac{-i}{\sqrt{2}}\hbar\Omega_L\sin\phi & 0 \\ 0 & \frac{i}{\sqrt{2}}\hbar\Omega_L\sin\phi & -\hbar\Omega_L\cos\phi & 0 \\ 0 & 0 & 0 & 0 \end{bmatrix}. \tag{7.58}$$

We now turn our attention to the system's interaction with the laser beam. Quite generally, this part of the Hamiltonian may be written as

$$H_L = -\vec{d}\cdot\vec{E} \tag{7.59}$$

where $\vec{E}$ is the electric field, and $\vec{d}$ is the induced dipole moment between sets of atomic states, and is taken to always be parallel to $\vec{E}$. It is now incumbent upon us to find a proper mathematical description for both $\vec{E}$ and $\vec{d}$.

We begin by considering the dipole operator, $\vec{d}$. Ref. [10] is kind enough to suggest a decomposition of the $\hat{x}$-component of the dipole operator into its raising and lowering operator components, as:

$$d_x \equiv \vec{d} \cdot \hat{x} = \frac{1}{\sqrt{2}} \left(d_{-1} - d_{+1} \right), \tag{7.60}$$

and we define the related quantity,

$$d_y \equiv \vec{d} \cdot \hat{y} = \frac{i}{\sqrt{2}} \left(d_{-1} + d_{+1} \right), \tag{7.61}$$

which is chosen so as to satisfy properties of linear independence and Hermiticity.

We will now consider the electric field, which we treat as a semiclassical electromagnetic wave oscillating in the xy-plane. For the case of circularly polarized light in which we are interested, we write

$$\begin{aligned} \vec{E} &= \frac{1}{\sqrt{2}} E_0 \left[\cos(\omega_L t)\hat{x} + \cos(\omega_L t \pm \pi/2)\hat{y} \right] & (7.62) \\ &= \frac{1}{\sqrt{2}} E_0 \left[\cos(\omega_L t)\hat{x} \mp \sin(\omega_L t)\hat{y} \right] & (7.63) \\ &= \frac{1}{\sqrt{2}} E_0 \left[\frac{1}{2} \left(e^{+i\omega_L t} + e^{-i\omega_L t} \right) \hat{x} \mp \frac{1}{2i} \left(e^{+i\omega_L t} - e^{-i\omega_L t} \right) \hat{y} \right] & (7.64) \end{aligned}$$

for σ_- and σ_+ polarizations respectively, and the atom-laser Hamiltonian from 7.59 becomes

$$\begin{aligned} H_L &= -\frac{1}{2} E_0 \left[\left(d_{-1} - d_{+1} \right) \cos(\omega_L t) \mp i \left(d_{-1} + d_{+1} \right) \sin(\omega_L t) \right] & (7.65) \\ &= -\frac{1}{2} E_0 \left[\frac{1}{2} \left(e^{+i\omega_L t} + e^{-i\omega_L t} \right) \left(d_{-1} - d_{+1} \right) \right. \\ &\quad \left. \mp \frac{1}{2} \left(e^{+i\omega_L t} - e^{-i\omega_L t} \right) \left(d_{-1} + d_{+1} \right) \right]. & (7.66) \end{aligned}$$

If we consider only one mode of circular polarization, this result may be simplified. We will now substitute $H_L = H_-$ or $H_L = H_+$ (where the subscript denotes the handedness of polarization), and we find that

$$\begin{aligned} H_- &= E_0 \left(e^{+i\omega_L t} \, d_{+1} - e^{-i\omega_L t} \, d_{-1} \right) & (7.67) \\ H_+ &= E_0 \left(e^{-i\omega_L t} \, d_{+1} - e^{+i\omega_L t} \, d_{-1} \right). & (7.68) \end{aligned}$$

We'll need to find our raising and lowering operators, d_{+1} and d_{-1} in this basis. We define the Rabi frequency (the factor of $\sqrt{3}$ is specific to this system) as

$$\Omega_R \equiv \frac{E_0}{\hbar\sqrt{3}} \langle F_1 || d || F_2 \rangle . \tag{7.69}$$

The Wigner-Eckart Theorem states that

$$\langle F_1 m_1 || d_\pm || F_2 m_2 \rangle = \frac{\hbar\sqrt{3}}{E_0} \Omega_R (-1)^{F_1 - m_1} \begin{pmatrix} F_1 & 1 & F_2 \\ -m_1 & \pm 1 & m_2 \end{pmatrix}, \tag{7.70}$$

and therefore,

$$d_{+1} = \frac{\hbar\Omega_R}{E_0} \begin{bmatrix} 0 & 0 & 0 & 0 \\ 0 & 0 & 0 & 0 \\ 0 & 0 & 0 & +1 \\ -1 & 0 & 0 & 0 \end{bmatrix} \tag{7.71}$$

$$d_{-1} = \frac{\hbar\Omega_R}{E_0} \begin{bmatrix} 0 & 0 & 0 & +1 \\ 0 & 0 & 0 & 0 \\ 0 & 0 & 0 & 0 \\ 0 & 0 & -1 & 0 \end{bmatrix} . \tag{7.72}$$

Our atom-laser interaction Hamiltonians become

$$H_- = \hbar\Omega_R \begin{bmatrix} 0 & 0 & 0 & +e^{+i\omega_L t} \\ 0 & 0 & 0 & 0 \\ 0 & 0 & 0 & -e^{-i\omega_L t} \\ +e^{-i\omega_L t} & 0 & -e^{+i\omega_L t} & 0 \end{bmatrix} \tag{7.73}$$

$$H_+ = \hbar\Omega_R \begin{bmatrix} 0 & 0 & 0 & +e^{-i\omega_L t} \\ 0 & 0 & 0 & 0 \\ 0 & 0 & 0 & -e^{+i\omega_L t} \\ +e^{+i\omega_L t} & 0 & -e^{-i\omega_L t} & 0 \end{bmatrix} . \tag{7.74}$$

Finally, we are in a position to add together all the pieces of the Hamiltonian. We find, for polarizations σ_- and σ_+:

$$H = \hbar \begin{bmatrix} \Omega_L \cos\phi & \frac{-i}{\sqrt{2}}\,\Omega_L \sin\phi & 0 & +\Omega_R\, e^{\pm i\omega_L t} \\ \frac{i}{\sqrt{2}}\,\Omega_L \sin\phi & 0 & \frac{-i}{\sqrt{2}}\,\Omega_L \sin\phi & 0 \\ 0 & \frac{i}{\sqrt{2}}\,\Omega_L \sin\phi & -\Omega_L \cos\phi & -\Omega_R\, e^{\mp i\omega_L t} \\ +\Omega_R\, e^{\mp i\omega_L t} & 0 & -\Omega_R\, e^{\pm i\omega_L t} & \omega_0 \end{bmatrix} . \tag{7.75}$$

We are now ready to make the customary change to rotating coordinates. We choose as the basis for the coordinate change,

$$U = e^{-iAt} \tag{7.76}$$

and

$$A = \begin{bmatrix} 0 & 0 & 0 & 0 \\ 0 & 0 & 0 & 0 \\ 0 & 0 & 0 & 0 \\ 0 & 0 & 0 & \omega_L \end{bmatrix}, \tag{7.77}$$

and define the following quantities:

$$\begin{aligned} \tilde{\rho} &\equiv U^{\dagger} \rho\, U & (7.78) \\ \tilde{H} &\equiv U^{\dagger} H U - \hbar A. & (7.79) \end{aligned}$$

In terms of these new variables, the time evolution equation is

$$\frac{d\tilde{\rho}}{dt} = \frac{1}{i\hbar} \left[\tilde{H}, \tilde{\rho} \right]. \tag{7.80}$$

We write out the full rotating-coordinate Hamiltonians explicitly:

$$\tilde{H}_{tot-} = \hbar \begin{bmatrix} \Omega_L \cos\phi & \frac{-i}{\sqrt{2}}\,\Omega_L \sin\phi & 0 & \Omega_R \\ \frac{i}{\sqrt{2}}\,\Omega_L \sin\phi & 0 & \frac{-i}{\sqrt{2}}\,\Omega_L \sin\phi & 0 \\ 0 & \frac{i}{\sqrt{2}}\,\Omega_L \sin\phi & -\Omega_L \cos\phi & -\Omega_R\, e^{-2i\omega_L t} \\ \Omega_R & 0 & -\Omega_R\, e^{+2i\omega_L t} & (\omega_0 - \omega_L) \end{bmatrix} \tag{7.81}$$

$$\tilde{H}_{tot+} = \hbar \begin{bmatrix} \Omega_L \cos\phi & \frac{-i}{\sqrt{2}}\,\Omega_L \sin\phi & 0 & +\Omega_R\, e^{-2i\omega_L t} \\ \frac{i}{\sqrt{2}}\,\Omega_L \sin\phi & 0 & \frac{-i}{\sqrt{2}}\,\Omega_L \sin\phi & 0 \\ 0 & \frac{i}{\sqrt{2}}\,\Omega_L \sin\phi & -\Omega_L \cos\phi & -\Omega_R \\ \Omega_R\, e^{+2i\omega_L t} & 0 & -\Omega_R & (\omega_0 - \omega_L) \end{bmatrix}. \tag{7.82}$$

The "fast-rotating" terms which will be discarded to make the rotating wave approximation immediately suggest themselves, and we find that

$$\tilde{H}_{tot-} \approx \hbar \begin{bmatrix} \Omega_L \cos\phi & \frac{-i}{\sqrt{2}}\,\Omega_L \sin\phi & 0 & \Omega_R \\ \frac{i}{\sqrt{2}}\,\Omega_L \sin\phi & 0 & \frac{-i}{\sqrt{2}}\,\Omega_L \sin\phi & 0 \\ 0 & \frac{i}{\sqrt{2}}\,\Omega_L \sin\phi & -\Omega_L \cos\phi & 0 \\ \Omega_R & 0 & 0 & (\omega_0 - \omega_L) \end{bmatrix} \tag{7.83}$$

$$\tilde{H}_{tot+} \approx \hbar \begin{bmatrix} \Omega_L \cos\phi & \frac{-i}{\sqrt{2}}\,\Omega_L \sin\phi & 0 & 0 \\ \frac{i}{\sqrt{2}}\,\Omega_L \sin\phi & 0 & \frac{-i}{\sqrt{2}}\,\Omega_L \sin\phi & 0 \\ 0 & \frac{i}{\sqrt{2}}\,\Omega_L \sin\phi & -\Omega_L \cos\phi & -\Omega_R \\ 0 & 0 & -\Omega_R & (\omega_0 - \omega_L) \end{bmatrix}. \tag{7.84}$$

We will henceforth take the incident light to be entirely σ_+ polarized, and take $\tilde{H} = \tilde{H}_{tot+}$ as the Hamiltonian of the system, dropping the subscripts.

The master equation (7.80) is still incomplete without additional terms to describe spontaneous decay from the excited state to the ground states. These must be added in by hand. In general, we are able to describe this dephasing behavior by

$$\left.\frac{\partial\rho}{\partial t}\right|_{spont} = \left.\frac{\partial\rho}{\partial t}\right|_{relax} + \left.\frac{\partial\rho}{\partial t}\right|_{repop}, \tag{7.85}$$

where

$$\left.\frac{\partial\rho}{\partial t}\right|_{relax} = -\frac{1}{2}\left(\hat{\Gamma}\rho + \rho\hat{\Gamma}\right) \tag{7.86}$$

$$\left.\frac{\partial\rho}{\partial t}\right|_{repop} = \hat{\Lambda}, \tag{7.87}$$

and where $\hat{\Gamma}$ and $\hat{\Lambda}$ are both diagonal matrices [10]. In the system we are considering, there is only a single excited state with equal coupling to each of the three ground states. Therefore, if atoms in the excited state spontaneously decay at a rate $\Gamma\rho_{ex} = \Gamma\rho_{33} = \Gamma\tilde{\rho}_{33}$,

$$\hat{\Gamma} = \begin{bmatrix} 0 & 0 & 0 & 0 \\ 0 & 0 & 0 & 0 \\ 0 & 0 & 0 & 0 \\ 0 & 0 & 0 & \Gamma \end{bmatrix}. \tag{7.88}$$

Because each of the three ground states are repopulated at an equal rate as a result of spontaneous emission from the population $\rho_{33} = \tilde{\rho}_{33}$, we find that

$$\hat{\Lambda} = \frac{1}{3}\Gamma\rho_{33}\begin{bmatrix} 1 & 0 & 0 & 0 \\ 0 & 1 & 0 & 0 \\ 0 & 0 & 1 & 0 \\ 0 & 0 & 0 & 0 \end{bmatrix}. \tag{7.89}$$

It should be noted that the form of Eqs. (7.86), (7.87), (7.88), and (7.89) remains unaltered under a coordinate transformation between laboratory and rotating coordinates. The master equation becomes

$$\frac{d\tilde{\rho}}{dt} = \frac{1}{i\hbar}\left[\tilde{H}, \tilde{\rho}\right] + \left.\frac{\partial\tilde{\rho}}{\partial t}\right|_{spont} \tag{7.90}$$

$$= \frac{1}{i\hbar}\left[\tilde{H}, \tilde{\rho}\right] - \frac{1}{2}\left(\hat{\Gamma}\tilde{\rho} + \tilde{\rho}\hat{\Gamma}\right) + \hat{\Lambda}. \tag{7.91}$$

We write the matrices of Eq. 7.91 out in explicit detail:

$$
\begin{aligned}
\frac{d}{dt}\begin{bmatrix} \tilde{\rho}_{00} & \tilde{\rho}_{01} & \tilde{\rho}_{02} & \tilde{\rho}_{03} \\ \tilde{\rho}_{10} & \tilde{\rho}_{11} & \tilde{\rho}_{12} & \tilde{\rho}_{13} \\ \tilde{\rho}_{20} & \tilde{\rho}_{21} & \tilde{\rho}_{22} & \tilde{\rho}_{23} \\ \tilde{\rho}_{30} & \tilde{\rho}_{31} & \tilde{\rho}_{32} & \tilde{\rho}_{33} \end{bmatrix} &= \\
-i\begin{bmatrix} \Omega_L\cos\phi & \frac{-i}{\sqrt{2}}\Omega_L\sin\phi & 0 & 0 \\ \frac{i}{\sqrt{2}}\Omega_L\sin\phi & 0 & \frac{-i}{\sqrt{2}}\Omega_L\sin\phi & 0 \\ 0 & \frac{i}{\sqrt{2}}\Omega_L\sin\phi & -\Omega_L\cos\phi & -\Omega_R \\ 0 & 0 & -\Omega_R & (\omega_0-\omega_L) \end{bmatrix}&\begin{bmatrix} \tilde{\rho}_{00} & \tilde{\rho}_{01} & \tilde{\rho}_{02} & \tilde{\rho}_{03} \\ \tilde{\rho}_{10} & \tilde{\rho}_{11} & \tilde{\rho}_{12} & \tilde{\rho}_{13} \\ \tilde{\rho}_{20} & \tilde{\rho}_{21} & \tilde{\rho}_{22} & \tilde{\rho}_{23} \\ \tilde{\rho}_{30} & \tilde{\rho}_{31} & \tilde{\rho}_{32} & \tilde{\rho}_{33} \end{bmatrix} \\
+i\begin{bmatrix} \tilde{\rho}_{00} & \tilde{\rho}_{01} & \tilde{\rho}_{02} & \tilde{\rho}_{03} \\ \tilde{\rho}_{10} & \tilde{\rho}_{11} & \tilde{\rho}_{12} & \tilde{\rho}_{13} \\ \tilde{\rho}_{20} & \tilde{\rho}_{21} & \tilde{\rho}_{22} & \tilde{\rho}_{23} \\ \tilde{\rho}_{30} & \tilde{\rho}_{31} & \tilde{\rho}_{32} & \tilde{\rho}_{33} \end{bmatrix}&\begin{bmatrix} \Omega_L\cos\phi & \frac{-i}{\sqrt{2}}\Omega_L\sin\phi & 0 & 0 \\ \frac{i}{\sqrt{2}}\Omega_L\sin\phi & 0 & \frac{-i}{\sqrt{2}}\Omega_L\sin\phi & 0 \\ 0 & \frac{i}{\sqrt{2}}\Omega_L\sin\phi & -\Omega_L\cos\phi & -\Omega_R \\ 0 & 0 & -\Omega_R & (\omega_0-\omega_L) \end{bmatrix} \\
-\frac{1}{2}\begin{bmatrix} 0 & 0 & 0 & 0 \\ 0 & 0 & 0 & 0 \\ 0 & 0 & 0 & 0 \\ 0 & 0 & 0 & \Gamma \end{bmatrix}&\begin{bmatrix} \tilde{\rho}_{00} & \tilde{\rho}_{01} & \tilde{\rho}_{02} & \tilde{\rho}_{03} \\ \tilde{\rho}_{10} & \tilde{\rho}_{11} & \tilde{\rho}_{12} & \tilde{\rho}_{13} \\ \tilde{\rho}_{20} & \tilde{\rho}_{21} & \tilde{\rho}_{22} & \tilde{\rho}_{23} \\ \tilde{\rho}_{30} & \tilde{\rho}_{31} & \tilde{\rho}_{32} & \tilde{\rho}_{33} \end{bmatrix} \\
-\frac{1}{2}\begin{bmatrix} \tilde{\rho}_{00} & \tilde{\rho}_{01} & \tilde{\rho}_{02} & \tilde{\rho}_{03} \\ \tilde{\rho}_{10} & \tilde{\rho}_{11} & \tilde{\rho}_{12} & \tilde{\rho}_{13} \\ \tilde{\rho}_{20} & \tilde{\rho}_{21} & \tilde{\rho}_{22} & \tilde{\rho}_{23} \\ \tilde{\rho}_{30} & \tilde{\rho}_{31} & \tilde{\rho}_{32} & \tilde{\rho}_{33} \end{bmatrix}&\begin{bmatrix} 0 & 0 & 0 & 0 \\ 0 & 0 & 0 & 0 \\ 0 & 0 & 0 & 0 \\ 0 & 0 & 0 & \Gamma \end{bmatrix} + \frac{1}{3}\Gamma\rho_{33}\begin{bmatrix} 1 & 0 & 0 & 0 \\ 0 & 1 & 0 & 0 \\ 0 & 0 & 1 & 0 \\ 0 & 0 & 0 & 0 \end{bmatrix}, \qquad (7.92)
\end{aligned}
$$

and the result is given in Eq. 7.96 on the following page (displayed in landscape orientation due to its size).

Equation 7.96 is quite large and any solution would need to be obtained numerically. However, we can still gain a bit of insight from considering its form. We are particularly interested in effects resulting from the transverse components of the magnetic field, which enter the equation as factors of $\Omega_L \sin\phi$.

From Eq. 7.96, we extract the component $\tilde{\rho}_{00}$ and find that

$$\dot{\tilde{\rho}}_{00} = \frac{-1}{\sqrt{2}}\Omega_L\sin\phi\,(\tilde{\rho}_{01}+\tilde{\rho}_{10}) + \frac{1}{3}\Gamma\tilde{\rho}_{33}, \qquad (7.93)$$

and furthermore,

$$
\begin{aligned}
\tilde{\rho}_{01}+\tilde{\rho}_{10} &= \int_0^t \left(\dot{\tilde{\rho}}_{01}+\dot{\tilde{\rho}}_{10}\right) \mathrm{d}t' && (7.94) \\
&= \frac{1}{\sqrt{2}}\Omega_L\sin\phi \int_0^t \left(2(\tilde{\rho}_{00}-\tilde{\rho}_{11}) - (\tilde{\rho}_{02}+\tilde{\rho}_{20})\right) \mathrm{d}t'. && (7.95)
\end{aligned}
$$

$$\begin{bmatrix} \dot{\tilde{\rho}}_{00} & \dot{\tilde{\rho}}_{01} & \dot{\tilde{\rho}}_{02} & \dot{\tilde{\rho}}_{03} \\ \dot{\tilde{\rho}}_{10} & \dot{\tilde{\rho}}_{11} & \dot{\tilde{\rho}}_{12} & \dot{\tilde{\rho}}_{13} \\ \dot{\tilde{\rho}}_{20} & \dot{\tilde{\rho}}_{21} & \dot{\tilde{\rho}}_{22} & \dot{\tilde{\rho}}_{23} \\ \dot{\tilde{\rho}}_{30} & \dot{\tilde{\rho}}_{31} & \dot{\tilde{\rho}}_{32} & \dot{\tilde{\rho}}_{33} \end{bmatrix} =$$

$$\begin{bmatrix}
\begin{pmatrix} \frac{-1}{\sqrt{2}}\Omega_L \sin\phi\,(\tilde{\rho}_{01}+\tilde{\rho}_{10}) \\ +\frac{1}{3}\Gamma\tilde{\rho}_{33} \end{pmatrix} &
\begin{pmatrix} \frac{1}{\sqrt{2}}\Omega_L \sin\phi\,(\tilde{\rho}_{00}-\tilde{\rho}_{11}-\tilde{\rho}_{02}) \\ -i\Omega_L \cos\phi\,\tilde{\rho}_{01} \end{pmatrix} &
\begin{pmatrix} \frac{1}{\sqrt{2}}\Omega_L \sin\phi(\tilde{\rho}_{01}-\tilde{\rho}_{12}) \\ -i\Omega_R\,\tilde{\rho}_{03} - 2i\Omega_L \cos\phi\,\tilde{\rho}_{02} \end{pmatrix} &
\begin{pmatrix} \frac{-1}{\sqrt{2}}\Omega_L \sin\phi\,\tilde{\rho}_{13} - \frac{1}{2}\Gamma\tilde{\rho}_{03} \\ -i(\omega_L-\omega_0+\Omega_L\cos\phi)\tilde{\rho}_{03} \\ -i\Omega_R\tilde{\rho}_{02} \end{pmatrix} \\
\begin{pmatrix} \frac{1}{\sqrt{2}}\Omega_L \sin\phi\,(\tilde{\rho}_{00}-\tilde{\rho}_{11}-\tilde{\rho}_{20}) \\ +i\Omega_L \cos\phi\,\tilde{\rho}_{10} \end{pmatrix} &
\begin{pmatrix} \frac{1}{\sqrt{2}}\Omega_L \sin\phi\,(\tilde{\rho}_{01}+\tilde{\rho}_{10}-\tilde{\rho}_{12}-\tilde{\rho}_{21}) \\ +\frac{1}{3}\Gamma\tilde{\rho}_{33} \end{pmatrix} &
\begin{pmatrix} \frac{1}{\sqrt{2}}\Omega_L \sin\phi(\tilde{\rho}_{11}-\tilde{\rho}_{22}+\tilde{\rho}_{02}) \\ -i\Omega_R\,\tilde{\rho}_{13} - i\Omega_L \cos\phi\,\tilde{\rho}_{12} \end{pmatrix} &
\begin{pmatrix} \frac{1}{\sqrt{2}}\Omega_L \sin\phi(\tilde{\rho}_{03}-\tilde{\rho}_{23}) \\ -\frac{1}{2}\Gamma\tilde{\rho}_{13} \\ -i\Omega_R\tilde{\rho}_{12} - i(\omega_L-\omega_0)\tilde{\rho}_{13} \end{pmatrix} \\
\begin{pmatrix} \frac{1}{\sqrt{2}}\Omega_L \sin\phi\,(\tilde{\rho}_{10}-\tilde{\rho}_{21}) \\ +i\Omega_R\,\tilde{\rho}_{30} + 2i\Omega_L \cos\phi\,\tilde{\rho}_{20} \end{pmatrix} &
\begin{pmatrix} \frac{1}{\sqrt{2}}\Omega_L \sin\phi(\tilde{\rho}_{11}-\tilde{\rho}_{22}+\tilde{\rho}_{20}) \\ +i\Omega_R\,\tilde{\rho}_{31} + i\Omega_L \cos\phi\,\tilde{\rho}_{21} \end{pmatrix} &
\begin{pmatrix} \frac{1}{\sqrt{2}}\Omega_L \sin\phi(\tilde{\rho}_{12}+\tilde{\rho}_{21}) \\ +\frac{1}{3}\Gamma\tilde{\rho}_{33} \\ -i\Omega_R(\tilde{\rho}_{23}-\tilde{\rho}_{32}) \end{pmatrix} &
\begin{pmatrix} \frac{1}{\sqrt{2}}\Omega_L \sin\phi\tilde{\rho}_{13} - \frac{1}{2}\Gamma\tilde{\rho}_{23} \\ -i\Omega_R(\tilde{\rho}_{22}-\tilde{\rho}_{33}) \\ -i(\omega_L-\omega_0-\Omega_L\cos\phi)\tilde{\rho}_{23} \end{pmatrix} \\
\begin{pmatrix} \frac{-1}{\sqrt{2}}\Omega_L \sin\phi\,\tilde{\rho}_{31} - \frac{1}{2}\Gamma\tilde{\rho}_{30} \\ +i(\omega_L-\omega_0+\Omega_L\cos\phi)\tilde{\rho}_{30} \\ +i\Omega_R\,\tilde{\rho}_{20} \end{pmatrix} &
\begin{pmatrix} \frac{1}{\sqrt{2}}\Omega_L \sin\phi(\tilde{\rho}_{30}-\tilde{\rho}_{32}) \\ -\frac{1}{2}\Gamma\tilde{\rho}_{31} \\ +i\Omega_R\,\tilde{\rho}_{21} + i(\omega_L-\omega_0)\tilde{\rho}_{31} \end{pmatrix} &
\begin{pmatrix} \frac{1}{\sqrt{2}}\Omega_L \sin\phi\,\tilde{\rho}_{31} - \frac{1}{2}\Gamma\tilde{\rho}_{32} \\ +i\Omega_R(\tilde{\rho}_{22}-\tilde{\rho}_{33}) \\ +i(\omega_L-\omega_0-\Omega_L\cos\phi)\tilde{\rho}_{32} \end{pmatrix} &
\left(\, i\Omega_R(\tilde{\rho}_{23}-\tilde{\rho}_{32}) - \Gamma\tilde{\rho}_{33} \,\right)
\end{bmatrix} \tag{7.96}$$

Substitution using Eqs. 7.93, 7.94, and 7.95 produces

$$\dot{\tilde{\rho}}_{00} \quad = \quad -\frac{1}{2}\Omega_L^2 \sin^2\phi \int_0^t \left(2(\tilde{\rho}_{00} - \tilde{\rho}_{11}) - (\tilde{\rho}_{02} + \tilde{\rho}_{20})\right) \mathrm{d}t' + \frac{1}{3}\Gamma\tilde{\rho}_{33}. \tag{7.97}$$

While the behavior of $(\tilde{\rho}_{02} + \tilde{\rho}_{20})$ over any period of time is not immediately obvious, it must be real, though there is no requirement that it be positive. The magnitude of this term is also limited by maintaining normalization. By contrast, if we expect the system to approach a steady state of some sort–and we do–the term $2(\tilde{\rho}_{00} - \tilde{\rho}_{11})$ must itself approach some constant value. Over many cycles, any oscillations in either term will average themselves out, and we find that

$$\tilde{\rho}_{00} \quad \sim \quad \Omega_L^2 \sin^2\phi. \tag{7.98}$$

Note that we do not rule out further dependence on $\Omega_L \sin\phi$ buried in the other terms, but it is clear that the dominant effect is proportional to the square of the transverse component of the magnetic field. Similar arguments may be also made regarding the populations $\tilde{\rho}_{11}$ and $\tilde{\rho}_{22}$.

Chapter 8

Conclusions

8.1 Results

We have developed an AC-MOT in hope that it would be useful to help us obtain samples of cold, confined, spin-polarized hydrogen-like atoms, particularly ^{37}K, which is the subject of our experiments on nuclear beta decay. As this isotope is radioactive and fairly short-lived ($t_{1/2} \approx 1.2s$), it is not normally available to us for testing purposes. As a result, we chose to use (stable) ^{41}K for testing and calibrations of the AC-MOT, due to its similar hyperfine structure.

The majority of the measurements in this thesis were performed in the "offline" AC-MOT, which was never intended to be used with radioactive isotopes. This was necessary because the "online" apparatus was not yet constructed at the time. Unfortunately, the offline AC-MOT was plagued by systematic problems, making it very difficult to produce reproducible measurements. This data is therefore of questionable value to the scientific community as a whole, however our qualitative findings are sufficient to provide useful guidance for us within the context of the larger nuclear beta decay experiment.

In particular, we have found that the AC-MOT has trap lifetimes that are long enough to be useful to us, even in spite of the many systematic effects that could not be fixed in the offline setup. We don't require a particularly long trap lifetime – the necessary consideration is that the trap lifetime must be significantly longer than the radioactive lifetime of ^{37}K ($\tau = t_{1/2}/\ln(2) \approx 1.8s$) so that the dominant loss mechanism is radioactive decay, rather than something we might be able to improve upon by adjustments to the apparatus.

Furthermore, the AC-MOT is robust enough to allow for it to be shut off intermittently for short periods of time – sufficient to allow us to optically pump the atoms and observe them before they disperse – without doing too much damage to the "average" trap lifetime. We've found that it is possible to have the AC-MOT off for a full 40% of the time without increasing the atom loss rate beyond what is tolerable, which in turn allows us to spend (nearly) 40% of our running time collecting beta decay data on spin-polarized atoms. This result is comparable to the 45% ‘MOT off time’ that has been used previously in the TRINAT research group with a DC-MOT, as in Dan Melconian’s thesis work [11]. It may still be possible to push the duty cycle further within the AC-MOT.

Additionally, in the AC-MOT, the residual magnetic quadrupole field not only decays rapidly, it starts out from close to zero as well, which is a great improvement on what could be accomplished with a DC-MOT. This in turn allows for better polarization of atoms within the cloud.

The included work on the Optical Bloch Equations is intended to be used as a qualitative theoretical ‘sanity check’ for numerical evolution codes [12] developed separately by our collaborator Ben Fenker in his Master’s thesis [13], and based on the description given in [14] .

8.2 Future Work

The TRINAT online setup, which is mainly designed for use in nuclear beta decay experiments, presents us with some novel possibilities for characterizing and working with the AC-MOT.

The first item of note is that the trapped atom cloud may be placed in an electrical potential, such that when an atom is ionized (or when it decays), the negatively charged electrons will be accelerated towards one side of the chamber, while the positively charged ions are accelerated towards the other. Negatively charged ions are unstable in an electric field of that magnitude (≥ 350 V/cm). This is useful in combination with additional hardware: at either end of the chamber, we have placed a stack of microchannel plates (to measure the time at which a particle hits), and a delay line (to determine the position of the hit).

Additionally, the online setup is equipped with a pulsed laser which is used to selectively photoionize trapped atoms from their excited state. This process is largely non-destructive, since the intensity of the laser is low enough that only a tiny fraction of the excited state atoms are photoionized.

In combination, this additional equipment will allow us to create a two-dimensional image of the atom cloud, with time-domain accuracy of ~ 5 ns – a great improvement from the 10s of milliseconds needed for a single CCD image. With AC frequencies of ~ 1 kHz such as we have been able to achieve, we will be able to image the trap at a wide range of phases during the AC-MOT cycle.

It is also possible to use the online AC-MOT as a crude electron spectrometer – a fact that was discovered accidentally. When an atom beta decays within the trap, one or more orbital electrons also become separated from the daughter atom, and these electrons and ions are accelerated by the electric field to microchannel plates on opposite ends of the chamber. In the past, the sudden approximation has been used to approximate the energies of such "shake-off" electrons. After TRINAT's December 2012 run, we noticed that the number of electrons collected in the microchannel plate varied with the magnitude of the magnetic field. This effect can be explained by taking into account the characteristic helical motion of a charged particle within a magnetic field, and so a larger magnetic field had the effect of decreasing the number of shake-off electrons impacting the microchannel plate. It may be possible to use this effect to measure the energy spectrum of these shake-off electrons directly, and thereby test the validity of the sudden approximation in this specific circumstance.

One problem we discovered in the online setup that had not been present in the offline AC-MOT (or even in shorter test runs with the online AC-MOT) was inductive heating of other materials within the chamber. As the online AC-MOT had much more metal than the offline MOT, this perhaps should not have come as such a surprise. Unfortunately, this inductive heating caused problems in the strip detectors (positioned directly above and below the quadrupole coils, outside of the vacuum chamber) which were intended to measure the energy spectrum of betas from decays within the trap. It may be possible to alleviate this problem by cooling the strip detectors. A second problem resulting from inductive heating is that it appears to cause materials within the vacuum system to outgas hydrogen, which is damaging to the MOT. However, it should be possible to mitigate the problem by running the AC-MOT at a lower frequency. Both of these fixes must be implemented before further use of the AC-MOT in TRINAT's beta decay experiments.

Bibliography

[1] E. L. Raab, M. Prentiss, A. Cable, S. Chu, and D. E. Pritchard, *Phys. Rev. Lett.* **59**, 2631 (1987).

[2] M. Harvey and A. J. Murray, *Phys. Rev. Lett.* **101**, 173201 (2008).

[3] A. Corney, *Atomic and Laser Spectroscopy* (Oxford University Press, New York, 1977).

[4] Harold J. Metcalf, Peter van der Straten, *Laser Cooling and Trapping* (Springer-Verlag New York, Inc., New York, 1999).

[5] V. Balykin, V. Minogin, and V. Letokhov, *Rep. Prog. Phys.* **63**, 1429 (2000).

[6] F. Touchard, P. Buimbal, S. Büttgenbach, R. Klapisch, M. De Saint Simon, J. M. Serre, C. Thibault, H. T. Duong, P. Juncar, S. Liberman, J. Pinard, J. L. Vialle, *Physics Letters* **108B** 3 (1982).

[7] S. Falke, E. Tiemann, and C. Lisdat. *Phys. Rev. A* **74**, 032503 (2006).

[8] S. Smale, *Summer 2012 Coop Report* (unpublished), 13 December 2012.

[9] T. B. Swanson, D. Asgeirsson, J. A. Behr, A. Gorelov, D. Melconian, *J. Opt. Soc. Am. B* **Vol. 15, No. 11** 2641 (1998).

[10] Marcis Ausinsh, Dmitry Budker, Simon M. Rochester, *Optically Polarized Atoms: Understanding Light-Atom Interactions* (Oxford University Press, New York, 2010).

[11] Dan G. Melconian (2000). *Measurement of the Neutrino Asymmetry in the Beta Decay of Laser-Cooled, Polarized 37K.* (Ph.D. Thesis).

[12] Benjamin Fenker (2013). *Measurement of Asymmetry Parameters in 37K – Optical Pumping of Alkali Atoms.* (Master's thesis). Retrieved from http://people.physics.tamu.edu/fenkerbb/Masters.pdf .

[13] B. Fenker, Optical Bloch Equations Code, retrieved from http://code.google.com/p/optical-bloch-equations .

[14] P. Tremblay and C. Jacques, *Phys. Rev. A* **41**, 4989 (1990).

[15] R. Shankar, *Principles of Quantum Mechanics, 2nd ed.* (Plenum Press, New York, 1994).

Appendix A

Waveform Generation Code

```python
# Python 2.7.3
import os
import numpy       # numpy version 1.6.2
import matplotlib  # matplotlib version 1.2.0
from matplotlib import pyplot
import math

pi = numpy.pi
deg = pi/180.0

plotting = False        # Show the waveform on screen too?
maxpoints = 16300.0     # Maximum number of points.  16300 is max.  7500 is editable.
minpoints = 500.0       # Minimum points to allow in a waveform.  No idea what coarseness is acceptable here.
maxsample = 40000000.0  # Max sample rate (Hz).  Allowable values are this number / N_sample.  N_sample has some max, too.

t_AC = 9.824e-4       # Seconds.
f_AC = 1.0/t_AC       # Hz.  Must be a float.
cycles_on = 3.0
cycles_off = 2.0
A = 1.0                 # Amplitude of the output waveform.

sinfile = "s_15q.dat"
phi_start = 0.0*deg + 1.0*pi/2.0
t_startdelta = 1.2e-5   # Time for the delta-spike at the beginning of the sinusoid.
phi_end = -6.0*deg + 1.0*pi/2.0
t_enddelta = 6.0e-6     # Time for the delta-spike at the end of the sinusoid.

def fileclear(filename):
  fileclear1 = open(filename, ’w’)
  fileclear1.close()
  print filename, "cleared."
  return 0

```

```
def main():
  # I'm not sure why Python requires some global variables but not others
  # to be explicitly declared within a function, but whatever.
  global phi_start
  global phi_end

  print "f_AC =", f_AC
  if cycles_off == 0.0:
  # This would be a continuous sinusoid.  No point in messing it up
  # with extra parameters that I forgot to adjust.
    phi_start = pi/2.0
    phi_end = pi/2.0
  print "phi_start - pi/2 =", (phi_start - 1.0*pi/2.0)/deg, " degrees."
  print "phi_end - pi/2   =", (phi_end - 1.0*pi/2.0)/deg, " degrees."
  N_cycles = cycles_on + cycles_off

  # Figure out how many data points to use.
  N_points = 16000.0   # 16000.0 (float!!) will work for lots of setups.
  N_sample = (maxsample*N_cycles) / (f_AC*N_points) # All of these things must be floats s.t. N_sample will be a float.
  points_per_cycle = N_points / N_cycles
  # If the guess fails, try to find some other number of points to use.
  if maxsample/f_AC != float(int(maxsample/f_AC)):
    # maxsample/f_AC should be a whole number, otherwise the true trap frequency will be wrong.
    print "maxsample/f_AC =", maxsample/f_AC
    print "*** Yeah, this isn't going to work.  Adjust trap frequency."
    # It's better to just adjust the trap frequency you're going for manually (and pick something that will work), so that you actually know what you're going to get.
    return
  elif ( (float(int(N_sample)) != N_sample) or (float(int(points_per_cycle)) != points_per_cycle) ):
    N_points = maxpoints
    points_per_cycle = N_points / N_cycles

  # N_sample = (maxsample*N_cycles) / (f_AC*N_points)
  # This is N_sample as in "samplerate=40,000,000.0/N_sample".
    N_sample = maxsample / ( points_per_cycle*f_AC)
    while ((float(int(N_sample)) != N_sample) or (float(int(points_per_cycle)) != points_per_cycle)) and (N_points
```

```
      >= minpoints):
    N_points = N_points - 1.0    # We are iterating over a float.  Crazy, right?
    points_per_cycle = N_points / N_cycles
    N_sample = maxsample / ( points_per_cycle*f_AC)
  if (N_points == minpoints - 1.0):
    print "A waveform cannot be generated with these parameters."
    print "Adjust the trap frequency, the number of trap cycles in the waveform, and/or the minimum acceptable number of points."
    return # No point continuing when we've already failed!
N_points = int(N_points)

# Now find the sample rate.
# awc.exe will *round* samplerate to the nearest value of 40,000,000/N, and reads to 4 places past the decimal.
# For N_sample < ~100,000, there is no ambiguity.  This is much higher N_sample than we require.
samplerate = maxsample / N_sample  # float.

delta_t = delta_t = 1.0/samplerate
print "* The waveform is", N_points*delta_t, "seconds long."
n_on = int( points_per_cycle*cycles_on + points_per_cycle*(phi_end - phi_start)/(2.0*pi) )

if cycles_off == 0.0:
  n_enddelta = 0
  n_startdelta = 0
else:
  n_enddelta = int(t_enddelta / delta_t)
  n_startdelta = int(t_startdelta / delta_t)

n_off = N_points - n_on - n_enddelta - n_startdelta
print "n_off =", n_off, ";   n_on =", n_on
print "n_enddelta =", n_enddelta
print "n_startdelta =", n_startdelta
print "N_points =", N_points

v_arr = numpy.zeros(N_points)
t_arr = numpy.zeros(N_points)
for i in range(N_points):
  t_arr[i] = float(i)*delta_t

# Make sure voltage is well-zeroed.
# For some reason, this seems to actually matter.
for i in range(N_points):
# Make every point this way. We'll over-write some later.
  if (i%2 == 0):
```

```
      v_arr[i] =  0.00000000001000
    else:
      v_arr[i] = -0.00000000001000

  # Make the starting spike.
  for i in range(n_off, n_off+n_startdelta):
    v_arr[i] = A
  # Make the ending delta-spike.
  if n_enddelta != 0:
    for i in range(N_points-n_enddelta-1, N_points):
      v_arr[i] = -1.0*A
  # Make datapoints for the sinusoid itself.
  for i in range(n_off+n_startdelta, N_points-n_enddelta):
    v_arr[i] = A*numpy.sin(phi_start + 2.0*pi*f_AC*(t_arr[i] - t_arr[n_off+n_startdelta]) )

  line1 = "%i"    % N_points
  line2 = "%8.4f" % samplerate
  line3 = "%i"    % 0            # '0' works.
  line4 = "%8.4f" % 1000.0000    # '1000.0' works.

  # Write out the waveform, header first.
  fileclear(sinfile)     # Clear any files with the same names that may have already been there.
  sinhandle = open(sinfile, 'a')
  sinhandle.write(line1+'\n')
  sinhandle.write(line2+'\n')
  sinhandle.write(line3+'\n')
  sinhandle.write(line4+'\n')
  numpy.savetxt(sinhandle, v_arr, fmt='%1.14f')
  sinhandle.close()
  print sinfile, "saved.\n"

  if plotting == True:
    print "Beginning to plot."
    fig1 = pyplot.figure()
    t_arr = numpy.linspace(0.0, N_points*delta_t, num=N_points, endpoint=False)
    p1 = fig1.add_subplot(1, 1, 1)
    p1.grid(True)
    p1.plot(t_arr, v_arr)
    p1.set_ylabel("Voltage")
    pyplot.show()
  return 0

if __name__ == '__main__':
  main()
```

wavegen_new3.py

Appendix B

Things that Are Very Obvious

B.1 The Center of Gravity

It's what happens when you set $A = 0$ and $B = 0$. That is all.

B.2 Diagonalizing the Hamiltonian

Given a Hermitian matrix $\hat{\Omega}$, there exists a unitary matrix $\hat{U}$ such that $\hat{U}^\dagger\hat{\Omega}\hat{U}$ is diagonalized. Solving for this matrix $\hat{U}$ is, in this case, equivalent to solving the eigenvalue problem for $\hat{\Omega}$ [15]. As it turns out, $\hat{U}$ is the matrix of eigenvectors of $\hat{\Omega}$, by which I mean that the eigenvectors are column vectors, and they're all squished together to make $\hat{U}$. It doesn't matter what order you put them in, but they probably have to be normalized.

Then, if

$$\hat{\Omega}' := \hat{U}^\dagger\hat{\Omega}\hat{U}, \tag{B.1}$$

we find that $\hat{\Omega}'$ is the diagonal matrix with its elements being the eigenvalues. They're in the same order as the eigenvectors we squished together to make $\hat{U}$ previously.

Also, a unitary operator, $\hat{U}$ is one which satisfies:

$$\hat{U}\hat{U}^\dagger = \hat{U}^\dagger\hat{U} = \underset{\sim}{I}. \tag{B.2}$$

B.3 Rotating Coordinates

If by $\hat{\Omega}$ we really mean the Hamiltonian $\hat{H}$, and by $\hat{U}$ we really mean a coordinate change that takes us to rotating coordinates such that we can easily make a rotating wave approximation, we must take more things into account. In particular, we find that our new rotating-coordinate Hamiltonian, $\tilde{H}$ is given by:

$$\tilde{H} = \hat{U}^\dagger\hat{H}\hat{U} - \hbar\hat{A} \tag{B.3}$$

where

$$\hat{U} := e^{-i\hat{A}t}. \tag{B.4}$$

This additional term arises from our statement of the Schrodinger equation,

$$\hat{H}\left|\psi\right\rangle = i\hbar\frac{\partial}{\partial t}\left|\psi\right\rangle. \tag{B.5}$$

In particular, note that B.5 includes only a partial derivative of the wavefunction. I derive this result explicitly in Chapter 7.2. See also Ref. [10], pg. 195.

B.4 Lifetimes and Half-Lifes

Since different people use different notation to describe exponential decay of a physical quantity, it is useful to be able to relate two of the most common methods for describing the decay. We begin with the rate equation,

$$\frac{dN}{dt} = -\gamma\, N, \tag{B.6}$$

where it is clear that the "rate" of decay must be $\gamma\, N$. If we initially have N_0 of the quantity in question, then Eq. B.6 has as its solution

$$N(t) = N_0\, e^{-\gamma\, t}. \tag{B.7}$$

Note that the physical interpretation of γ is the "linewidth".

We'll wish to convert γ into other quantities of interest. In particular, we can re-write the solution B.7 as

$$N(t) = N_0\, e^{-t/\tau}, \tag{B.8}$$

where $\tau = 1/\gamma$ is referred to as the "lifetime". Then, we find the half-life $t_{1/2}$ by enforcing the fact that it is the time at which the number of remaining atoms is equal to half of what was originally present. Therefore,

$$N(t_{1/2}) = N_0 e^{-t_{1/2}/\tau} = \frac{1}{2}N_0 \tag{B.9}$$

$$e^{-t_{1/2}/\tau} = 1/2 \tag{B.10}$$

$$t_{1/2}/\tau = \ln(2). \tag{B.11}$$

Thus, we see that

$$t_{1/2} = \ln(2)\,\tau, \tag{B.12}$$

where τ is the "lifetime" of the state, and $t_{1/2}$ is its "half-life".

B.5 Reduced Matrix Elements

The Wigner-Eckart Theorem says, for vector operator V^q,

$$\langle \alpha' j' m' | V^q | \alpha j m \rangle = \langle j' m' | j 1 m q \rangle \langle \alpha' j' \| V \| \alpha j \rangle. \tag{B.13}$$

The point being that $\langle \alpha' j' \| V \| \alpha j \rangle$ is the same for all m and q.

B.6 Doppler Cooling Limit

Here it is!

$$kT_{\mathrm{D}} = \frac{1}{2}\hbar\Gamma \tag{B.14}$$